Fall 2015

On the dynamic analysis of compliant mechanisms based on the pseudo-rigid-body model

Andrew Christian
Missouri University of Science and Technology

Department:

ON THE DYNAMIC ANALYSIS OF COMPLIANT MECHANISMS BASED ON THE PSEUDO-RIGID-BODY MODEL

by

ANDREW JAMES CHRISTIAN

A THESIS

Presented to the Faculty of the Graduate School of the

MISSOURI UNIVERSITY OF SCIENCE AND TECHNOLOGY

In Partial Fulfillment of the Requirements for the Degree

MASTER OF SCIENCE IN MECHANICAL ENGINEERING

2015

Approved by:

Dr. Ashok Midha, Advisor
Dr. Walter Eversman
Dr. Nishant Kumar

ABSTRACT

Compliant mechanisms derive some or all of their mobility from the deflection of flexible members. A pseudo-rigid-body model (PRBM) provides an elegant and simple way of modeling and analyzing traditionally nonlinear large-deflection problems pertaining to compliant mechanisms. In this work, several aspects pertainting to the dynamics of compliant mechanisms are considered. First, dynamic models are derived to predict not only the natural frequency of the large-deflection systems, but also the transient response, using the PRBM approach. A unique multi-stage damping model is developed to determine the transient response in free vibration. Recent works have neglected to consider the transient response prediction of these problems. Investigations are conducted into the dynamic analysis of partially compliant slider mechanisms, composed of rigid and compliant segments as well as revolute and prismatic pairs are considered. The static response of these mechanisms is predicted and tested. The PRBM is then used to determine their dynamic response with emphasis on the energy characteristics of these mechanisms. Specifically, modular constant-force mechanisms are considered in this work primarily for their unique force-deflection characteristics. It is anticipated they would have a multitude of applications. Experimental results are presented ranging from static to dynamic testing.

ACKNOWLEDGEMENTS

I am most to my graduate advisor, Dr. Ashok Midha for his constant support and guidance, coupled with his expectation for excellence. In guiding me through this research, he encouraged me to perform at a higher academic and professional level. His expertise and experience have always helped achieve practical solutions to the most difficult problems. This research would not have been successful without his guidance.

I also wish to thank my committee members, Dr. Nishant Kumar and Dr. Walter Eversman, two of the most caring and pragmatic teachers I have interacted with during my time at Missouri S&T. Their insights and approval of this reasearch are most gratefully acknowledged.

I am thankful to the Department of Mechanical and Aerospace Engineering and the Product Innovation and Creativity Center (PICC) for financial support provided as a Graduate Teaching Assistant and as a PICC fellow.

I am appreciative and thankful to my research group and co-workers, Pratheek Bagivalu Prasanna, Vamsi Lodagala, Sushrut Bapat, and Krutika Karthik. The many thoughtful discussions with them have played a key role in shaping this research. A special thanks goes to Brian Bullock and Dr. Daniel Stutts for their patience, guidance, and practical knowledge.

Finally, to my parents, Ron and Martha Christian, my wife, Dava Mentis and her son Layton Elliott, for their constant support and encouragement through all the difficult times.

TABLE OF CONTENTS

LIST OF ILLUSTRATIONS

Page

LIST OF TABLES

Page

1. INTRODUCTION

1.1 COMPLIANT MECHANISMS

Compliant mechanisms are devices that gain some or all of their mobility through the deflection of their flexible members. This deflection is accompanied by a transformation or transference of motion, force, and/or energy [1,2]. Figure 1.1 shows a one-piece compliant fish hook remover, the Compliers [3], which utilizes a fully-compliant mechanism. The motion and force transference is enabled due to the compliant segments of the mechanism. A majority of mechanisms can be made compliant by replacing their rigid member with flexible segments.

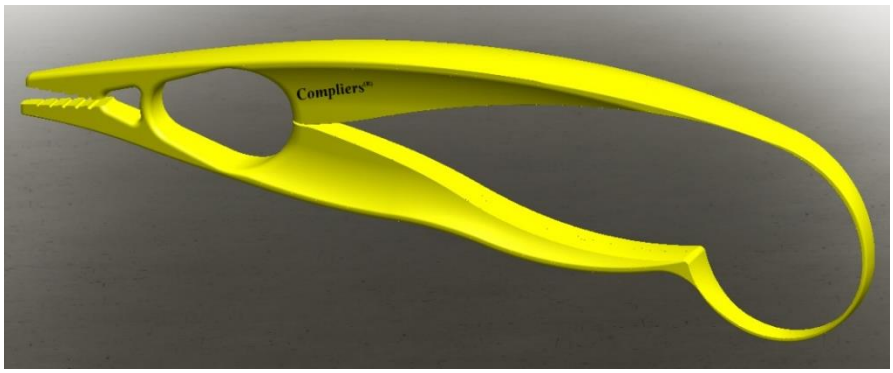

Figure 1.1. Compliers® Fully Compliant Fishhook Remover

Compliant mechanisms are typically designed for prescribed displacement and/or force boundary conditions and/or energy storage requirements. With the definitions provided in [1, 2], a compliant mechanismmay be designed with the notion of integrating

its function into the body of the mechanism; several advantages are realized as a result. Simply by applying appropriate design methodologies, compliant mechanisms exhibit:

1.) Part-count reduction
2.) Reduced assembly time
3.) Simplified manufacturing processes
4.) Increased precision
5.) Increased reliability
6.) Reduced wear and lash
7.) Reduced weight
8.) Reduced maintenance

However, compliant mechanisms typically exhibit two drawbacks. First, compliant mechanisms frequently experience large deflections, and their analysis is rendered difficult using traditional engineering methods. Second, issues of creep and fatigue become more important and have to be considered more carefully.

1.2 HISTORICAL DEVELOPMENT OF COMPLIANT MECHANISMS

Compliance in life has been a part of the world since the beginning. Natural compliance may be found in tree saplings, where early humans exploited the energy storage characteristics to make tools and weapons. Perhaps the earliest example of compliance can be found in the atlatl and dart. The atlatl itself is a rigid extension, however, the dart may be regarded as a flexible energy storage element [4]. Another early example, perhaps more widely known, would be the English longbow constructed from the Yew bush [5]. It is interesting to note that while looking at mechanisms in

history, compliant mechanisms had their hand in expanding ancient civilizations who had first developed them. More recently, development of compliant mechanisms has exploded, and for less baser objectives than war. The development of non-pneumatic tires, for example the Michelin X-Tweel, has resulted in an airless tire that utilizes a compliant honeycombed structure to provide support [6]. Researchers at Brigham Young University have developed a compliant replacement for spinal disks as an alternative to spinal fusion [7]. Numerous examples may be seen in the development of compliant robot end effectors that aid in increased precision, reliability, and safety.

The study of elastica had been developed for years prior to the publication of Leonhard Euler's work in 1744. He deserves much credit for building upon and expanding the field of elastica analysis by providing characterization of curves and solutions to differential equations [8]. After Euler, the field of large deflection became relatively stagnant until 1968, when Burns and Crossley [9] used kinetostatic approaches to synthesize and analyze large-deflection mechanisms. Bisshopp and Drucker [10] developed closed-form elliptic integral solutions to the large-deflection analysis of a cantilever beam end loaded with a vertical force. Her and Midha [11] developed a method known as the chain algorithm that discretized a continuum into small, straight beam segments, and treated each segment as a cantilever beam with fixed end conditions to the preceding element. This method utilized a shooting method with an iterative Newton-Raphson method to solve for specified displacement boundary conditions. This method continues to serve as a precise and rapid solver for complex geometries and loading conditions.

Salamon [12] developed methods of designing rigid-link mechanisms and implementing a compliant link to analyze the mechanism utilizing a Pseudo-Rigid-Body Model (PRBM), discussed in depth in the next chapter. Salamon and Midha [13] studied the effect of compliance on the mechanical advantage of mechanisms. Midha et al., [14] and Bapat [15] utilized these concepts and further investigated mechanical advantage of compliant mechansisms drawing important conclusions. Byers and Midha [16] developed a parallel compliant griper device using the chain algorithm. Nahvi [17] developed static and dynamic models of compliant mechanisms using a finite element approach. Murphy [18] generalized a theory of type synthesis for compliant mechanisms by adding compliant features to existing rigid-body mechanisms. Howell [19] investigated the energy storage and kinematic equations of PRBM to synthesize compliant mechanisms for desired energy storage characteristics. Howell and Midha [20] proposed a PRBM for analysis purposes and optimization of fully compliant mechanisms, and Howell and Midha [21] designed mechanisms using small-length flexural pivots (SLFPs). Howell [22] and Howell and Midha [23] extended the PRBM for cantilever beams subjected to any combination of moment and end-force loads. Midha et al., [24] and Bapat [15] presented a PRBM model for a compliant beam with an inflection point. Mettlach and Midha [25] developed the concept of the characteristic deflection domain, and this work was utilized by Bapat [15] and Midha and Bapat [26]. Pauly [27] and Kuber [28] presented works leading to improvements in parameterization of key values of the PRBM

1.3 HISTORICAL DEVELOPMENT OF CONSTANT-FORCE MECHANISMS

Early work can be witnessed in the development of constant-force springs, which resemble a coil of sheet metal. These springs can generate constant force for large ranges of motion [29]. Some of the earliest patents for constant-force mechanisms can be seen in [30-32]. These mechanisms utilize a combination of rigid links and mechanical springs to achieve constant force over a desired range of motion. Harmening [33] developed a four bar mechanism for mass balancing. Carson [34] developed a synthesis technique to achieve mechanisms with the same input and output forces for the general mechanism case. Jenuwine and Midha [35] used loop-closure and energy methods to develop a mechanisms leading to a constant-force output for accelerated pavement testing. Murphy [18] developed type synthesis methods for compliant mechanisms and discussed partially compliant constant-force configurations. Howell et al., [36] utilized an optimization scheme of the PRBM to synthesize constant-force four-bar mechanisms. Midha et al., [37] employed this theory for electrical connectors. Miller et al., [38] experimentally validated the theory of dimensional synthesis. Parkinson et al., [39] utilized parametric optimization to develop constant-force mechanisms. Evans and Howell [40] developed a robotic end-effector for glass cutting applications. Weight [41] compared compliant constant-force mechanisms based on certain parameters like stiffness, percentage constant force, etc., and optimized them to obtain new mechanisms with improved characteristics. Nahar and Sagar [42] analyzed a constant-force relationship for a double-sided mechanism used for micro/macro applications and experimentally validated the relationship. Howell and Magleby [43] developed a resistance module for an exercise machine that would provide a substantially constant output force for a range of input displacement. Meaders and Mattson [44] performed a

robust design optimization of constant-force electrical connectors that were subjected to mating uncertainty. Hajhashemi et al., [45] developed a constant-force micro-gripper for precise positioning of needles and surgical knives in teleoperation surgeries. Lan et al., [46] presented a constant-force mechanism to regulate the contact force of a robot end-effector. Ugwuoke [47] designed and developed compliant constant-force mechanisms for use as constant-force compression spring electrical contacts.

1.4 HISTORICAL DEVELOPMENT OF COMPLIANT MECHANISMS DYNAMICS

The study of large-deflection dynamics has been very broad and not specifically tailored to compliant mechanisms. However, two specific works exist that study the large-deflection vibrations of compliant mechanisms. These works also provide the inspiration for the present research. Boyle [48] extended the static development of the constant-force four bar mechanisms and applied Lagrangian dynamics to obtain a closed-form model to determine the dynamic response. The constant-force four bar mechanisms were developed in [37] Static and dynamic testing was done, however conclusions drawn may not be completely representative of constant-force mechanisms as the static portion of testing failed to yield constant force. Lyons [49] studied the natural frequency characteristics of compliant cantilever beams in combined loading and compared with FEA and experimental results. The theory was based on utilizing the mass moment of inertia of the PRBM as the mass term. The theory was also applied to micro and macro mechanisms with experimental validation. Yu et al., [50] developed natural frequency predictions based on energy equivalence methods. Wang and Yu [51] developed highly parametric equations to develop the energy expressions for different loading conditions and extend this theory to four bar mechanisms with negligible side link masses. There

exist numerous other works that are tailored to a specific mechanism and lose generality and typically involve finite element methods, as in the work of [52].

1.5 SCOPE OF INVESTIGATION

The main objective of the present work is to implement a constant-force mechanism design, experimentally test the mechanism for force constancy, develop a simplified dynamic model utilizing basic compliant mechanism principles, and provide experimental validation of the dynamic model developed. The primary device under consideration is a 2-D planar, four-bar compliant slider mechanism. The present research is divided into six sections.

Section 1 presents an introduction and a historical development of the pertinent components of the present research.

Section 2 presents current methods for large-delfection analysis, knowns as the PRBM. The PRBM for end force loading condtions will be discussed in detail.

Section 3 will discuss the development of the basic dynamic model for compliant segments undergoing beam end forcing. A new dynamic model will be presented in contrast to previous work. The transient response of a single segment will be discussed and experimental results provided.

Section 4 will discuss the development on a compliant constant-force slider mechanism based on the virtual work approach. An optimization scheme is implemented to determine appropriate design parameters that provides a constant force or nearly constant-force mechanism. Static test results will be presented.

Section 5 will detail the experimental dynamic testing completed on the constant-force mechanism.

Section 6 will discuss conclusions drawn and provide a path towards future research that should be completed.

The motivation for this study is twofold. Firstly, little work has been done studying the dynamic energy characteristics of compliant mechanisms by way of the pseudo-rigid-body model. Properly modeling the energy characteristics of compliant mechanisms in a dynamic scenario will only help to further their applications. Secondly, mechanisms with unique force deflection curves have interested the engineering community for several years. The applications using constant-force mechanisms are expected to be bountiful and a further study of these mechanisms and proper modeling techniques is necessary. From biomedicalto electro-mechanical to manufacturing applications, these mechanisms are increasingly finding utility in a host of industries. Therefore, in order to advance their usage, a thorough understanding and modeling methodology must be developed.

2. LARGE-DEFLECTION ANALYSIS

2.1 INTRODUCTION

The geometric nonlinearities associated with large deflections pertaining to compliant mechanisms makes analysis very difficult. The underlying equation that requires a solution is the classic Euler-Bernoulli Beam Equation:

$$M = EI \cdot \frac{\partial \theta}{\partial s} \tag{1}$$

Traditional analysis assumes small deflections, leading to the assumption that curvature is equal to the second derivative of the deflection as shown below:

$$M = EI \cdot \frac{\partial^2 y}{\partial x^2} \tag{2}$$

In large-deflection analysis this assumption does not hold true, and the proper equation is given by below In turn the solution to the large-deflection problem becomes problematic.

$$\frac{\partial \theta}{\partial s} = \frac{1}{\left(\left[1 + \left(\frac{\partial y}{\partial x} \right)^2 \right]^{\frac{3}{2}} \cdot \frac{\partial^2 y}{\partial x^2} \right)} \tag{3}$$

In order to address these issues, Bisshopp and Drucker [10] developed closed-form solutions for cantilever beams for vertical end loads. Benamar and Bennouna [53] presented methods of weighted coefficients to solve nonlinear vibration problems and decomposed the solutions on a per mode basis. Gorski [54] presented a compilation of

large-deflection analysis with hundreds of sources. It can be seen that in the arena of large deflections a multitude of analysis methods exist, all focused around solving equation (3). These methods include numerical methods, elliptical integral, and PRBM models. A straightforward method for practicing engineers for a quick implementation is the PRBM. The PRBM allows both graphical visualization and accurate solutions to large-deflection problems. The PRBM utilizes several optimization routines that have been tabulated as functions of beam geometry and loading. Section 2.2 will discuss these parameters in context of a cantilever beam.

2.2 THE GENERAL PRBM MODEL FOR CANTILEVER BEAM WITH FORCE AND FREE END (FIXED-PINNED)

A cantilever beam with length L and uniform cross section undergoing small strain deflection is shown in Figure 2.1. The end force can be a combination of vertical (P) and horizontal (nP) loading, where the resultant force is applied at an angle of ϕ. The beam end angle is denoted by θ_0 . By assuming small strains, the beam geometry remains approximately the same before and after deflection, which has been proven true through multiple experimental results [15].

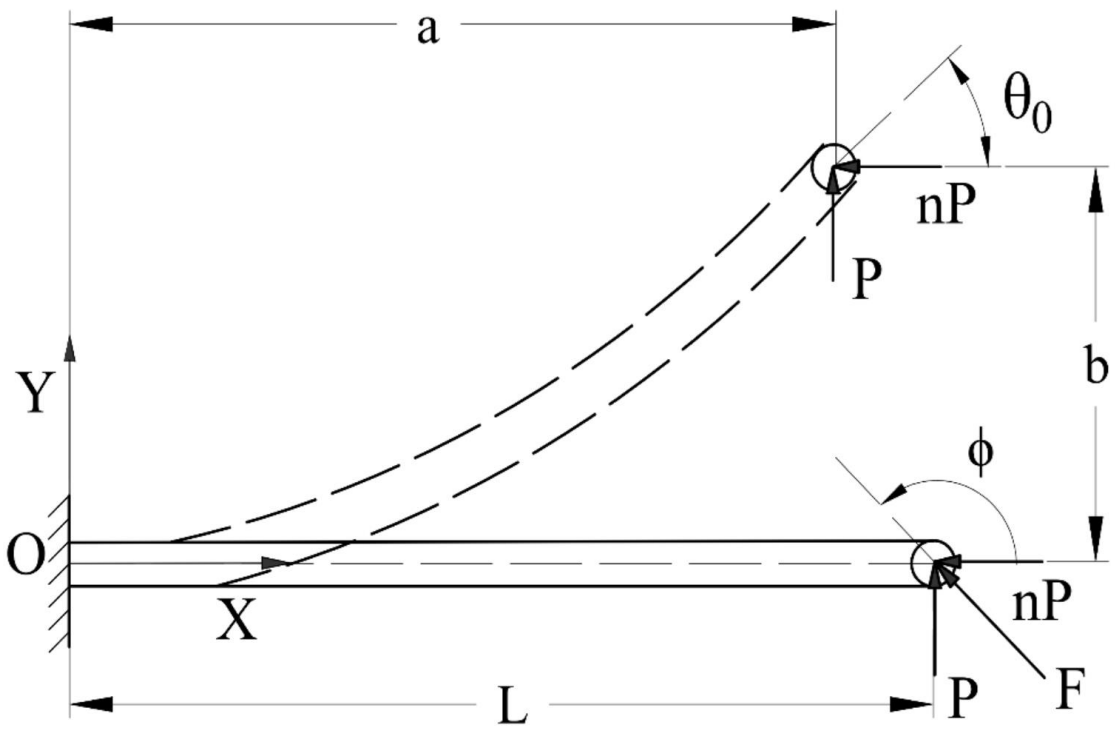

Figure 2.1. Cantilever Beam Undergoing Large-deflection

Upon examination, the free end of the beam is seen to follow a nearly circular path with a center of curvature, known as the characteristic pivot, located near the clamped end of the beam [19]. Physically, the beam undergoes deflection along the entire length of the beam, however as one approaches the clamped end, the deflections become smaller. The PRBM of the cantilever beam is modeled as two rigid links joined at the characteristic pivot with a torsional spring. The location of the characteristic pivot was found in [20] via optimization to be at a distance of γL from the free end. γ, is known as the characteristic radius factor. The torsional spring mimics the resistance to bending of the continuous beam. The PRBM of the beam is shown in Figure 2.2.

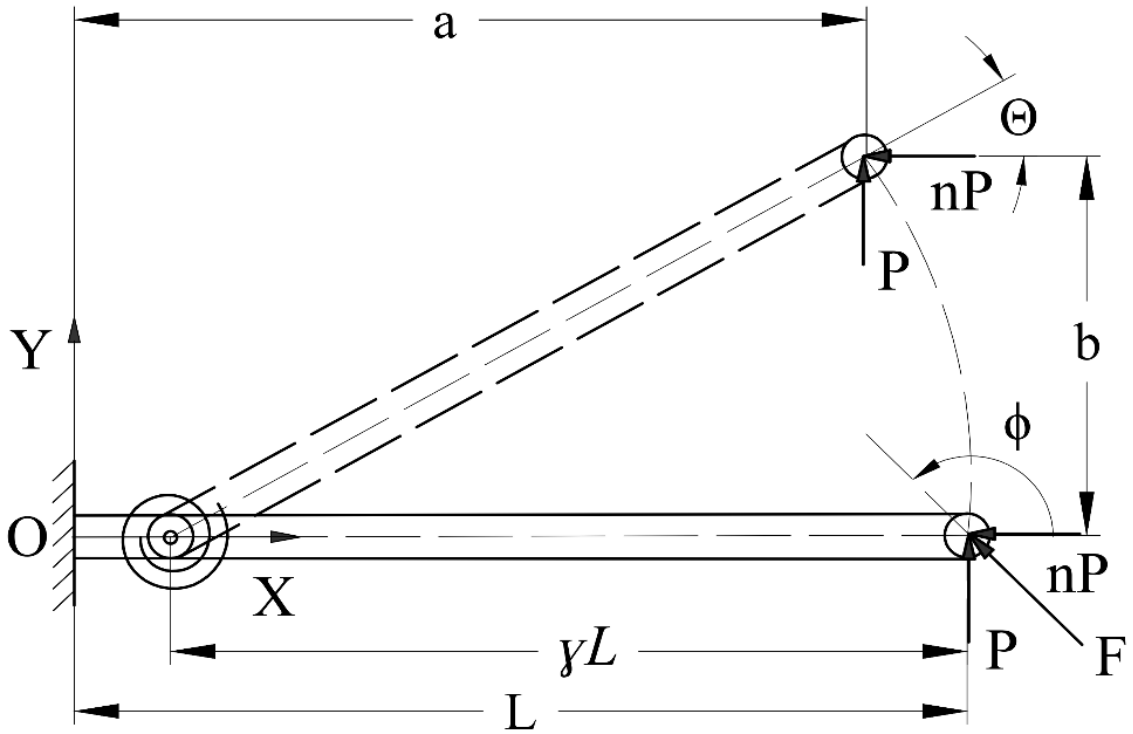

Figure 2.2. PRBM of Large-deflection Cantilever Beam

The angle θ is referred to as the pseudo-rigid-body angle, and is a measure of the beam deflection in the PRBM. The beam end location can be found using equations below, where *a* is the horizontal location and *b* is the vertical location. It is important to note that the values for the PRBM constants may be obtained using either the averaged integral equations, or tabulated values in the literature. Recently, Midha et al., [55] gave improved PRBM variables that were an improvement on those given in [22].

$$a = L \cdot [1 - \gamma \cdot (1 - \cos(\theta))] \tag{4}$$

$$\mathrm{b} = \gamma \cdot \mathrm{L} \cdot (\sin(\theta)) \tag{5}$$

The equation to find the torsional spring stiffness is given below:

$$\mathrm{K} = \frac{\gamma \cdot \mathrm{K}_{\theta} \cdot E \cdot I}{L} \tag{6}$$

While many other segment types exist, the fixed free beam is the main subject of the present research. Readers are referred to Bapat [15] and Karthik [56] for further review of the segment types. The limitations of the PRBM include increasingly higher error as the PRBM angle increases. Furthermore, the PRBM is only applicable to small strain deformation, which implies that the beam must be of Euler-Bernoulli type. This section presented several methods of large-deflection analysis. By comparison, the PRBM is a simplified approach to the large-deflection problem as compared to the elliptic integral approach. While the chain algorithm has proven to be fast and accurate, the user often can lose the visualization that the PRBM offers.

3. LARGE-DEFLECTION DYNAMICS

3.1 INTRODUCTION

The PRBM has been shown to accurately predict the static response of large-deflection members. Given the static response is accurately portrayed, a dynamic model can be developed based on the PRBM. A brief explanation of the Euler-Bernoulli model will be given, but first several fine points must be enumerated about compliant mechanisms and their behavior.

The large-deflection problem has been studied by numerous researchers. Early research was done to provide a closed-form solution that could be solved. With the advent of the PRBM, a numerical solution was presented that gave an algebraically closed-form solution that was accurate to within an acceptable degree of 0.5% relative error [19]. Recently, several attempts have been made at using finite element analysis techniques and numerical optimization schemes that are quite cumbersome to the end user and do not capture the simplicity and elegance of the PRBM. While the PRBM as used here is a single-degree-of-freedom system, the development of PRBM's containing multiple characteristic pivots can be used in a similar manner for dynamic situations.

Midha [57] identified the fundamental concept of compliant mechanisms: compliant mechanisms behave as they are designed to. Behavior of mechanisms is often not fully integrated into the design process. However, by the unique nature of compliant mechanisms, the mechanism behaves in a deterministic fashion and is limited in the number of ways that it can behave. This behavior was investigated by Midha and Bagivalu Prasanna [58] by investigating the number of statically deflected positions

possible. This work provides a foundation of how to determine the possible deflected shapes of a compliant mechanism based on the minimum of potential energy. In this development, non-following force, and beam end loading only are considered [20]. Given these constraints, there are a very limited number of ways in which the beams may be deflected.

It would be appropriate here to distinguish the large-deflection compliant systems on hand from yet another class of large displacement motions, as in high speed machinery undergoing vibration superposed onto the nominal rigid-body motion. The resulting equations of motion are characterized by time-dependent coefficients, and the system is subject to parametric vibrations and instability [59].

Another justification for the use of a single-degree-of-freedom system is found by analyzing the small-deflection Euler-Bernoulli beam. A good dynamic model should encapsulate the majority of potential and kinetic energies of a system. Analyzing the linear Euler-Bernoulli beam model, and observing the energies as a function of mode numbers will help to understand the relative order of contributions of modes. Figures 3.1 and 3.2 show the kinetic energy and potential energy, respectively, vested in each mode. As seen in these figures, the majority of energy is captured in the first mode of free vibration. Figures 3.1(b) and 3.2(b) show amplified plots to highlight the relative energy contents of the higher modes. The plots in Figures 3.1 and 3.2 represent the energy contents in each mode contributing to the total motion of the free vibration response when the beam end is given an intial deflection and released. As may be seen, a majority of the energy is captured in the first mode of vibration, an expected result due to the intial deflection in the first mode.

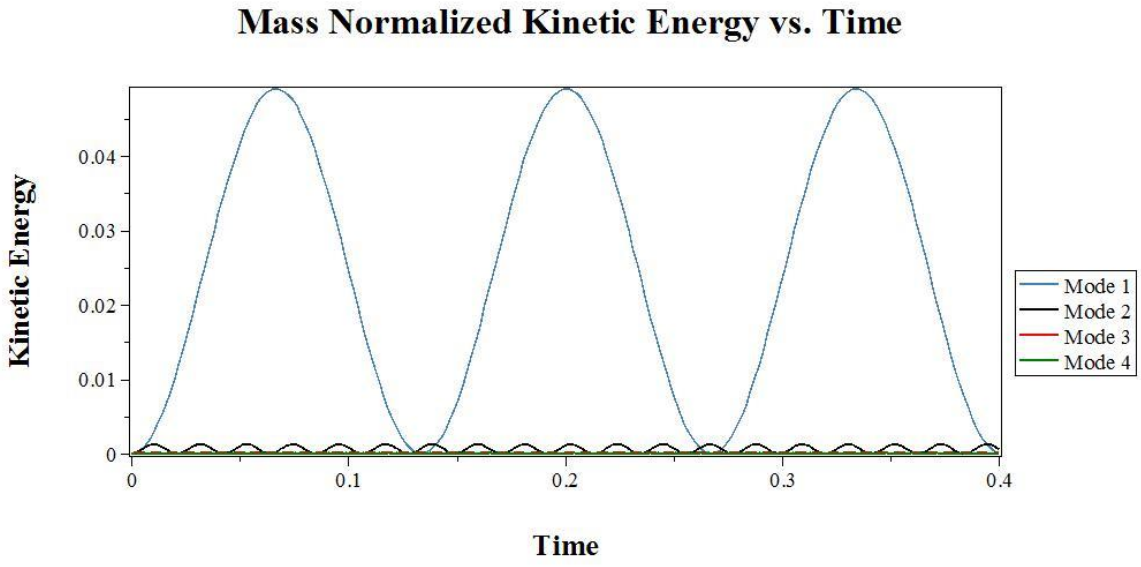

(a)

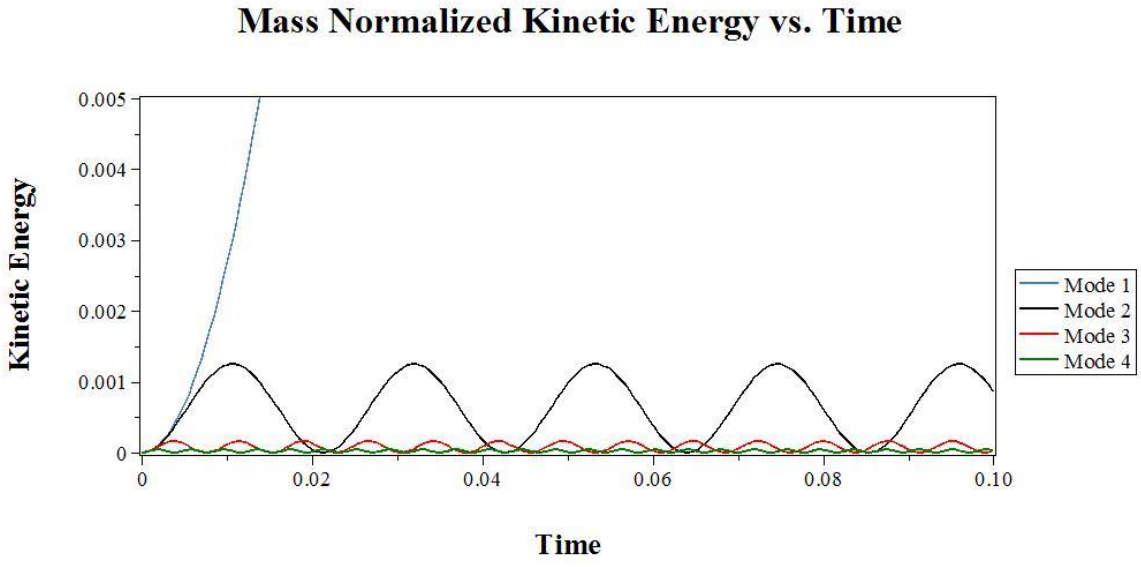

(b)

Figure 3.1. Normalized Kinetic Energy for Cantilever Beam

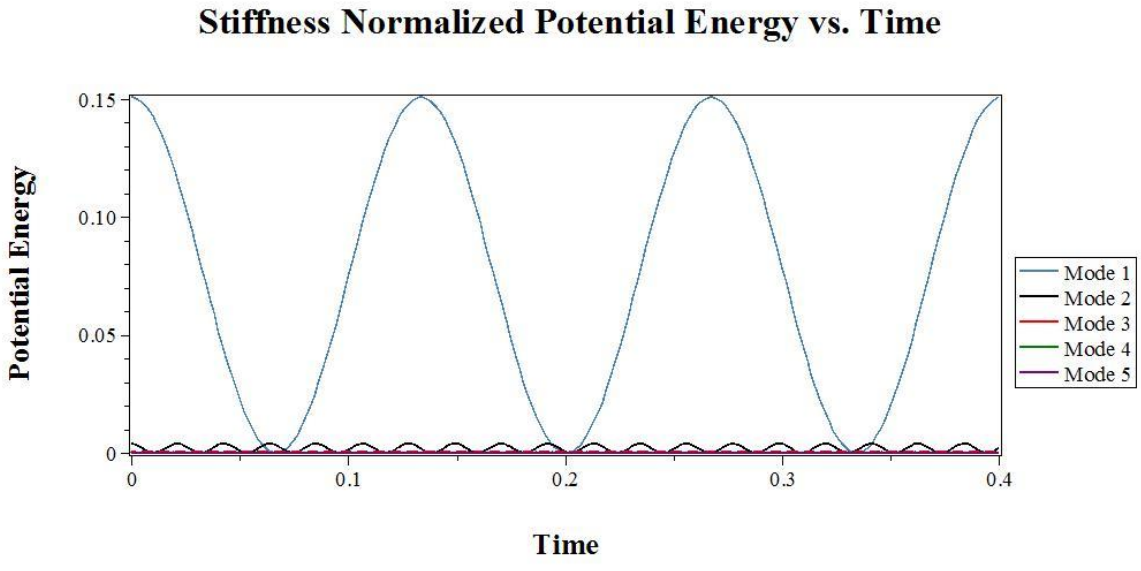

(a)

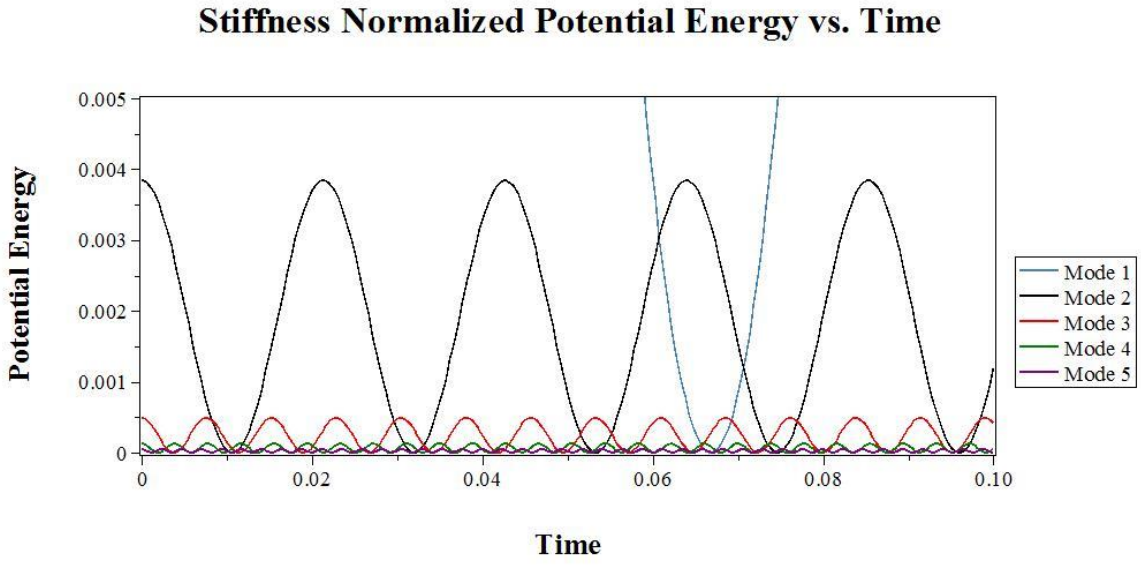

(b)

Figure 3.2. Stiffness Normalized Potential Energy for Cantilever Beam

The potential energy in large-deflection cantilever beams were investigated using ANSYS® and compared with that of the PRBM. The beam end was deflected and the corresponding strain energy was determined using Ansys® and the PRBM®. Young's

Modulus was held constant for each trial in order to simplify the testing. The data shows what has been observed in the past, that the PRBM predicts slightly stiffer segments. The results are shown in Table 3.1. While the PRBM predicts slightly stiffer segments, the potential energy terms are adequately accounted for under static considerations.

Table 3.1. Potential Energy Comparison

Width	Thickness	Length	Beam End Displacement	Potential Energy ANSYS®	Potential Energy PRBM	% Error
0.1	0.1	10	5	10.884	11.216	2.96
0.5	0.1	15	10	75.80	76.77	1.26
0.1	0.5	15	10	1894.29	1919.18	1.30

3.2 EULER-BERNOULLI BEAM MODEL

In continuous vibration models several assumptions are made that allow for the solution of a differential equation to predict the deflection response. The solution is comprised of the homogenous and non-homogenous portions; both the forced and free vibrations are readily solved. The forced portion of the solution is due to the external forcing on the dynamic system. The free vibration is a result of the natural frequency response due to the initial conditions. The equation of a slender cantilever beam undergoing forced vibration, without any system losses is shown below[60]:

$$E \cdot I \cdot \frac{\partial^2}{\partial x^2}\left[\frac{\frac{\partial^2 w(x,t)}{dx^2}}{(1+(\frac{\partial w(x,t)}{dx})^2)^{\frac{3}{2}}}\right] + \rho \cdot \mathrm{A} \cdot \frac{\partial^2 w(x,t)}{dt^2} = F(x,t) \qquad (7)$$

Where w(x,t) represents the transverse deflection, ρ the mass density, A the cross-sectional area, E the Young's Modulus of elasticity, I the mass moment of inertia, and F(x,t) the external forcing function. Under the small-deflection assumption, the nonlinear terms can either be disregarded due to the smallness of their contribution, or be transformed into the following [60]:

$$E \cdot I \cdot \frac{\partial^4 w(x,t)}{\partial x^4} + \rho \cdot \mathrm{A} \cdot \frac{\partial^2 w(x,t)}{dt^2} = F(x,t) \tag{8}$$

It is important to note that the natural frequency for each mode of a cantilever beam can be solved by the eigenvalue equation shown below [60]:

$$\frac{d^4 W(x)}{dx^4} - \beta^4 \cdot W(x) = 0 \tag{9}$$

subject to the boundary conditions: $W(0) = 0, \frac{dW(0)}{dx} = 0, \frac{d^2 W(\mathrm{L})}{dx^2} = 0$, and $\frac{d^3 W(\mathrm{L})}{dx^3} = 0$

where, $$\beta^4 = \frac{\omega^2 \rho A}{EI} \tag{10}$$

and $W(x)$ represents the mode of vibration. Numerous texts tabulate several eigenvalues [60], β, and the natural frequency, ω, is easily found from using Table 3.2 and equation (10).

Table 3.2. Eigenvalues (β) for the First Five Modes of a Cantilever Beam

Mode Number	1	2	3	4	5
Eigenvalue (β)	1.8751	4.6941	7.8548	10.9955	14.1372

The above derivation, however, only applies to small-deflection dynamics. Nonlinear terms in the potential energy arising from nonlinear geometry pose a difficult problem. However, work done by Azrar et al. [61] shows that for a clamped-clamped beam, the change in natural frequency by accounting for the nonlinearity is only 2.22%. Furthermore, [53] shows that the modal participation factor for large-deflection vibrations of a clamped-clamped beam is 99.8598%. The modal participation factor is a method of measuring the relative contribution of each mode of vibration to the total solution [62]. While these results are not specific to the cantilever beam, they do shed light as to the similarities of the small deflection assumption and the large-deflection problems. As suggested, the PRBM predicts the potential energy of the nonlinear beam adequately. Therefore, the next step would be to calculate the natural frequency or the kinetic energy of the PRBM.

3.3 PSEUDO-RIGID-BODY DYNAMIC MODEL

Before a PRBM is suggested, the following assumptions are made relative to the elastic beam:

1.) It has uniform cross-sectional area along its length

2.) It has uniform material properties

3.) The elastic segment is considered to be a slender beam

4.) Only beam end loads are applied

5.) Only non-following forces are considered

A PRBM utilizes all five assumptions. The beam slenderness is important if large deflections are to be considered. Figure 3.3 shows the basic dynamic PRBM for a compliant cantilever beam.

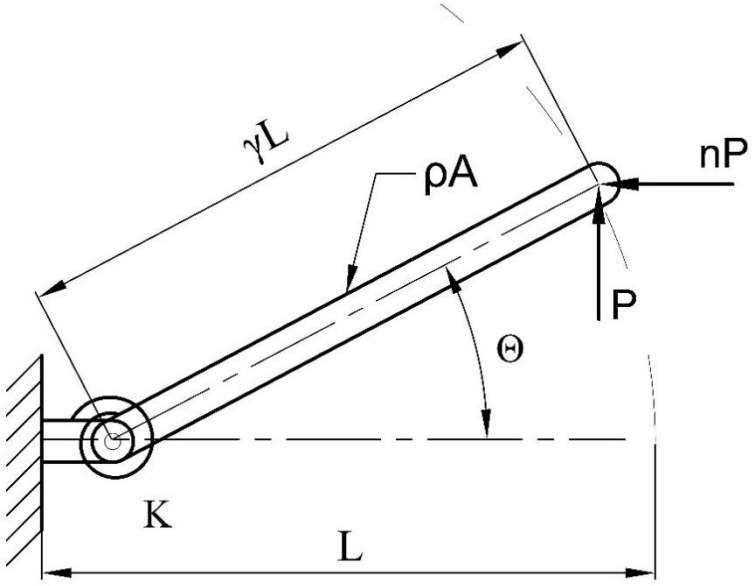

Figure 3.3. Basic Dynamic PRBM

Referring to Figure 3.3, the governing equation of motion may be found using Lagrange's principle. The Lagrange's equation is expressed as:

$$\frac{\partial}{\partial t}\frac{\partial L}{\partial \dot{q}_i} - \frac{\partial L}{\partial q_i} = Q_{q_i} \tag{11}$$

where *L*, termed the Lagrangian,represents the difference between the kinetic and potential energies, q_i the ith generalized coordinate, and Q_{q_i} the ith generalized force.

For the PRBM in Figure 3.3, the kinetic energy (*T*) and potential energy (*U*) are shown in equations (12) and (13), and the Lagrangian (*L*) in equation (14):

$$T = \frac{1}{2} \cdot J \cdot \dot{\Theta}(t)^2 \tag{12}$$

$$U = \frac{1}{2} \cdot K \cdot \Theta^2 + \frac{\gamma L}{2} \cdot m \cdot g \cdot \cos\left(\Theta(t)\right) \tag{13}$$

$$L = T - U \tag{14}$$

where $J = \frac{1}{12} \cdot m \cdot l^2$, represents the polar moment of inertia, K is the PRBM stiffness, Θ is the PRBM angle, g is gravity, and $m = \rho \cdot A \cdot L$ is the mass of the beam. In case of free vibration, the applied force is zero. Substituting these values into equation (11) yields the following equation of motion:

$$\ddot{\Theta}(t) = -\frac{K}{J} \cdot \Theta(t) + \frac{\gamma L}{2J} \cdot m \cdot g \cdot sin\left(\Theta(t)\right) \tag{15}$$

The model derivived has been termed the Polar Moment of Intertia Model, as it utilizes the polar moment of intertia of the beam as the mass term. Lyons [49] provided a similar approach to modeling a single segment, however, gravity was neglected. Given the masses typically associated with compliant segments, one solution is to simply ignore gravity rendering the equation of motion linear; however, it is included here for completeness. Lyons showed that for a wide range of cases the natural frequency was predicted to be within 7% of measured values of beams undergoing large deflection; however, these results are only valid for beams with small masses. The results of this model are summarized later in this chapter.

3.4 IMPROVED PSEUDO-RIGID-BODY DYNAMIC MODEL

In order to minimize the error of the above model with respect to Euler-Bernoulli beam theory, a new model will be presented. This model allows for the calculation of first natural frequency that will have zero error as compared to Euler-Bernoulli theory, while maintaining the simplicity of the PRBM. Consider the system shown in Figure 3.4.

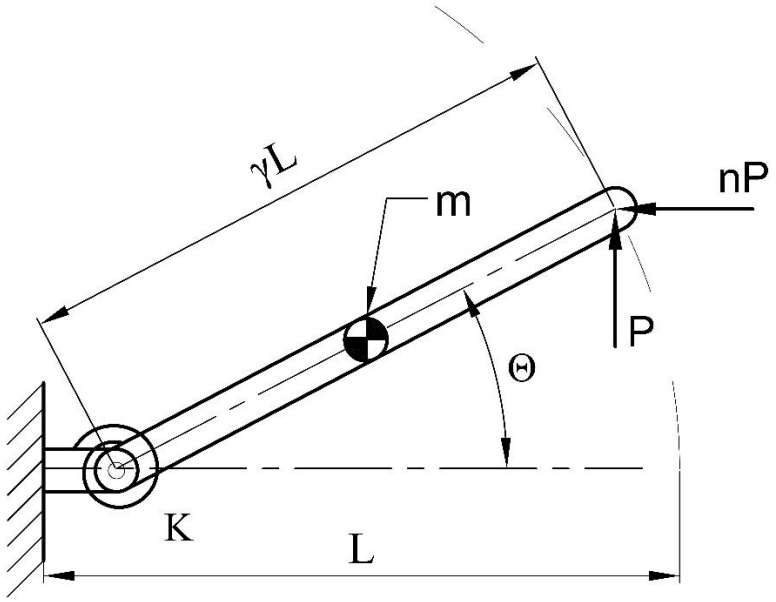

Figure 3.4. Dynamic PRBM Model Based on Characteristic Mass

Deriving the kinetic and potential energies of the system yields:

$$T = \frac{(\gamma L)^2}{4} m \cdot \dot{\Theta}(t)^2 \tag{16}$$

$$U = \frac{1}{2} \cdot K \cdot \Theta^2 + \frac{\gamma L}{2} \cdot m \cdot g \cdot \cos\left(\Theta(t)\right) \tag{17}$$

and substitution into equation (11) gives the following equation of motion:

$$\ddot{\Theta}(t) = -\frac{4 \cdot K}{(\gamma L)^2 \cdot m} \cdot \Theta(t) + \frac{4}{2\gamma L} \cdot g \cdot sin\left(\Theta(t)\right) \tag{18}$$

As with the first dynamic model, the gravity may be viewed as an external forcing function. The natural frequency of the system found by comparing the equation of motion to that of the equation below:

$$\ddot{\Theta}(t) + \omega^2 \cdot \Theta(t) = 0 \tag{19}$$

Euler-Bernoulli beam theory gives the first natural frequency of a cantilever beam as [60]:

$$\omega = \frac{\beta^2}{L^2}\sqrt{\frac{EI}{\rho A}} \tag{20}$$

where ρ is the linear density of the beam, and A the cross-sectional area. Equating equation (20) and the natural frequency of equation (18) gives a mass value equal to:

$$m = \frac{4K\rho AL^2}{\gamma^2 \beta^4 EI} \tag{21}$$

This PRBM approach is an approximation technique that lumps the potential energy of large deflections at a single point, using the methodology recently developed. In the same spirit, it is deemed rational to assume that the mass may be lumped at an appropriate point. This approach will yield zero error in natural frequency when

compared to the Euler-Bernoulli beam theory. The main goal of this method is to reconcile any small approximation errors between the PRBM and Euler-Bernoulli beam theory methods. This method has been termed the Parametric Point Mass Model, due to the dependency of the mass term on the PRBM parameters. It is important to note that the term parametric here does not refer to classic stability problems associated with traditional nonlinear dyanimc systems. The alternative to this model is to place the physical mass at the center of the pinned segment, this alternative approach is termed the Physical Point Mass Model.

Table 3.3 shows sample cases for the Polar Moment of Interia, Physical Point Mass, and Parametric Point Mass Models. In this case both mass density and Young's modulus of elasticity were held constant. As seen, the Parametric Point Mass Model is the only one with zero error as compared to the Euler-Bernoulli beam theory and also has the closest results with ANSYS® with regards to natural frequency. This results is as expected due to the formulation of the mass term used in the Parametric Point Mass Model. However, all three models predict results very well. The implementation of models can be left to the end user to decide the degree of accuracy which is needed. The test cases were run using a material having a Young's Modulus of 60 GPa and a mass density of 183 Kg/m^3.

Table 3.3. Natural Frequency Comparisons

Width, thickness, Length (*wxtxl*)	Polar Moment of Inertia	Physical Point Mass	Parametric Point Mass	Euler-Bernoulli	ANSYS®
.020x0.00125x0.11	9.05	10.45	9.62	9.62	9.62
.0405x0.0025x.2	5.47	6.33	5.82	5.82	5.82
.025x0.0005x.01	438.29	506.09	465.49	465.49	465.27

3.5 SYSTEM LOSSES IN THE PRBM

The next step in the construction of a dynamic model is to include system losses such as damping in order to mimic a real world scenario. Many forms of damping exist however the use of viscous damping in modeling is perhaps the most straightforward and most widely accepted in engineering practice. The addition of this term is very simple in the proposed models is shown in below in equation (22) and (23) for the Polar Moment of Inertia Model and the Point Mass Models, respectively:

$$\ddot{\Theta}(t) = -\frac{K}{J}\cdot\Theta(t) - 2\sqrt{\frac{K}{J}}\zeta\cdot\dot{\Theta}(t) + \frac{\gamma L}{2J}m\cdot g\cdot sin\left(\Theta(t)\right) \tag{22}$$

$$\ddot{\Theta}(t) = -\frac{4K}{(\gamma L)^2 m}\Theta(t) - 2\sqrt{\frac{4K}{(\gamma L)^2 m}}\zeta\dot{\Theta}(t) + \frac{4}{2\gamma L}\cdot g \cdot sin\left(\Theta(t)\right) \tag{23}$$

However, the damping ratio, ζ , is typically determined experimentally and thus design of mechanisms for desired behavior where damping will affect the outcome will be difficult to model. The approach would be iterative until a solution that displays desired damping characteristics is found. The damping of a single segment has been found to be related to how close to the yield point the segment is vibrating [63]. To observe this behavior, an experimental study was conducted by deflecting a beam nearly one-half of its length and letting it vibrate freely. The first mode shape was extrapolated by implementing a digital band-pass filter about the lowest measured frequency peak. The plot of the peak envelope may be seen in Figure 3.5.

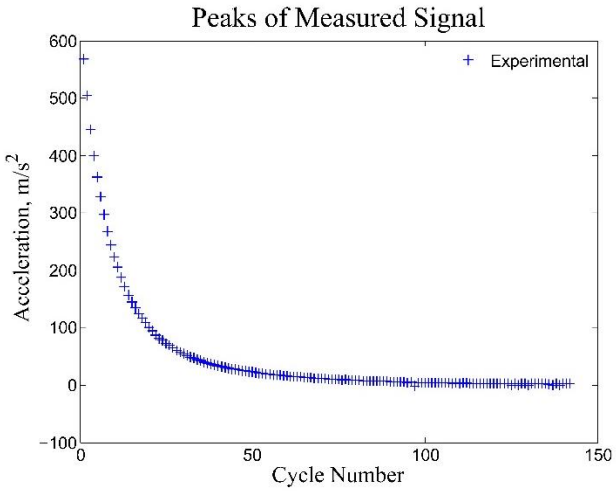

Figure 3.5. Peak Envelope Plot of Measured Acceleration

Curve fitting this measured response shows a two-term exponential decay rate. The general equation is shown in equation (24):

$$f(x) = Ae^{-Bx} + Ce^{-Dx} \tag{24}$$

Where A and C represent the magnitude of each terms contribution to the decay, and B and D define the rate of decay.

While the exact behavior would be difficult to model, a two-staging damping ratio is readily implementable. Solving equation (15) or equation (18), and then comparing the deflection obtained to a defined ranges of deflection, such as 100% to 10%, and 10% to 0% of the beam length, a value for the damping ratio can be obtained for each regime of vibration based on damping ratios measured from experimental results. This allows for the damping ratio to be larger in the large-deflection region, and a smaller value in the small-deflection regime. At the time of transition from large to small deflection in the time response, the next zero crossing in time is found and the displacement and velocity constraints are imposed on the next regime. For example, if the last peak for the large-deflection response occurs at time t, the small-deflection damping ratio value will be imposed at the immediate next zero crossing in time. Going forward, the solution to the differential equation uses initial conditions of zero displacement and a nonzero velocity. The proposed method may be implemented for any number of defined damping ratios. For example, if it is determined that the damping ratio changes significantly for diplacements over 10%, 30%, and 50% of the beam length, the damping ratios can be calculated in a similar fashion, by solving the differential equation of motion and using a damping ratio unique to each regime. More complex damping models may also be

implemented, particularly for multi-degree-of-freedom systems. While this method does not explicitly address structural damping, the net effects are included in the damping model proposed. Other losses such as that due to Coulomb friction may be readily accounted for, however, as needed, and will be discussed in application to mechanisms in a later section.

3.6 EXPERIMENTAL VALIDATION

In order to determine the validity of the proposed models, experiments are conducted that focus on the transient response of the single segment and the natural frequency measured. The experimental setup consisted of a cantilever beam made of Delrin®, an acetal co-polymer, and measuring 2.0 in. x 0.125 in. x 11.0 in. The beam is secured to a large table with a clamp, and an accelerometer placed at the beam tip in the center of the beam. The beam is deflected 6 in., approximately one-half of the beam length, and allowed to vibrate freely until coming to rest. The first mode of vibration is isolated from the experimental data using a hardware band pass filter along with the first peak in the frequency spectrum. The band pass filter is +/- 5 Hz of this peak, eliminating frequencies above and below this band. The experimental data is shown in Figure 3.6.

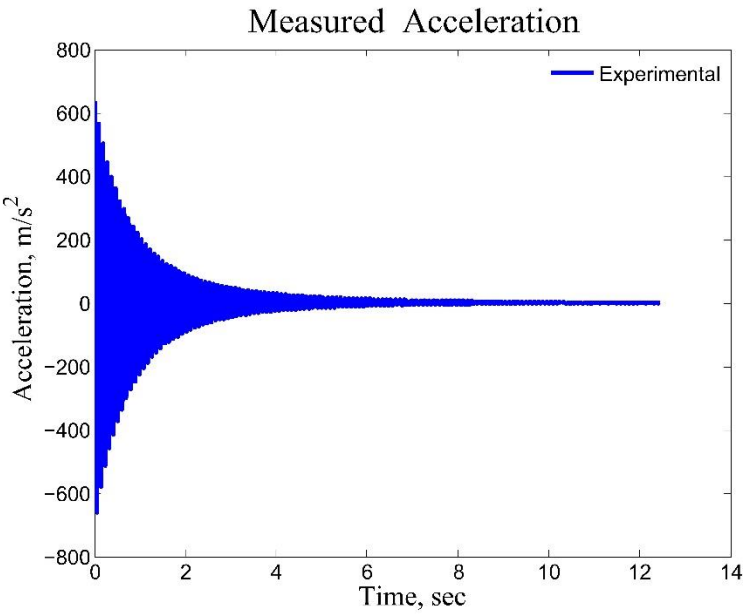

Figure 3.6. Measured Acceleration of Delrin® Beam

The damping ratio, ζ, is calculated using the logarithmic decrement method over the first ten peaks of the large-deflection acceleration data. The model is then run to determine a time at which the beam end deflection was less than 15% of the beam length. At this time, a new damping ratio is calculated from the experimental data and amplitude decays to a sufficiently small value. Figure 3.7 shows a Fast Fourier Transform (FFT) of the predicted and measured signals. As observed, the dynamic model shows good correlation with the measured signals, both in terms of amplitude, frequency, and band width. The chosen dynamic PRBM uses the Polar Moment of Inertia Model.

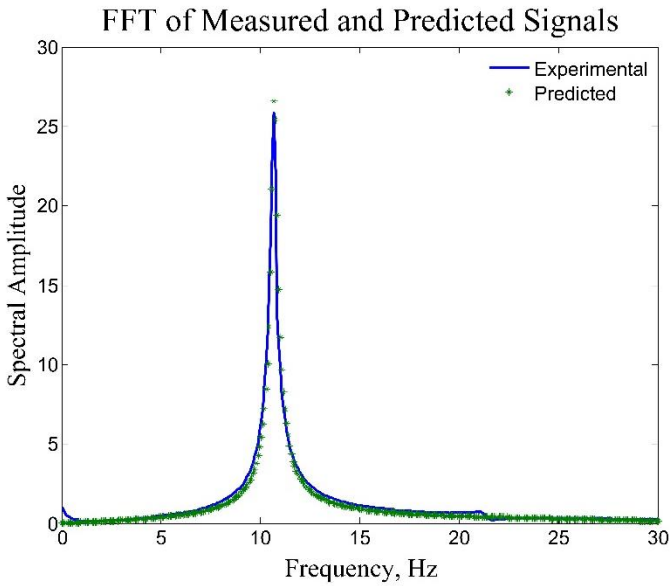

Figure 3.7. FFT of Measured and Predicted Signals for Delrin® Beam

Figure 3.8(a) shows the predicted and measured acceleration values. Note that Figure 3.8(b) is the magnified portion of the intial release of the beam.

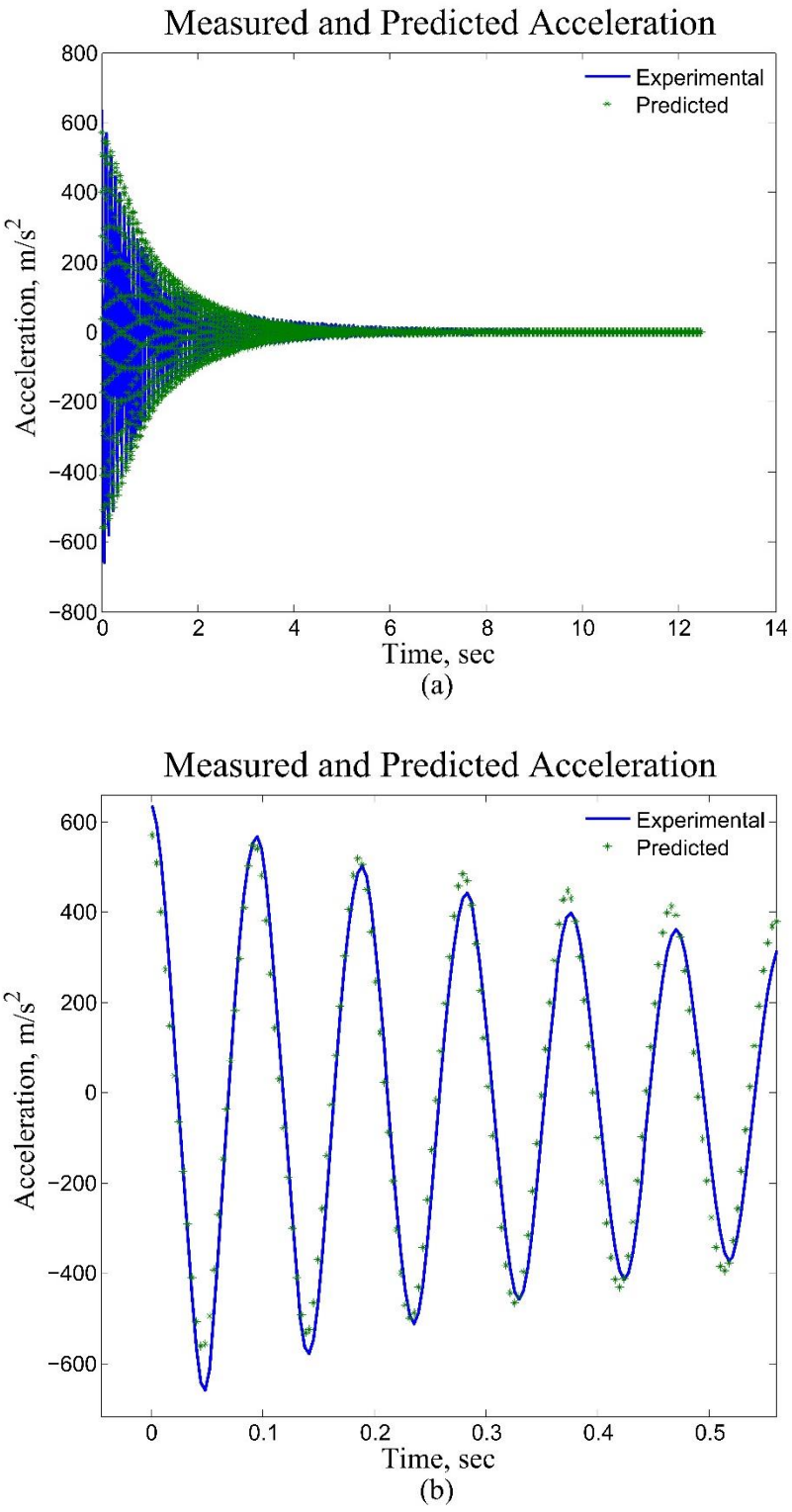

Figure 3.8. Measured and Predicted Time Acceleration Histories for Delrin® Beam

Another way of comparing the plots is then to show the positive peak envelope of the signal. The predicted and measured values match closely; however, as the deflection increases, so does the error. The multi-stage damping ratios could help alleviate this problem, however, the current results are deemed suitable as a first approximation. The peak envelope plot is shown in Figure 3.9.

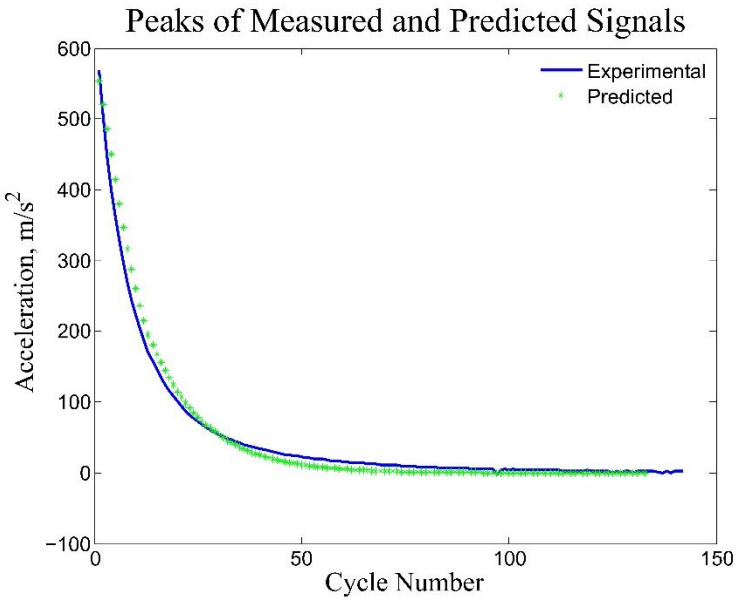

Figure 3.9. Peak Envelope Plot of Measured and Predicted Signals for Delrin® Beam

The area under the peak envelopes was used as a method to determine the suitability of the transient model. The integral of the force deflection curve represents energy, and so the integral of the acceleration profile is a measure of energy, but is not the absolute value. This method can be used to investigate trends of the energy profiles. To do this the *trapz* command in Matlab® was used on the data set displayed above. For

the above case the integrals were computed over the entire dataset and the percent difference was found to be 0.0863%.

Another test was conducted on a metallic specimen of aluminum. This test utilized the Parametric Point Mass Model. The FFT and peak envelope plots of acceleration are shown below in Figure 3.10 and Figure 3.11 for a beam measuring 2.05”x.0375”x11.75”. The initial deflection of the beam was 2.75 inches. A three stage damping regime was implemented, with conditions of 8.5% and 2% of the beam length. If the deflection falls above 8.5% of the beam length, the highest damping value is used. If the deflection is between 8.5% and 2%, the medium damping value is used, and if below 2% the lowest value is used. The damping values were recorded over numerous peaks from the experimental data and times which aligned with the simulation. Discrepancies noted are easily attributed to the difficulty of releasing the beam. Any small variations in the manual release of the beam will result in changes to the initial conditions, therefore changing the response.

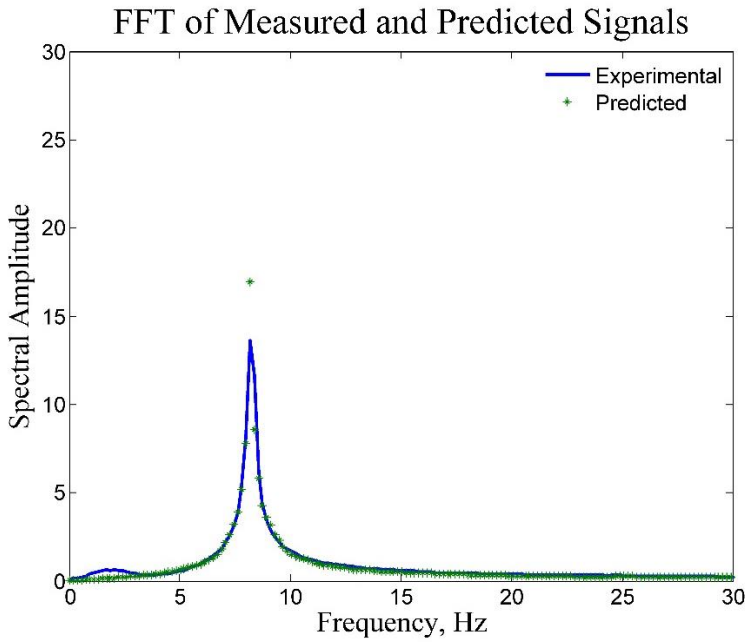

Figure 3.10. FFT of Measured and Predicted Signals for Aluminum Beam

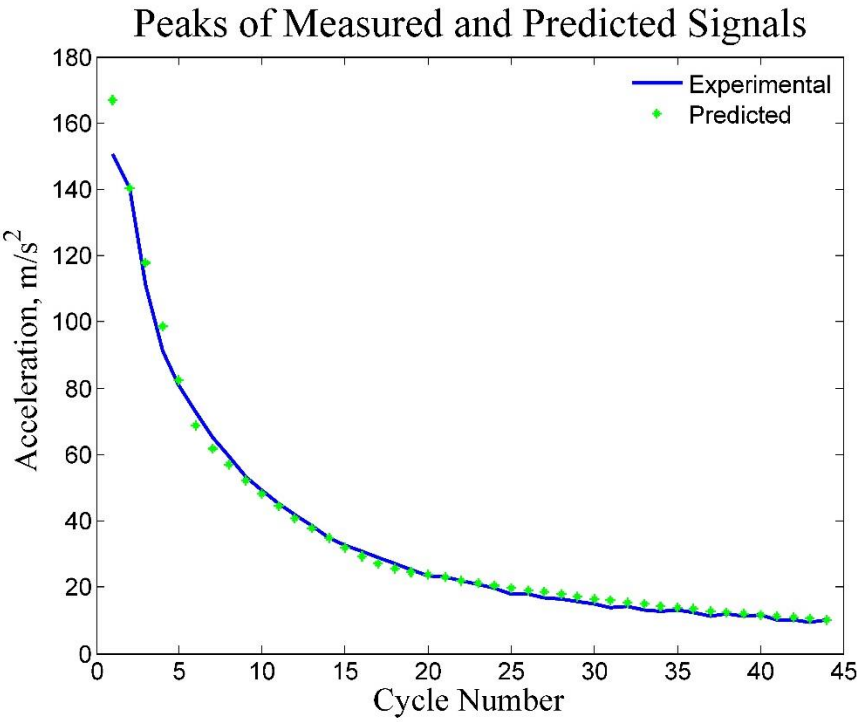

Figure 3.11. Peak Envelope Plot of Measured and Predicted Signals for Aluminum Beam

Again, the area under the peak envelopes was used as a method to determine the suitability of the transient model. For the above case the integrals were computed over the entire dataset and the percent difference was found to be 1.9340%.

3.7 APPLICATIONS TO MECHANISMS

In order to expand the proposed method to mechanisms, a parallel guiding mechanism was constructed. A new equation of motion was derived. The formulation is centered on the fact that the parallel guiding mechanism is a four bar mechanism and thus single degree of freedom mechanism. A schematic of the parallel guiding mechanism is shown in Figure 3.12.

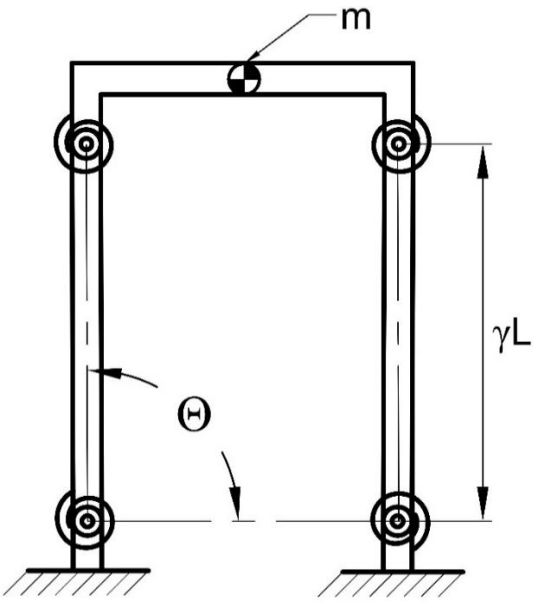

Figure 3.12. PRBM of Parallel Guiding Mechanism

The energies of the system can be calculated and traditional Lagrangian dynamics implemented. Calculation the potential and kinetic energies of the system is shown in equations (25) and (26), respectively based on the Polar Moment of Interia Model:

$$U = \frac{4}{2} \cdot K \cdot \Theta(t)^2 + \frac{\gamma L}{2} \cdot \mathrm{g} \cdot \cos\left(\Theta\left(t\right)\right)\left(2m + M\right) \tag{25}$$

$$T = J \cdot \dot{\Theta}\left(t\right)^2 + \frac{1}{2} \cdot m \cdot (\gamma L)^2 \cdot \dot{\Theta}(t)^2 \tag{26}$$

Implementing these into expressions in equation (11) gives the following equation of motion:

$$\ddot{\Theta}\left(t\right) = -\frac{4K\Theta}{2J + m(\gamma L)^2} - 2\zeta\sqrt{\frac{4K}{2J + m(\gamma L)^2}}\dot{\Theta}\left(t\right) + \frac{\gamma L}{2}\mathrm{g}\sin\left(\Theta\left(t\right)\right)\left(2m + M\right) \tag{27}$$

Where M is the mass of the side links, either the parametric mass or physical mass will work in this case, and m represents the mass of the coupler. A mechanism was constructed from Delrin® and tested. The mechanism was built from links .75”x.125”x10.5” with a coupler mass of 65 grams. The initial deflection of the mechanism was 4.5 inches in the horizontal. As was the case for the single segment model the natural frequency of the mechanism was predicted adequately as shown in Figure 3.13.

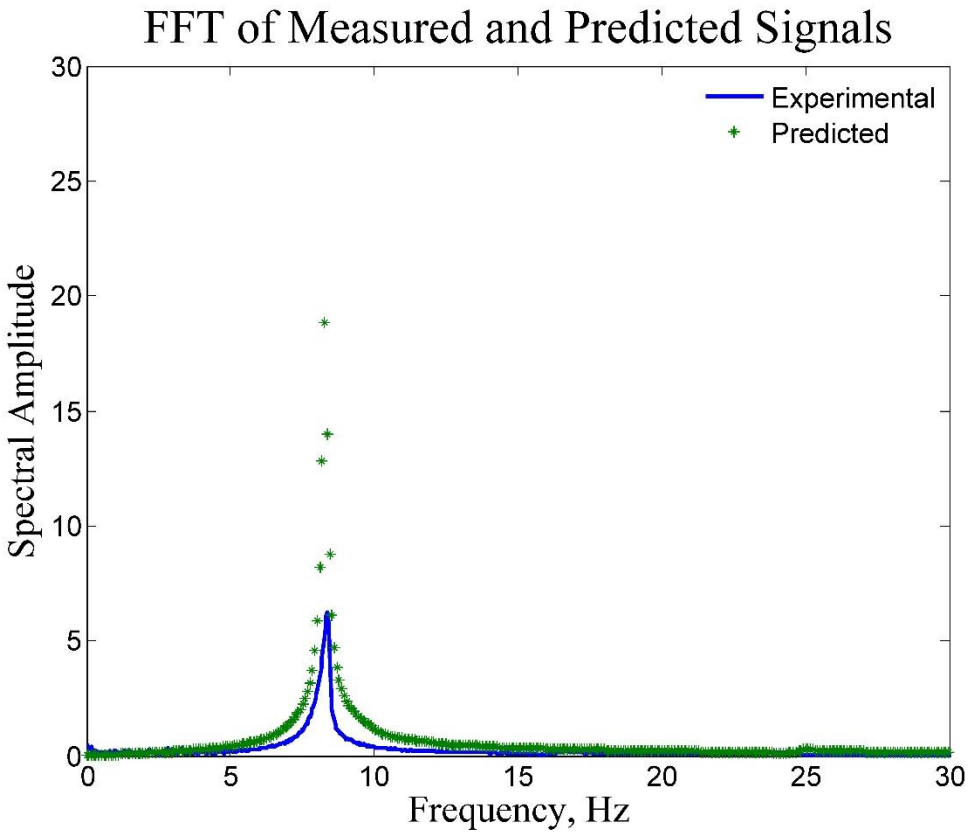

Figure 3.13. FFT of Measured and Predicted Signals for Parallel Guiding Mechanism

Again, any errors will be magnified by the discrepancy in natural frequency, and the peak envelope plot again is used to compare the model in Figure 3.14. The integral error was found to be 3.03%.

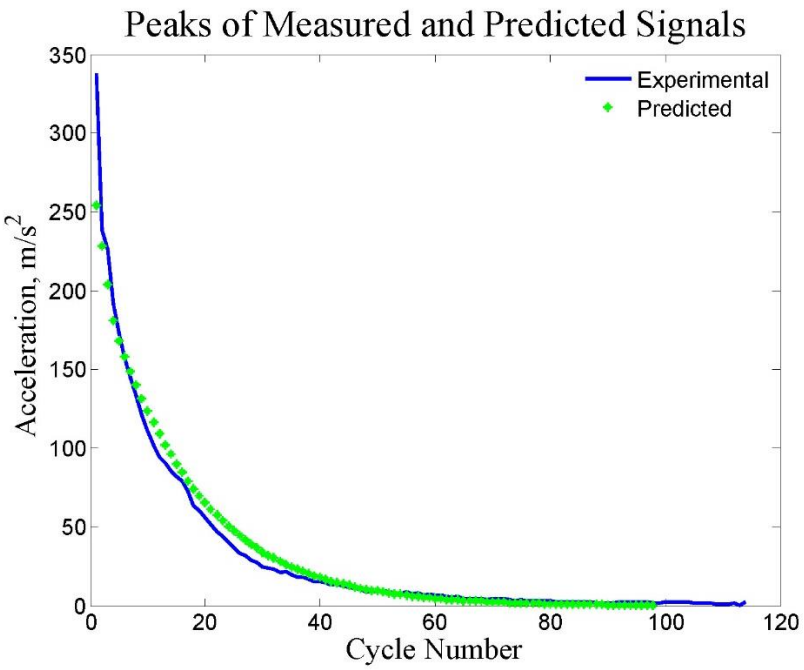

Figure 3.14. Peak Envelope Plot of Measured and Predicted Signals for Parallel Guiding Mechanism

3.8 CONCLUSIONS

Dynamic models capturing the transient behavior of a freely vibrating compliant segment were developed. An improved version of this model was developed to yield zero error with traditional small deflection dynamic techniques. A two stage damping regime, where the damping constant, ζ, depends on the local maximum cyclic deflection is derived, with the ability to expand to multiple stages. Implementation of two and three stage damping regimes were given with experimental results. Applications to mechanisms are investigated by means of implementing the transient model in a parallel guiding mechanism. The natural frequency and peak envelope are used to gauge the proposed model's viability with experimental results, with acceptable error.

4. CONSTANT-FORCE SLIDER MECHANISMS

4.1 DEVELOPMENT OF COMPLIANT CONSTANT-FORCE SLIDER MECHANISM

Mechanisms with unique force deflection curves have been of interest to the engineering community for some time. These mechanisms can find niche applications in many industries. Recently research has been re-ignited on the design and analysis of constant-force slider mechanisms. The earliest constant-force mechanisms can be found in [30] and [37]. These mechanisms utilized six bar mechanisms with linear springs to achieve a constant force at the output port. In [36], development of multiple configurations of compliant constant-force slider mechanisms was presented. In Boyle [48] the dynamic characteristics of these compliant slider mechanisms was investigated with varying results. In Karthik [56] a modular design of multiple compliant segments was present with promising experimental results. The present work expands on the work done in [56] with investigations into both the compressive and extensive characteristics of compliant constant-force mechanisms. First the static response will be investigated from a virtual work approach. An overview of the optimization schemes used to determine appropriate link length ratios will be given. Next considerations for mass effects and friction will be given, something unique not done in previous work. Finally experimental results obtained from a universal testing machine (UTM) will be given to confirm the presented modeling for a cycle of compression and extension of the compliant mechanism.

4.2 DIMENSIONAL SYNTHEIS OF CONSTANT-FORCE SLIDER MECHANISMS

Four bar mechanisms are very popular in engineering and mechanical design due to their simplicity. The four bar displays characteristics of good mechanical advantage and 1 degree of freedom. Murphy [18] generated design iterations of a constant-force mechanism by implementing flexible segments in place of linear springs. Out of this work twenty-eight configurations of constant-force mechanisms were generated. A generalized schematic of the four bar mechanism is shown below.

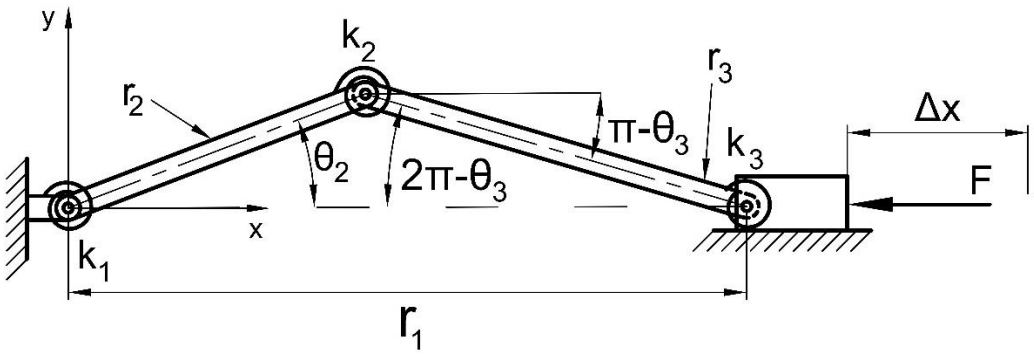

Figure 4.1. PRBM of Generic Slider

Howell [19] furthered this work by classifying the 28 mechanisms into several classes and performed dimensional synthesis to generate optimized values for link length and stiffness ratios. The five classes are summarized below.

For class 1A mechanisms shown in Figure 4.2 one rigid link of the four bar mechanism is replaced with a flexible segment. This replacement eliminates one pin

joint at an end of the mechanism, and also constrains the flexible segment to be a fixed pinned segment.

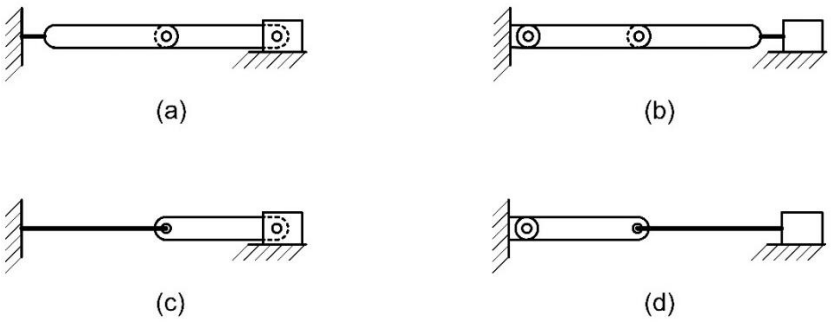

Figure 4.2. Class 1A Constant-Force Mechanisms

Class 1B mechanisms are shown in Figure 4.3. For this case the mechanisms either consist of small length flexural pivots in place of pin joints or a flexible link fixed to the rigid link.

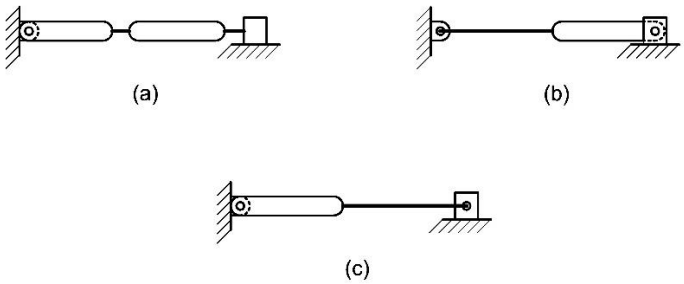

Figure 4.3.Class 1B Constant-Force Mechanisms

Class 2A mechanisms are shown in Figure 4.4. The mechanisms are generated by replacing the center pin joint and another pin joint by small length flexural pivots.

Figure 4.4. Class 2A Constant-Force Mechanisms

Class 2B mechanisms, shown in Figure 4.4 are created by replacing the two pin joints at the end of the mechanism with flexible links.

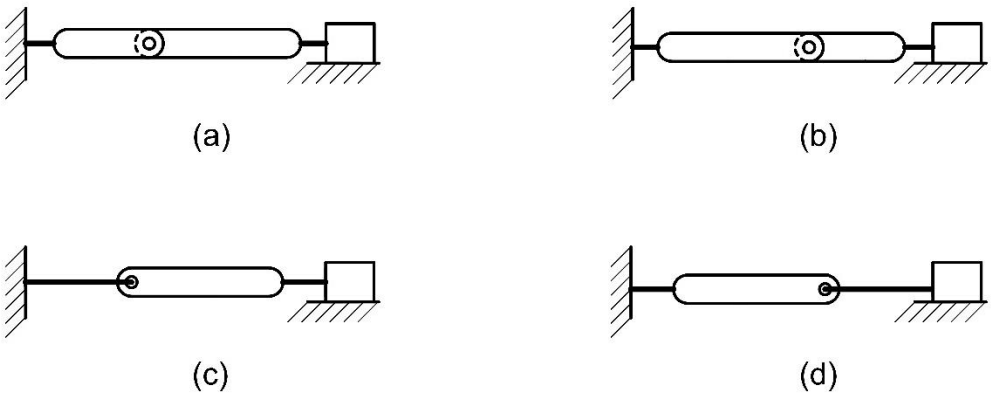

Figure 4.4. Class 2B Constant-Force Mechanisms

Class 3 Mechanisms are created by replacing each pin joint with a flexible link. It is important to note that for all classes the mechanisms on the right are created by replacing the order of the links on the left i.e. r_2 becomes r_3 and vice versa.

Figure 4.5. Class 3 Constant-Force Mechanisms

Furthermore, Midha et al. [37] presented an alternative solution to using pin joints. A sliding contact pair may be modeled as a pin joint, as shown in Figure 4.6.

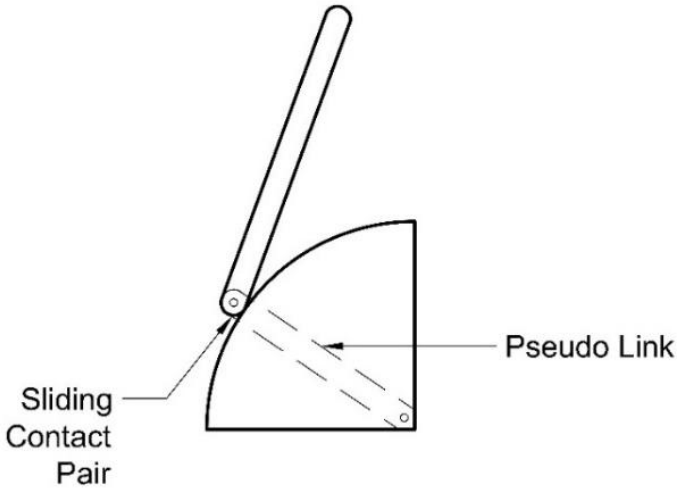

Figure 4.6. Sliding Contact Pair as Pseudo Link

Howell et al. [36] also presented used the principle of virtual work to generate an equation relating the output force to the slider displacement. Assuming that the slider is in line with the fixed point of r_2 then the force at the slider can be found as:

$$F = \frac{r_3 \cos(\theta_3)[k_1\theta_2 + k_2(2\pi + \theta_2 - \theta_3)] + r_2 \cos(\theta_2)[k_2(2\pi + \theta_2 - \theta_3) + k_3(2\pi - \theta_3)]}{r_2 r_3 \sin(\theta_2 - \theta_3)} \quad (28)$$

Where:

$$\theta_2 = \cos^{-1}\left(\frac{r_1^2 + r_2^2 - r_3^2}{2r_1 r_2}\right) \quad (29)$$

$$\theta_3 = \sin^{-1}\left(\frac{-r_2 \sin(\theta_2)}{r_3}\right) \quad (30)$$

$$\Phi = \frac{\cos(\theta_3)\theta_2 + K_1(\theta_2 - \theta_3)}{\sin(\theta_2 - \theta_3)} + \frac{\cos(\theta_2)[K_1(\theta_2 - \theta_3) - K_2(\theta_3)]}{R\sin(\theta_2 - \theta_3)} \quad (31)$$

$$F = \frac{k_1}{r_2}\Phi \quad (32)$$

Where k_i represents the stiffness from the PRBM and r_i represents the link lengths of the PRBM. The above derivation neglects mass effects, if the slider was parallel to gravity, and any friction effects. To account for friction and mass effects one needs simply to subtract (or add) the expressions for these terms from the above equation. A more in-depth analysis will be given in the following chapters.

4.3 OPTIMIZED DIMENSIONAL SYNTHESIS

The intent of dimensional synthesis is to derive a mechanism that will yield a constant or nearly constant output force for a large range of input angles, i.e. stiffness and link length ratios. Using equation (31) the nondimesional force, Φ, can be plotted for various R values to investigate the behavior of varying link length ratios. For a class 1A-c or d mechanism, the stiffness ratios are ignored as there is only one spring. Howell was

able to implement IMSL optimization and used *dnconf* to dimensionally synthesize in-line constant-force slider mechanisms [19]. The exercise was done by minimizing the non-dimensional force over a range of specified non-dimensional slider displacements. The non-dimensional slider displacement is given by:

$$\frac{\Delta x}{r_2 + r_3} \tag{33}$$

The value of the non-dimensional force was calculated at 50 evenly spaced points along the non-dimensional displacement. The optimization scheme us summarized below:

$$\text{Find X}=\begin{Bmatrix} K_1 \\ K_2 \\ R \end{Bmatrix} = \begin{Bmatrix} \frac{k_2}{k_1} \\ \frac{k_3}{k_1} \\ \frac{r_2}{r_3} \end{Bmatrix} \tag{34}$$

Which minimizes

$$f(x) = \frac{|\Phi|_{\max}}{|\Phi|_{\min}} = \Xi \tag{35}$$

Subject to

$$k_i \geq 0 \tag{36}$$

$$r_i > 0 \tag{37}$$

$$k_1 \neq 0 \tag{38}$$

Where Ξ represents the deviation from constant force over the entire range of motion. In this case, maintianing Ξ as close to one as possible will yield a more constant force mechanism. Recently Karthik [56] performed optimization using *fmincon* in Matlab® and a finer resolution on spacing. In addition to these differences, the input link rotation was used as input to the optimization instead of non-dimensionalized displacement. Offset slider mechanisms were also considered in this study. The summary of this investigation for inline mechanisms is given below in Table 4.1. The table is useful due to the non-dimensional values. Using link 2 as a free choice, the table will then allow the user to determine the length of link 3, and the value of the spring constant for link 3. Note that for every non-dimensional displacement, the first value listed was found in [19] and the second value was found in [56].

Table 4.1 Link Length and Spring Ratios for Constant-force Mechanism Classes

Class	$\Delta x / (r_2 + r_3)$	R	K1	K2	Ξ	Φ
1A	.16[13]*	.8274	0	0	1.0031	.4537
	.16 [48]*	.8271	0	0	1.0031	.4536
	.40	.8853	0	0	1.0248	.4773
	.40	.8849	0	0	1.0244	.4752
1B	.16	1	0	0	1.0570	2.0563
	.16	1	0	0	1.0570	2.0373
	.40	1	0	0	1.1591	2.1513
	.40	1	0	0	1.1591	2.1018
2A	.16	.3945	.1906	0	1.0016	.9575
	.16	.3470	.1637	0	1.0006	.8934
	.40	.4323	.2237	0	1.0061	1.0466
	.40	.3911	.1927	0	1.0027	1.0111
2B	.16	.7591	0	.1208	1.0030	1.2259
	.16	.7784	0	.0913	1.0028	.5044
	.40	.8441	0	.1208	1.0241	2.2154
	.40	.8435	0	.1208	1.0239	.5416
3	.16	2.6633	1	12.6704	1.0002	3.4016
	.16	2.5641	1.0621	12.4888	1.0007	3.5628
	.40	2.0821	1	9.3816	1.0052	3.6286
	.40	2.0857	.9919	9.3837	1.005	2.6100
*First value for each displacement row is from [13] second value is from [48]						

Karthik [56] investigated numerous effects of mechanism parameters such as varying offset ratios, non-zero initial starting angles, and varying link length ratios. The reader is referred to this work for a more concise and in depth analysis of these effects.

4.4 MASS AND FRICTION EFFECTS

The design of a modular constant-force mechanism was first attempted by Evans and Howell [40] by the construction of a robot end effector. This end effector was constructed such that a total of four slider mechanisms were used in an axisymmetric fashion. The prototype of this mechanism can be seen in Figure 4.7 [48].

Figure 4.7. Compliant Constant-Force Robot End Effector

Experimental testing was done to characterize the force deflection curve of this mechanism. For one complete cycle of compression and extension, the results are shown in Figure 4.8 [40].

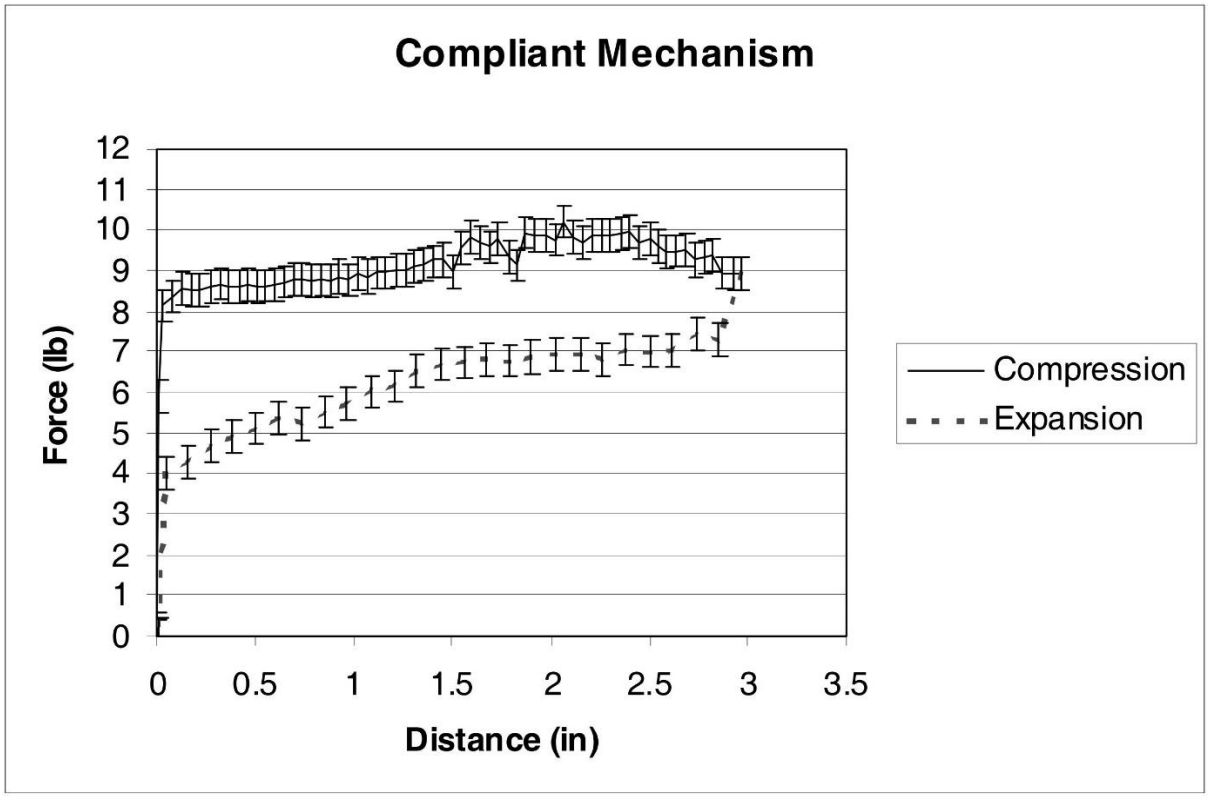

Figure 4.8. Force Deflection Curve for Robot End Effector

A few characteristics of the test data should be noted. First is the ramping of the compression stroke. A slight linear slope is noticed throughout the entire range of motion. Secondly, at the end of the compression stroke and start of the extension stroke, a significant and instantaneous drop in force is noticed. Lastly, the ramp effect on the

extension stroke is a negative slope however is not identical to the compression stroke. This testing was done such that acceleration effects could be neglected.

Jenuwine and Midha [35] developed an exact constant-force single input multi output port mechanism for accelerated pavement testing. The mechanism was a rigid body mechanism where the energy storage was obtained from linear springs. Figure 4.9 shows the rigid body mechanism.

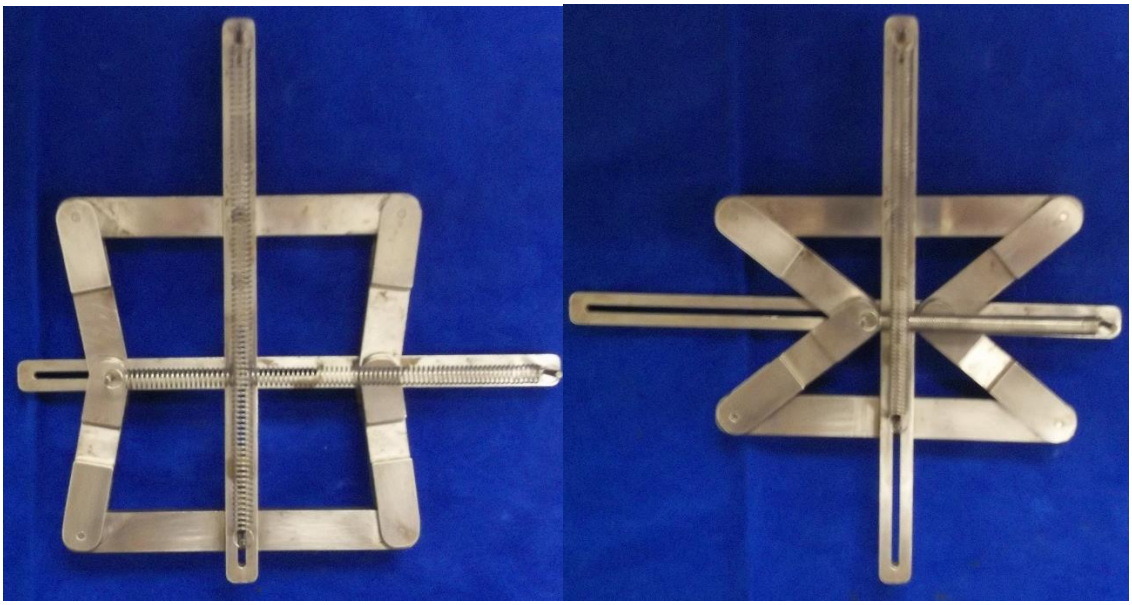

Figure 4.9. Constant-Force 6-Bar Mechanism in Deflected and Undeflected Position

Interestingly, the results from this testing appear to show nearly the same trends as those in [40]. Figure 4.10 [64] shows the summary of the results.

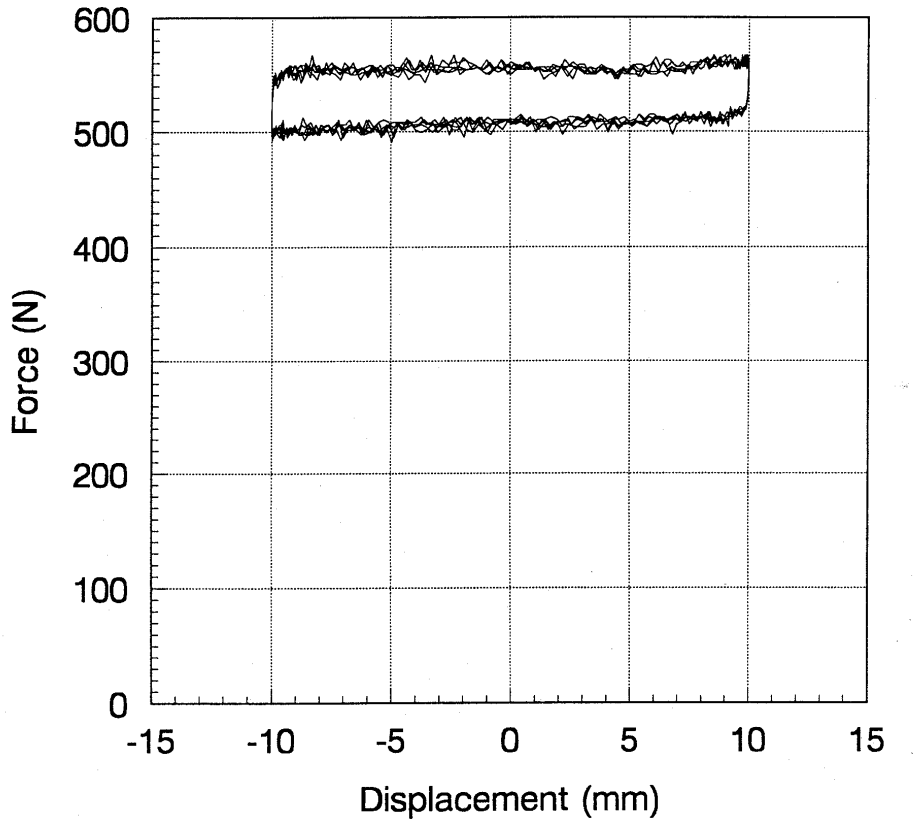

Figure 4.10. Constant-force 6-Bar Test Results

In this case mass effects cannot be ignored. Based on the results of these two seemingly dissimilar mechanisms, and the fact that the trends of the curves are very similar it is proposed that Coulomb friction has a profound effect on the response of the constant-force slider mechanisms. However, in order to analyze this issue, a mechanism will first be developed. Turning attention to Karthik [56] a modular compliant slider mechanism was developed utilizing radial symmetry. A class 1A-d mechanism was

developed having five compliant segments and no pin joints. Initial testing was given and below is the plot of the experimental data in Figure 4.11.

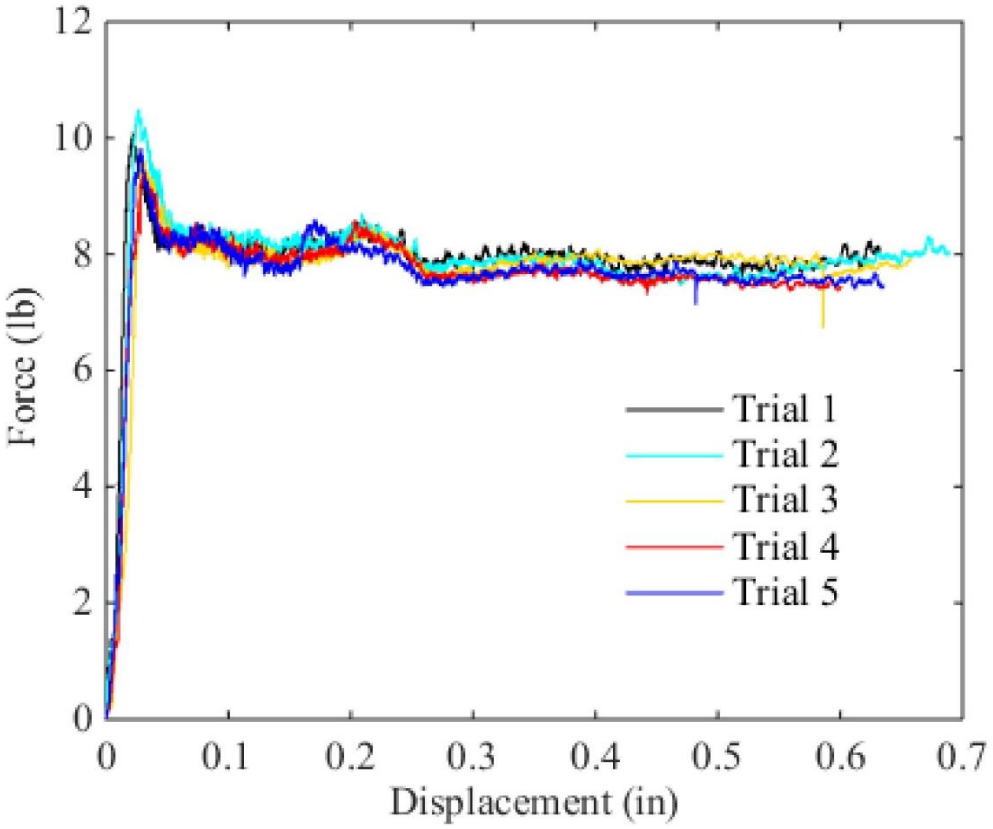

Figure 4.11. Modular Constant-Force Compliant Mechanism Test Results [56]

However the friction and mass effects were not considered in any analysis given in [19] or [56]. A solid model rendering of the mechanism under consideration is shown in Figure 4.12.

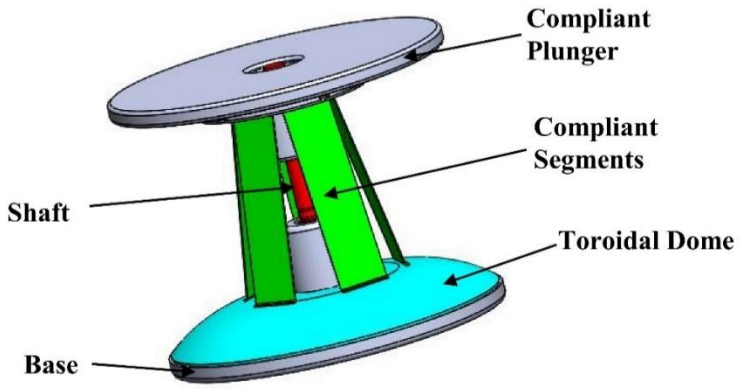

Figure 4.12. 3D Rendering of Modular CFM

In order to account for mass and friction effects a free body diagram approach is utilized. The PRBM of the mechanism under consideration is shown in Figure 4.13.

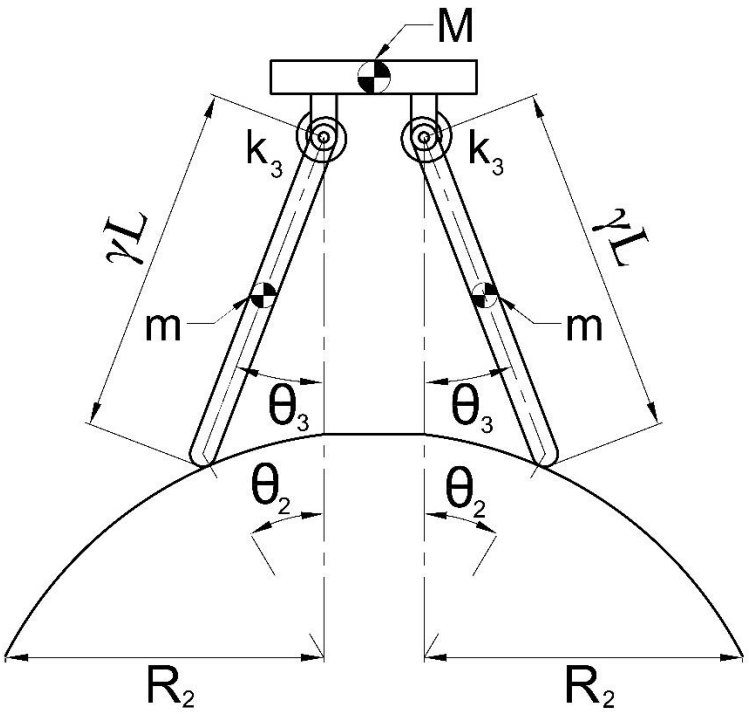

Figure 4.13. PRBM of Modular CFM

It is important to note that the center of curvature of the toroidal dome must lie in line with the center line of the compliant segments, and that from this center point, the radius is constant to the contact surface. The free body diagram is shown in Figure 4.14.

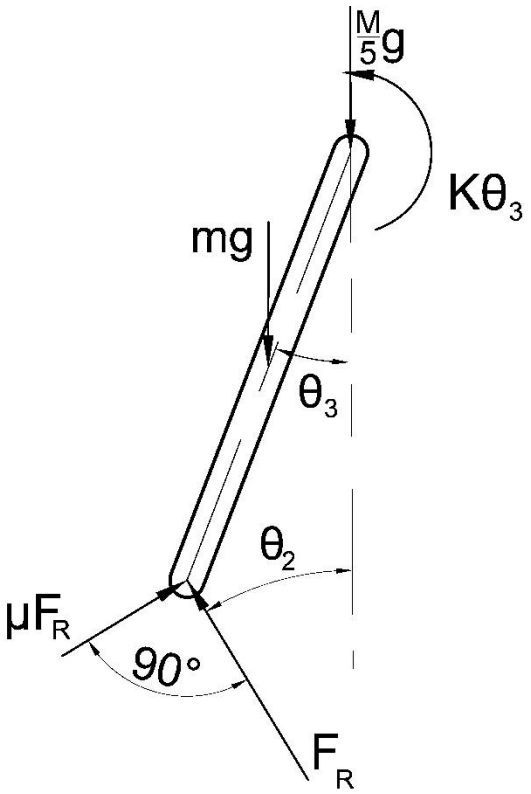

Figure 4.14. Free Body Diagram of Compliant Plunger

Where $\frac{M}{5}$ is the mass of the slider and is divided by the number of compliant segments, m is the mass of the compliant segment, and F_R is the reaction force from link 2 to link 3, and the friction force is assumed proportional to the normal force and acts perpendicular to the normal force. From the free body diagram an equation for F_R can be obtained, noting the mechanism under study has five compliant fingers. Summing the torques at the pin joint yields:

$$F_{R,comp} = \frac{5k_3\theta_3}{(\cos(\theta_2) - \mu\sin(\theta_2))\,\mathrm{r}_3\sin(\theta_3) + (\sin(\theta_2) + \mu\cos(\theta_2))\,\mathrm{r}_3\cos(\theta_3)} \qquad (39)$$

The above formulation applies for increasing θ_2, for decreasing θ_2 the equation for reaction force is given by:

$$F_{R,ext} = \frac{5k_3\theta_3}{(\cos(\theta_2) + \mu\sin(\theta_2))\,\mathrm{r}_3\sin(\theta_3) + (\sin(\theta_2) - \mu\cos(\theta_2))\,\mathrm{r}_3\cos(\theta_3)} \tag{40}$$

Now that the reaction for has been calculated, the non-conservative friction force can be taken into and the force output of the mechanism can be calculated using equation (39) for compression and (40) for extension.

$$F_{losses,comp} = F - \mu\sin(\theta_2)F_R + (M+m)g \tag{41}$$

$$F_{losses,ext} = F - \mu\sin(\theta_2)F_{R,ext} - (M+m)g \tag{42}$$

Where F is calculated from equation (28), $(M+m)g$ is the combined weight of the slider and compliant links, and μ is the coefficient of friction of the sliding contact. The force calculated in (28) should be at the halfway between the compression and extension forces. Equations (41) and (42) represent the net force from the compliant slider mechanism for compression and extension, respectively. A test case was run where the coefficient of friction was set to zero to ensure that the simulation was behaving as expected. Figure 4.15 shows the simulation for the coefficient of friction equal to zero.

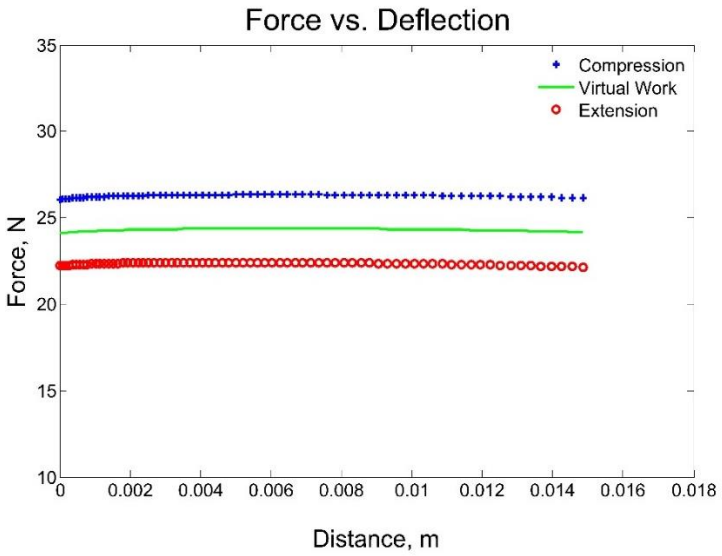

Figure 4.15. Simulation with no Friction Effects

Given the response of the simulation appeared appropriate, another test case for an arbitrary coefficient of friction of was ran. Figure 4.16 shows the response of the simulation for the coefficient of friction equal to .25.

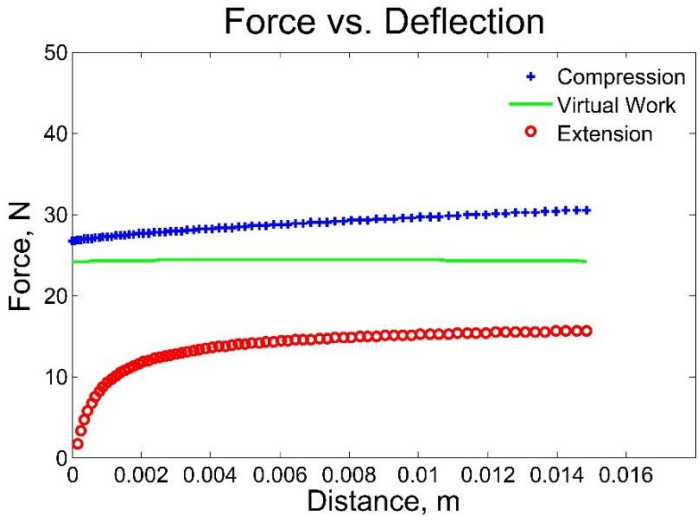

Figure 4.16. Simulation with Mass and Friction Effects

As seen the addition of the friction forces causes the response in extension and compression to drastically deviate from each other. The compression case tends to match closer to the force predicted in equation (28). As θ_2 tends to zero it is interesting to note the rapid slope change. However there is an indication that while the forces deviate in extension, there is still a large constant-force region that is still found in the extension case.

4.5 EXPERIMENTAL VALIDATIONS

The above equations give the response of a constant-force mechanism for one cycle of motion. Experimental validations were carried out by construction of a modular mechanism. The mechanism was tested on an ADMET universal testing machine. In order to reduce friction Teflon spheres inserted into the compliant plungers. All sliding surfaces were lubricated with lithium grease as well. Figure 4.17 shows the realization of the prototype mechanism constructed.

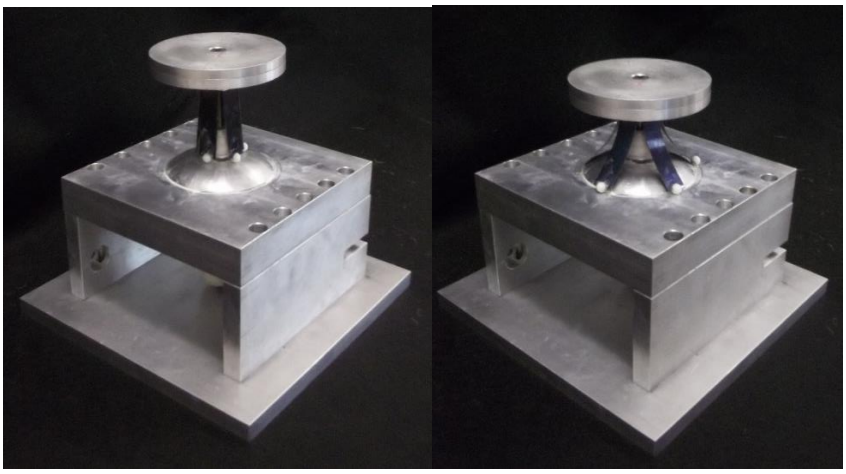

Figure 4.17. Physical Prototype Fully Extended and Fully Compressed

(a) (b)

The compliant plungers were constructed from 1074 scale less blue spring steel. The toroidal dome was precision machined on a CNC lathe, and the rest of the mechanism was fabricated by hand by experienced machinists. The spring steel plungers were .015”x.5”x2.15”. The mass of the slider was measured to be .255 kg. The length of the pseudo-link was 1.59”.

The test data was recorded by use of a force transducer and simultaneously recording the linear displacement of the transducer. The speed of the test was 15 mm/min, a value deemed suitable to neglect the acceleration and inertia effects of the mechanism. The force deflection plot of the mechanism is shown in Figure 4.18.

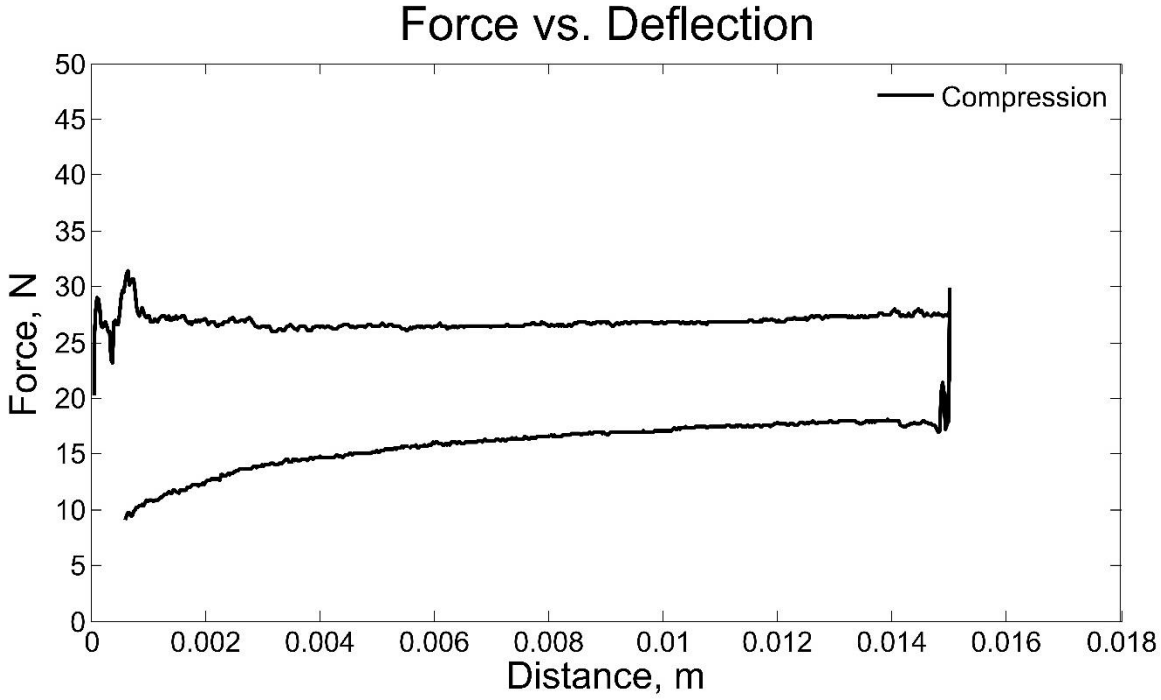

Figure 4.18. UTM Test Data

Taking the coefficient of friction of the sliding interface as .25 [65] and implementing the above formulations the response was predicted. Figure 4.19 shows the response of the mechanism using the friction and mass modeling, the principle of virtual work neglecting friction and mass effects, and the measured response.

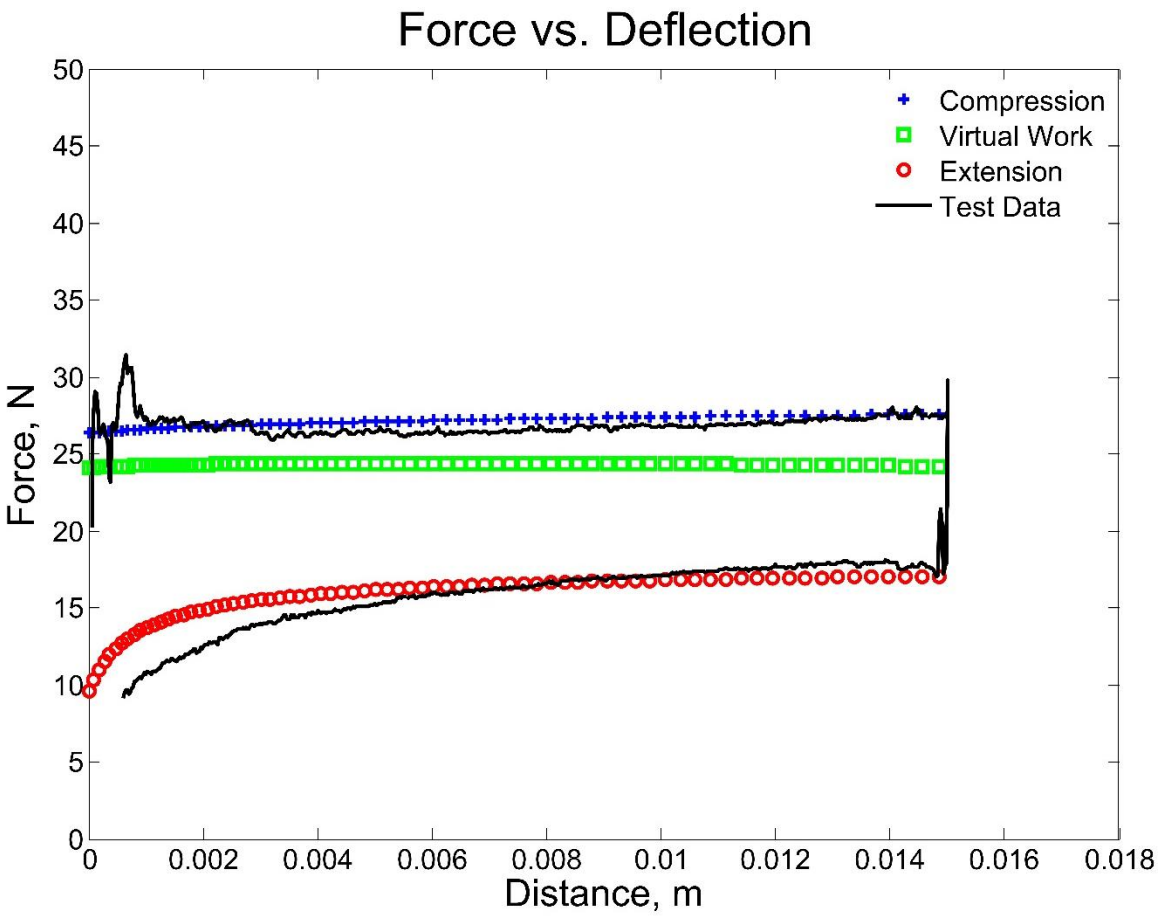

Figure 4.19. UTM Test Data and Modeled Response

The response in compression is measured approximately equal by either accounting or neglecting friction. The results obtained here in compression match those found in Karthik [56]. The beginning of the compression stroke shows an overshoot

response that is most likely either a buckling phenomenon or friction effects not accounted for. At the end of the of the compression stroke a large hysteretic drop is seen. The reason for this is attributed to the friction changing direction in conjunction with the force output of the mechanism changing directions, thus leading to the force due to the mass acting opposite of the measured force. The model predicts the trend of the response however discrepancies are seen in the amplitudes. While the above model does not predict the extension response with high precision, it does provide an easily implementable modeling technique as a first round approximation.

The compression stroke has a nearly linear increasing trend. The extension stroke however appears to have a nonlinear behavior. This again could be due to some buckling type phenomenon not accounted for. Manufacturing tolerances and defects could also play a role in this, however it is more likely some effect not accounted for is the main reason for the error terms for the extension cycle.

While preliminary modeling techniques were able to predict trends of the response, error in the amplitude is shown to be above acceptable limits. However this investigation does shed some light into the response shown in past research in the construction and validation of constant-force mechanisms. The integrals of the curves where calculated for both the compression and extension case, the compression error was found to be 10.54% and the extension error was found to be 8.92%. The larger error in the compression case is attributed to the buckling response seen at the beginning of the stroke.

5. DYNAMIC ANALYSIS OF CONSTANT-FORCE MECHANISMS

5.1 DYNAMIC RESPONSE OF COMPLIANT CONSTANT-FORCE MECHANISMS

Initially an investigation was undertaken to determine the plausibility of generating a square acceleration profile from a constant-force mechanism. Initial research was done into using existing rigid body solutions as generated by Jenuwine and Midha [35] Initial investigations proved promising as reported in Midha et al, [66]. The applications envisioned for such a mechanism were directed at impact testing for electronic equipment. However more far reaching applications were proposed such as shock absorption and energy management. Characterizing the characteristics of constant-force mechanisms will help ascertain the feasibility of these mechanisms in applications requiring energy management. This chapter will investigate the dynamic characteristics of compliant constant-force mechanisms. First a dynamic model will be presented. Modification of this model will then take place based on experimental static testing. Finally experimental results will be shown.

5.2 GENERAL DYNAMIC MODEL

Lagrangian techniques will again be used to model the general case for the compliant slider. First consider the system below undergoing planar motion shown in Figure 5.1.

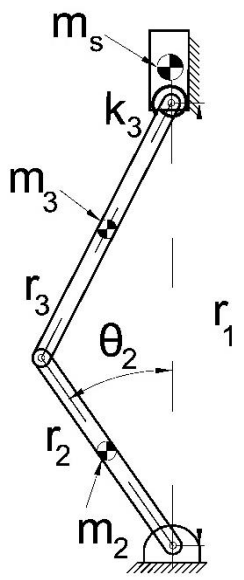

Figure 5.1. Dynamic Slider

Using loop closure equations the position and velocity of the slider can be found by the following equations:

$$r_2 \cos(\theta_2) + r_3 \cos(\theta_3) = r_1 \tag{43}$$

$$r_2 \sin(\theta_2) + r_3 \sin(\theta_3) = 0 \tag{44}$$

$$\theta_3 = -a\sin\left(\frac{r_2 \sin(\theta_2)}{r_3}\right) \tag{45}$$

$$\theta_{31} = a\sin\left(\frac{r_2 \sin(\theta_2)}{r_3}\right) \tag{46}$$

$$\dot{r}_1 = -r_2\dot{\theta}_2 \sin(\theta_2) + \frac{r_2^2 \sin(\theta_2)\cos(\theta_2)\dot{\theta}_2}{r_3\sqrt{1-\frac{r_2^2 \sin(\theta_2)^2}{r_3^2}}} \tag{47}$$

$$v_{r3} = -r_2\dot{\theta}_2 \sin(\theta_2) - \frac{1}{2} r_3\dot{\theta}_3 \sin(\theta_3) \tag{48}$$

Taking the gravitational datum when θ_2 is zero and assuming the system is perpendicular to gravity, and neglecting contributions from r_2, the kinetic and potential energies of the system can be written as shown below:

$$V = \frac{1}{2}(m_s\dot{r}_1^2 + J_3\dot{\theta}_{31}^2 + m_3 v_{r3}^2) \tag{49}$$

$$U = \frac{1}{2}k_3\theta_{31}^2 - m_3 g(r_2 \cos(\theta_2) + \frac{1}{2} r3\cos(\theta_3)) - m_s g r_1 \tag{50}$$

Where v_{r3} represents the velocity of the center of mass of link 3, m_3 represents the mass of link 3, r_3 is the length of link 3 based on the PRBM, k_3 is the PRBM stiffness, r_1 is the vertical distance from ground to the pin joint connecting r_3 and the slider, and m_s represents the mass of the slider.

It is important to note that the energy terms are nearly identical to those given in Boyle [48] however the polar moment of inertia term, *J*, has been modified to represent a link rotating at its end. Formulating the Lagrangian yields:

$$L = \frac{1}{2}(m_s\dot{r}_1^2 + J_3\dot{\theta}_{31}^2 + m_3 v_{r3}^2) - \frac{1}{2}k_3\theta_{31}^2 - m_3 g(r_2 \cos(\theta_2) + \frac{1}{2} r3\cos(\theta_3)) - m_s g r_1 \tag{51}$$

While taking the appropriate derivatives of the Lagrangian is possible, the ensuing derivations would be very cumbersome and so Maple's Euler-Lagrange function call was used to derive the equation of motion for the mechanism. The equation of motion for the mechanism is shown below as obtained from equation (11):

$$\frac{-J_3 r_2^4 \dot{\theta}^2 \theta}{r_3^4\left(1-\frac{r_2^2\theta^2}{r_3^2}\right)^2}-\frac{k_3 a \sin(\frac{r_2\theta}{r_3})r_2}{r_3\sqrt{\psi}}+m_s g(-r_2\sin(\theta)-\frac{r_2^2\sin(\theta)\cos(\theta)}{r3\sqrt{\psi}}$$

$$+mg(-r_2\sin(\theta)-\frac{r_2^2\sin(\theta)\cos(\theta)}{2r3\sqrt{\psi}})-m_s(-r_2\cos(\theta)\dot{\theta}^2 \tag{52}$$

$$-r_2\sin(\theta)\ddot{\theta}-\frac{r_2^4\sin(\theta)^2\cos(\theta)^2\dot{\theta}^2}{r_3^3\psi^{\frac{3}{2}}}-\frac{r_2^2\cos(\theta)^2\dot{\theta}^2}{r_3\sqrt{\psi}}$$

$$+\frac{r_2^2\sin(\theta)^2\dot{\theta}^2}{r_3\sqrt{\psi}}-\frac{r_2^2\sin(\theta)\cos(\theta)\ddot{\theta}}{r3\sqrt{\psi}})(-r2\sin(\theta)-\frac{r_2^2\sin(\theta)\cos(\theta)}{r_3\sqrt{\psi}})-\frac{J_3 r_2^2\ddot{\theta}}{r_3^2\psi}=F(t)$$

Where

$$\Psi=1-\frac{r_2^2\sin(\theta)^2}{r_3^2}$$

A simulation was conducted to verify the above derivation. The case of extension in the mechanism was considered. The mechanism was simulated to be fully compressed and then suddenly released, and the resulting acceleration profile was captured as shown in Figure 5.2.

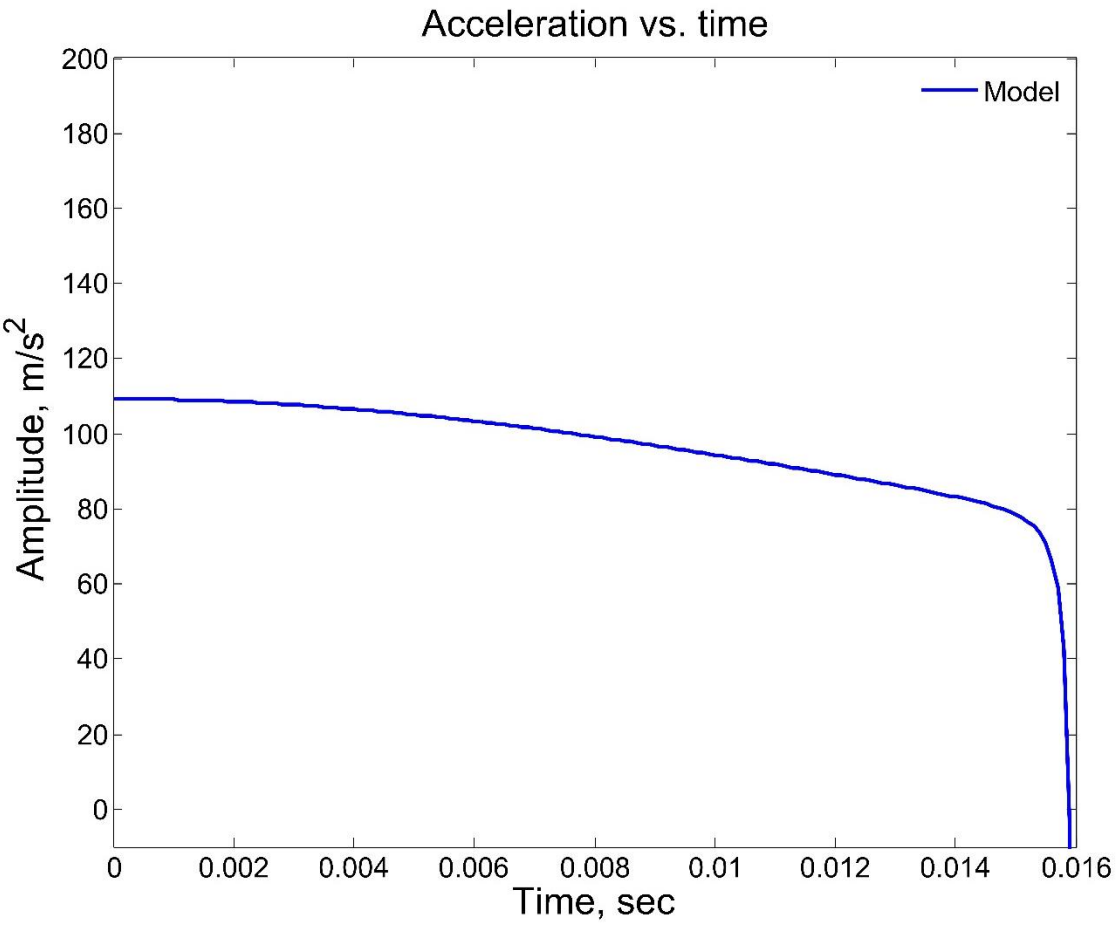

Figure 5.2. Ideal Dynamic Extension Stroke

5.3 MODIFICATION FOR THE EXTENSION CASE

From static testing the modular constant-force slider mechanism was shown to deviate from the predicted constant force values. Based on this it can be inferred that the potential energy of the mechanism deviates from the predicted expression in equation 50. This relationship was derived in Midha and Jenuwine [35]:

$$F = \frac{dE}{dr} \tag{53}$$

To properly model the mechanism based on the static response, either the potential energy can be obtained from the force deflection curve, or the static response can be treated as an external forcing function. The former of these two options was implemented. To calculate the potential energy the Force vs. θ_2 curve was fitted using a second order polynomial equation. The curve fit was then integrated with respect to θ_2 and the potential energy was known. Figure 5.3 shows the Force vs. θ_2 curve with the second order polynomial curve fit.

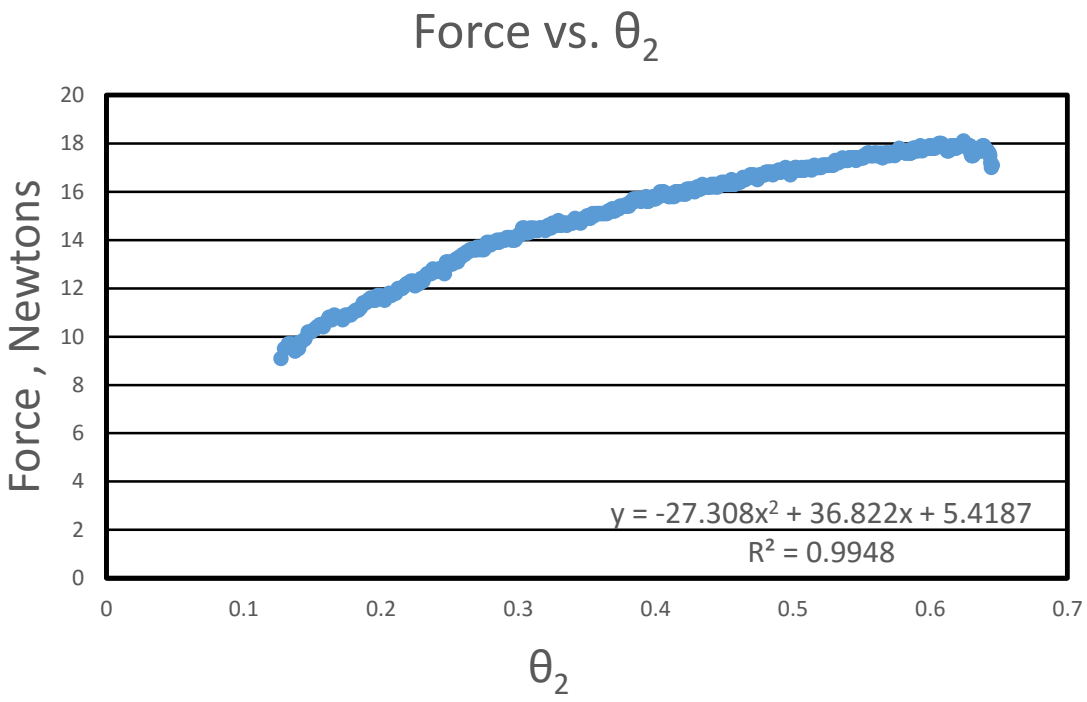

Figure 5.3. Force vs. θ_2 for Extension Stroke

The potential energy can now be expressed with terms including system losses and gravity terms as:

$$U = \frac{-27.308}{3} \cdot \theta^3 + \frac{36.822}{2} \cdot \theta^2 + 5.4187 \cdot \theta \tag{54}$$

This expression only applies to the extension case. The potential energy term can be viewed as a nonlinear spring and implementation of the term into the Lagrangian yields a nonlinear differential equation, however the solution of this equation is still possible by numerous numerical solver schemes, such as Runge-Katta 4-5th order solvers. The final equation of motion for the adjusted potential energy terms is shown in equation below:

$$\begin{aligned}
&-5.4187 + 27.308\theta_2^2 - 36.822\theta_2 - \frac{J_3 r_2^4 \dot{\theta}^2 \theta}{r_3^4 \psi} \\
&-m_s(-r_2\cos(\theta)\dot{\theta}^2 - r_2\sin(\theta)\ddot{\theta} \\
&-\frac{r_2^4 \sin(\theta)^2 \cos(\theta)^2 \dot{\theta}^2}{r_3^3 \psi^{\frac{3}{2}}} - \frac{r_2^2 \cos(\theta)^2 \dot{\theta}^2}{r_3\sqrt{\psi}} + \frac{r_2^2 \sin(\theta)^2 \dot{\theta}^2}{r_3\sqrt{\psi}} - \frac{r_2^2 \sin(\theta)\cos(\theta)\ddot{\theta}}{r3\sqrt{\psi}}) \\
&(-r2\sin(\theta) - \frac{r_2^2 \sin(\theta)\cos(\theta)}{r_3\sqrt{\psi}}) - \mathrm{m}_3(-r_2\cos(\theta)\dot{\theta}^2 - r_2\sin(\theta)\ddot{\theta} \\
&-\frac{r_2^4 \sin(\theta)^2 \cos(\theta)^2 \dot{\theta}^2}{2r_3^3 \psi^{\frac{3}{2}}} - \frac{r_2^2 \cos(\theta)^2 \dot{\theta}^2}{2r_3\sqrt{\psi}} + \frac{r_2^2 \sin(\theta)^2 \dot{\theta}^2}{2r_3\sqrt{\psi}} - \frac{r_2^2 \sin(\theta)\cos(\theta)\ddot{\theta}}{2r3\sqrt{\psi}}) \\
&(-r2\sin(\theta) - \frac{r_2^2 \sin(\theta)\cos(\theta)}{2r_3\sqrt{\psi}}) - \frac{J_3 r_2^2 \ddot{\theta}}{r_3^2 \psi} = 0
\end{aligned} \tag{55}$$

Where

$$\Psi = 1 - \frac{r_2^2 \sin(\theta)^2}{r_3^2}$$

It is important to note that the force deflection curve of the mechanism can be implemented directly into the equation of motion. By ignoring any potential energy terms in the Lagrangian, the polynomial curve fit would simply replace the right hand side of equation (52).

5.4 MODIFICATION FOR THE COMPRESSION CASE

While static testing showed much better prediction for the compression case modification to the equation of motion was implemented to ensure better results. Furthermore, the testing procedures for the compression case would dictate changes to the equation of motion. First consider the system below, a mass falling onto a spring bed as shown in Figure 5.4.

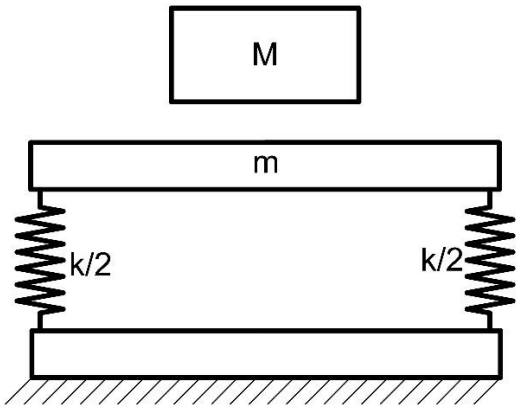

Figure 5.4. Mass Spring Bed System

After impact, assuming the mass *M* follows the platen mass *m*, the kinetic and potential energies of the spring bed platen can be expressed by equations below. In this case k represents the nonlinear spring rate of the constant-force mechanism. It is

important to note that the masses used in the equations below are not correlated with the masses in equations (41) and (42). The term m, represents the combined mass of the slider and the compliant links.

$$T = \frac{1}{2}(M + m)\dot{x}^2 \tag{56}$$

$$U = \frac{1}{2}kx^2 + (M + m)gx \tag{57}$$

To obtain the initial conditions of the system the Conservation of Momentum needs to be implemented to compare the initial and final velocities about the impact of the falling mass striking the platen. The following equation demonstrates how to obtain the velocity of the platen after impact:

$$\frac{Mv_i^2}{(\mathrm{M}+\mathrm{m})\,\mathrm{v}_o^2} = e \tag{58}$$

By using any standard kinematic equation to determine the initial velocity of the impact, v_i, and assuming a coefficient of restitution, one can determine the initial velocity, v_0, to the equation of motion. The forcing function of this system is no longer zero, and is given below for the impact:

$$F = Mv_0\delta(t) \tag{59}$$

Where $\delta(t)$ represents the Dirac Delta function. As with the extension case, the potential energy term needs to be adjusted to mimic the static deflection of the mechanism. Following the same procedure in the previous section, the Force vs. θ_2 plot can be seen in Figure 5.5.

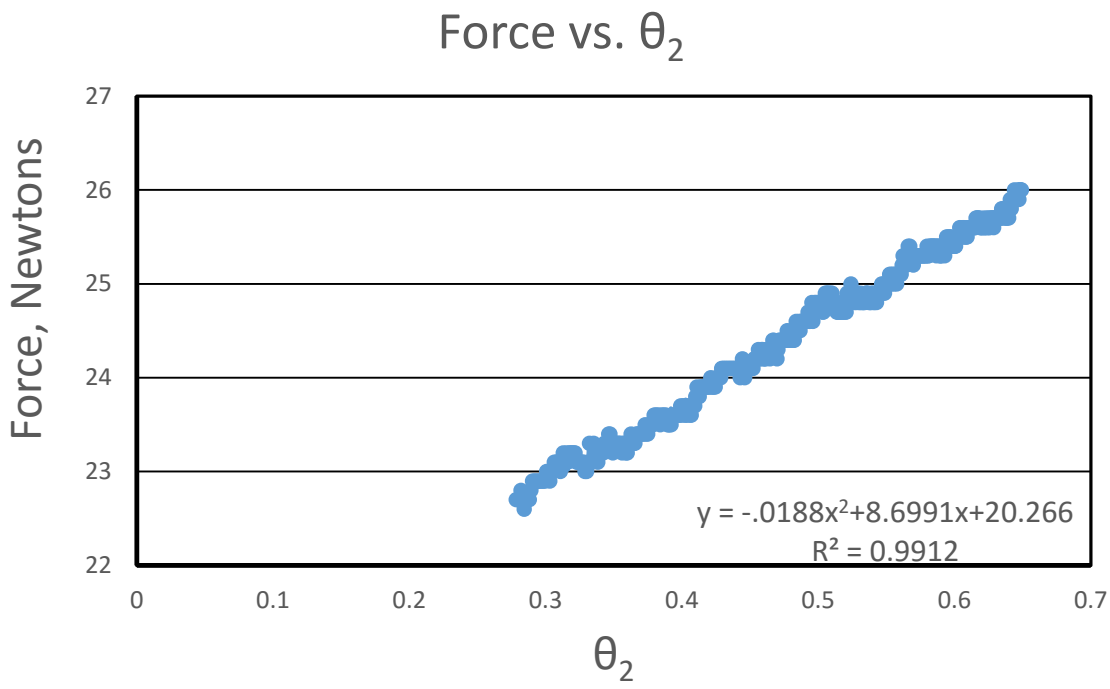

Figure 5.5. Force vs. θ_2 for Compression Stroke

Implementing the curve fit the potential energy of the system can now be expressed as:

$$U = \frac{-.0188}{3} \cdot \theta_2^3 + \frac{8.6991}{2} \cdot \theta_2^2 + 20.266 \cdot \theta_2 \tag{60}$$

Where gravity and friction effects are accounted for in this expression. Thus the final equation of motion is expressed as:

$$-20.266 + .0188\theta_2^2 - 8.6991\theta_2 - \frac{J_3 r_2^4 \dot{\theta}^2 \theta}{r_3^4 \psi}$$

$$-m_s(-r_2\cos(\theta)\dot{\theta}^2 - r_2\sin(\theta)\ddot{\theta}$$

$$-\frac{r_2^4\sin(\theta)^2\cos(\theta)^2\dot{\theta}^2}{r_3^3\psi^{\frac{3}{2}}} - \frac{r_2^2\cos(\theta)^2\dot{\theta}^2}{r_3\sqrt{\psi}} + \frac{r_2^2\sin(\theta)^2\dot{\theta}^2}{r_3\sqrt{\psi}} - \frac{r_2^2\sin(\theta)\cos(\theta)\ddot{\theta}}{r3\sqrt{\psi}})$$

$$(-r2\sin(\theta) - \frac{r_2^2\sin(\theta)\cos(\theta)}{r_3\sqrt{\psi}}) - \mathrm{m}_3(-r_2\cos(\theta)\dot{\theta}^2 - r_2\sin(\theta)\ddot{\theta}$$

$$-\frac{r_2^4\sin(\theta)^2\cos(\theta)^2\dot{\theta}^2}{2r_3^3\psi^{\frac{3}{2}}} - \frac{r_2^2\cos(\theta)^2\dot{\theta}^2}{2r_3\sqrt{\psi}} + \frac{r_2^2\sin(\theta)^2\dot{\theta}^2}{2r_3\sqrt{\psi}} - \frac{r_2^2\sin(\theta)\cos(\theta)\ddot{\theta}}{2r3\sqrt{\psi}})$$

$$(-r2\sin(\theta) - \frac{r_2^2\sin(\theta)\cos(\theta)}{2r_3\sqrt{\psi}}) - \frac{J_3 r_2^2\ddot{\theta}}{r_3^2\psi} = Mv_0\delta(t) \tag{61}$$

Where

$$\Psi = 1 - \frac{r_2^2\sin(\theta)^2}{r_3^2}$$

While the modification of the potential energy may be viewed by some as forcing the model to fit, it is important to note Table 3.1 that showed very high accuracy of the prediction of strain energy with that of ANSYS®. The power of the PRBM to predict the potential energy of single segments has been proven already, and the discrepancies are again most likely a cause of the construction of the mechanism with effects not considered in the modeling.

5.5 EXPERIMENTAL SETUP

With both cases of mechanism travel modeled, experimental validations were conducted to test the validity of the predictions. First, a brief outline of the equipment used and testing procedures will be outlined.

For any dynamic experiment a proper data acquisition system is necessary. Ease of use, practicality of implementation, sample rate, and availability often dictate which systems will be used. The all dynamic testing done in this work the National Instruments 9234 C-DAQ series was used. The 9234 has four BNC inputs, offers in-built hardware anti-aliasing filtering and IEPE excitation for piezo electric sensors. The maximum sample rate of this system is 51.2 kHz [67] . National Instruments also provides several software integration features to facilitate data collection that require no user programming. The package of choice was National Instruments Signal Express (SE). SE offers flexibility in experimental setup, filtering, and frequency analysis. Data collected from SE was exported as either filtered or unfiltered and imported into Matlab.

Sensor choices should be done so that the sensor is capable of capturing the frequency range of interest and minimal impact on the system under test. The Kistler 8614A5 was chosen due to its small weight and high frequency range. Beeswax was used to attach the accelerometer to the devices under test. Low noise BNC cables were used to minimize or eliminate unwanted electrical noise. All experiments were conducted on large vibration isolating tables to reduce external environmental effects such as building vibrations.

5.6 EXPERIMENTAL VALIDATION EXTENSION CASE

For the case of extension the sensor was placed at the centerline of the mechanism in order to reduce any effects due to force imbalances. The mechanism was compressed and held in place with a dowel pin acting as a release mechanism. The change of height relative to the foundation on which the mechanism rested was measured, and from this initial conditions for the differential equation were calculated. Masses such as the mass of the slider were measured using a digital scale and the values implemented into the differential equation. The simulation was conducted using Matlab and invoking the ODE45 function call. ODE45 is a 4-5th order Runge-Katta solution method for general differential equations. The solution to the differential equation yielded displacement and velocity as a function of time. These values were the substituted back into the original differential equation to determine the acceleration profile of the mechanism. Below is a plot of the experimental data for the extension case. This data was filtered using an 8 pole Butterworth low-pass filter with a cutoff frequency of 5000 Hertz. The sample rate was 51.2 kHertz.

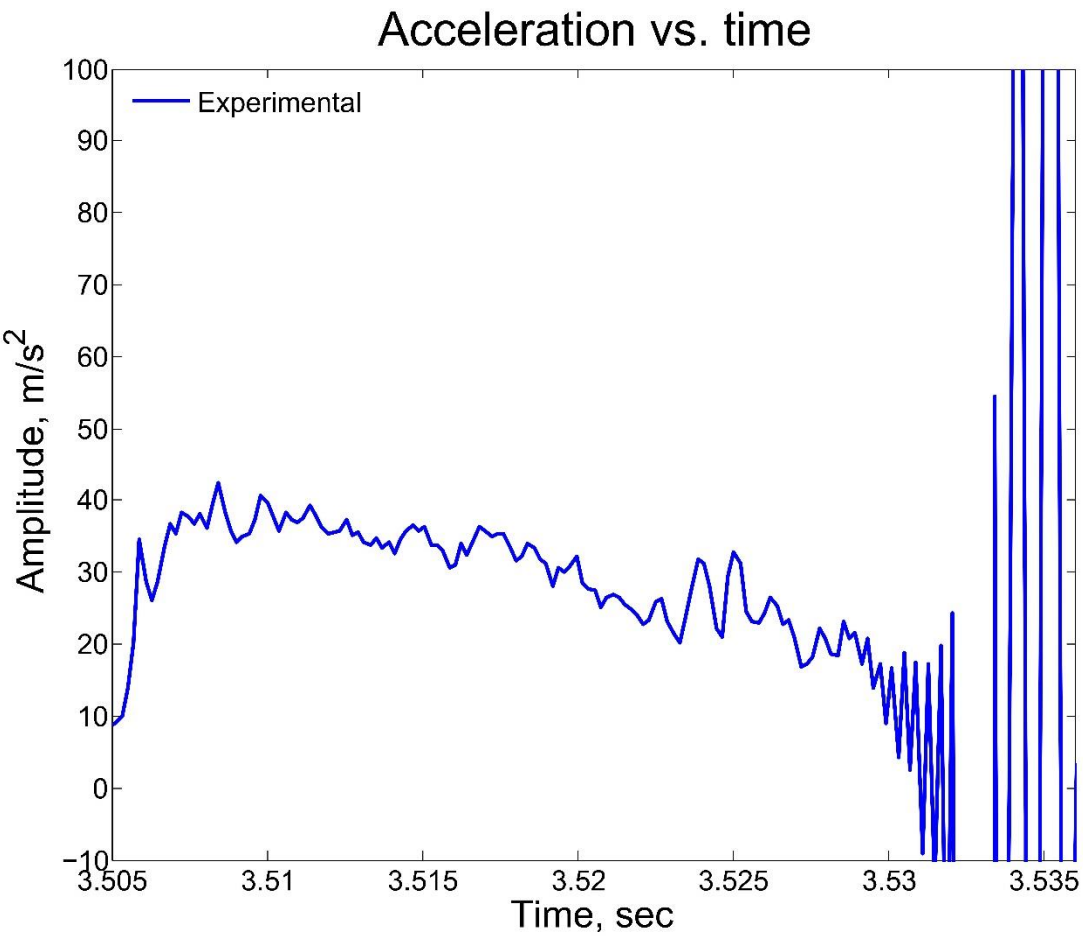

Figure 5.6. Measured Acceleration Signal for Extension Stroke

The behavior is as expected. From the static testing the force is higher at the beginning of the extension stroke and reduces in amplitude as the mechanism reaches its equilibrium position. The time duration of the stroke is very important to note. If the energies of the system can be captured correctly, the time duration of the physical mechanism and the simulations should match. Under the modifications of the dynamic model, the potential energy terms have been adjusted and should reflect the physical system under test with high fidelity. Therefore, and discrepancies in the time duration would come from errors in predicting the kinetic energy of the system. Oscillations

noticed in the experimental results can be attributed to small imperfections of the machined toroidal dome and external vibrations not isolated by the base. As the mechanism reaches its equilibrium point, the response of the mechanism may excite itself into other modes of vibrations not accounted for in the modeling. Vibrations after the mechanism has reached its equilibrium position are due to the collision of a physical stop implemented on the main shaft. This was done to prevent the mechanism from separating. Lastly, a slight rise time at the onset of the data can be seen. This has been attributed to small friction and any cocking of the mechanism as the pin is pulled that has not been accounted for the in the model. Figure 5.7 shows the overlay of the predicted acceleration profile and the measured response.

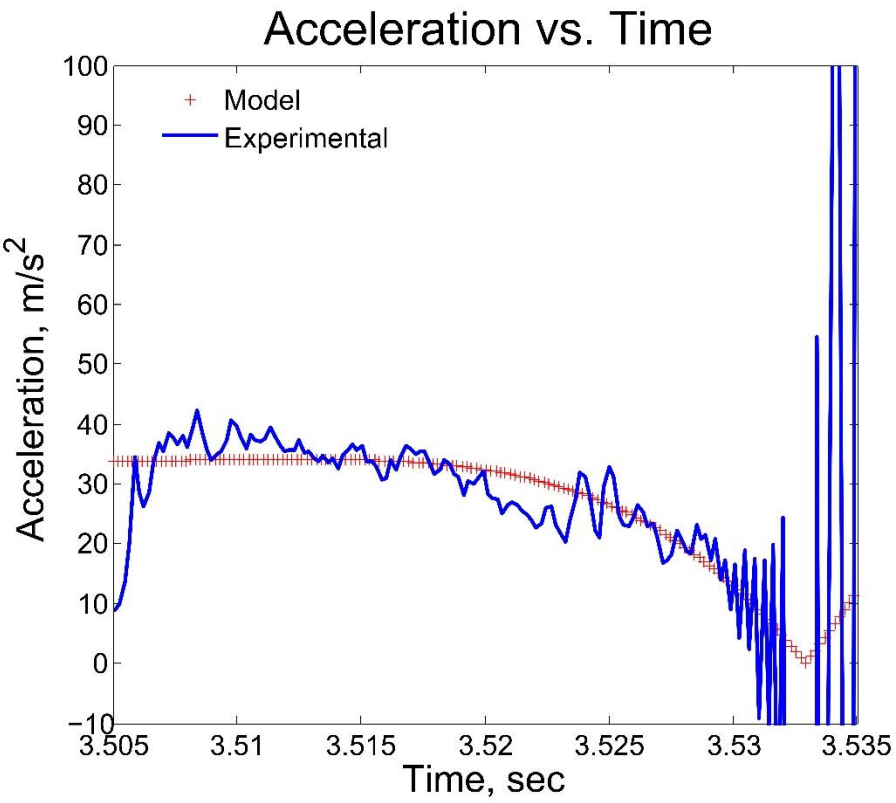

Figure 5.7. Measured and Predicted Acceleration for Extension Stroke

As seen the predicted values closely resemble the shape and duration of the measured pules. Oscillations at the end of the stroke appear to be nearly symmetric about the predicted values. Issues such as rise time to nominal acceleration, the ramp effect at the beginning of the stroke, are not accounted for. The predicted value very nearly accounts for the entire area under the measured values. While some areas are slightly higher in the measured response, others are slightly under. Integrating the area under both signals reveals insights about the energy absorption characteristics of the mechanism. The integration was done for two conditions, once over the entire range of motion, and once neglecting the rise time at the beginning of the response. If the rise

time phenomenon can be explained, implementation of this into the model can be done and will perhaps lead to better correlation. Taking the integration of both signals over the time duration of the stroke shows extremely good correlation. It is important to note that the integration of the curve represents the impulse of the mechanism. Computing the percent difference of the integrals gives a percent error of 3.4525%. Extremely promising results for a simple single degree of freedom model. Applying the unmodified model yields an error of nearly 50%, showing the impetus to have carefully constructed mechanisms. Furthermore, the large error from the theoretical model points to the fact that more insight is needed into the physical mechanisms for the errors in the static cases.

The model predicts the area under the measured acceleration curve very closely. Proper prediction of the acceleration profile for constant-force mechanisms will prove to greatly lend a hand in the analysis of the energy absorption characteristics.

5.7 EXPERIMENTAL VALIDATION COMPRESSION CASE

For the compression case a slightly different approach was taken than that in Boyle [48]. In previous work an actuator was used to give a displacement boundary condition to the mechanism and the response and force input was measured. However the response of the mechanism will be highly dependent on the input displacement conditions, and in fact the dynamic response could be dominated by this. To try to overcome these issues an impact test was implemented in the case of dynamic compression testing. A cylindrical mass of aluminum was dropped from a known position and the response of the slider was measured. Some liberal assumptions were made as to the impact portion such as all momentum of the impacting mass is transferred to the slider and that the impact was perfectly elastic. While these assumptions are most

likely not prefectly true, they provide a starting point for determining the systems response.

For this testing a mass of 1.18 Kg was dropped from a distance of 4 inches. The accelerometer was attached to bottom of the platen. Initially the data was filtered again at 5000 Hz with the Butterworth filter from the extension testing. A plot of the filtered data is below.

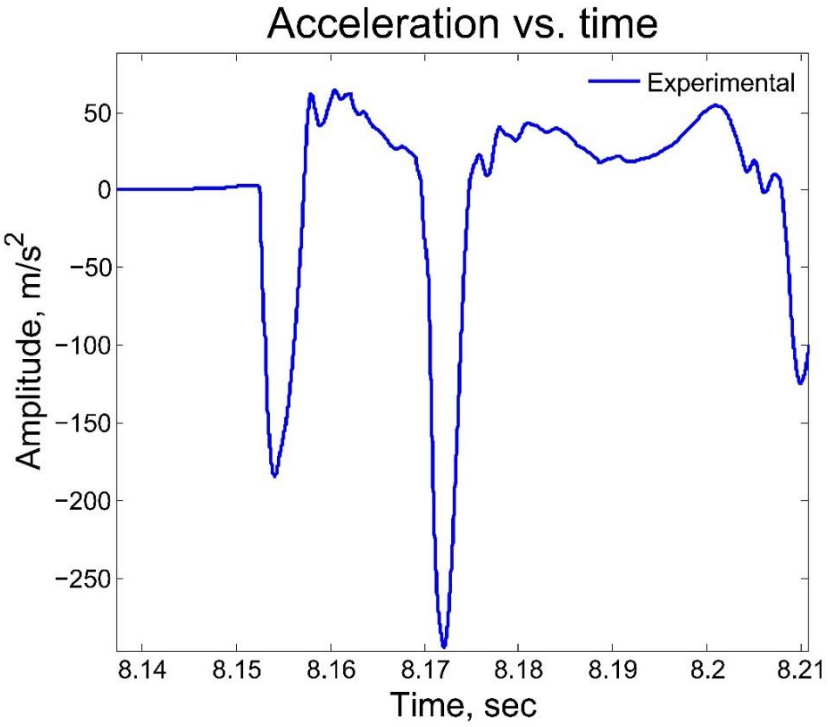

Figure 5.8. Multiple Cycles from Compression Test

As seen, the mechanism undergoes a sharp acceleration downward to the end of the stroke, and then the extension portion becomes evident by the rebound witnessed.

This cycle continues at least two noticeable times before vibration in the mechanism becomes more than the rigid-body response. The response is composed of two regimes, the compression and the extension stroke. The full cycle from one maximum compression displacement to another represents the full cyclic response of the mechanism. Also of note is thedeviation on the decreasing portion of the compression stroke. This is most likely due to external vibrations. To emphasize the nature of this portion of the stroke, all that is of concern is the initial deceleration portion of the first curve. After that the model will diverge due to the potential energies not being correct. As mentioned above the liberal assumption of the coefficient of restitution equal to 1 yielded unreasonable results. The initial condition was iterated upon to determine a suitable coefficient of restitution. The modeling shown uses a coefficient of restitution of 0.4.

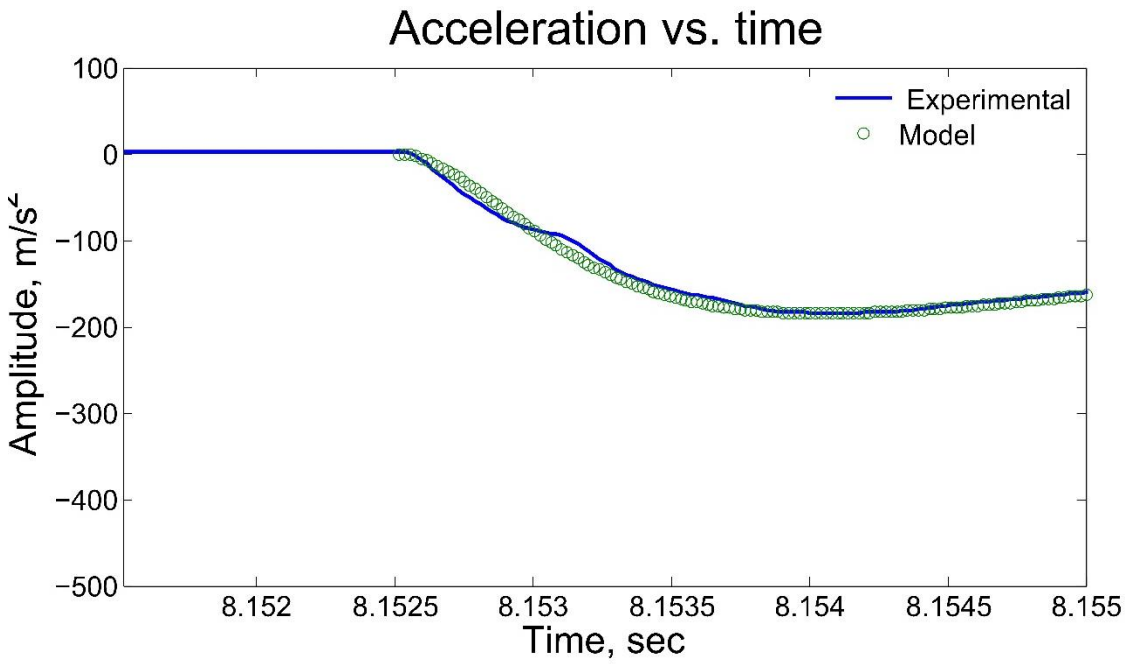

Figure 5.9. Measured and Predicted Acceleration for Compression Test

The simulation results are shown along with the first compression cycle of the experimental results. The correlation appears to be very good at first sight. The magnitude of the maximum acceleration is predicted adequately, along with the time to reach the maximum. Calculating the integrals under the curve from the initial deceleration to the minimum yields a percent error of 1.1309%. While the results look extremely promising more analysis and thought needs to be given on the assumptions made in the modeling.

6. CONCLUSIONS AND FUTURE WORK

6.1 FUTURE WORK AND CONCLUSIONS

The validity of the PRBM for dynamic transient modeling has been established. Several approaches to account for the kinetic energy with a "characteristic mass" have been presented. Each model provides reasonable accuracy when compared with experimental results. Furthermore, approaches to modeling the transient response of flexible segmentsm with nonlinear damping representation, utilizing a two stage damping ratio determination have been developed. This approach should be investigated for further damping stages and validated with forced vibration tests. Furthermore, applications of the 2R and 3R PRBM may be implemented to allow for higher accuracy, including more modes of vibration modeled using the PRBM. From the modeling presented the PRBM predicts the potential energy of a large-deflection cantilever beam extremely well, and given the high precision with which the natural frequencies are predicted, the PRBM predicts the kinetic energy of these segments by way of defining the "characteristic mass." Further work should be done with other segment types such as the SLFP and fixed-guided segments.

The work pertaining to single segments was extend to simple mechanisms e.g. a parallel guiding mechanism. The dynamic model based on the PRBM was able to capture the natural frequency content and the decay of the free vibration resonse of this mechanism.

The static response of constant-force slider mechanisms was also investigated. Throughout the literature review, numerous works have been presented on the

mechanisms that generate constant force, however, analytical insights as to their deviation from expected results were never given. This work is the first to attempt to explain discrepancies in the measured and predicted values of the constant force generated by the slider mechanisms. While the expansion stroke predictions have a larger error associated with them, the compression strokes have far better accuracy, and trends in this and previous works can now be explained with clarity. Further investigation into the buckling phenomenon and friction effects should be conducted.

An important objective of this thesis was to generate a rectangular impulsive acceleration profile. The main premise and hope was that constant force would yield constant acceleration. With the construction of the selected configuration, however, this was not exactly possible due to manufacturing difficulties and friction effects. However, a dynamic model analyzing the acceleration of the constant-force slider mechanism was presented and validated, for both compression and extension cases. Further testing should be done in both cases for forced vibration analysis. Fully understanding the dynamic characteristics of the mechanisms will help with practical application matching for these devices. Currently, it is recommended that the devices be investigated for applications in:mpact Testing

1.) Packaging Protection
2.) Fall Protection
3.) Vehicle Crash Protection

As greater understanding of these mechanisms is developed, so will be their applications. Finally, it is suggested that a careful study of their manufacturing be considered, so that the effects of manufacturing tolerances and friction may be

minimized. As manufacturing methods advance and materials sciences develop stronger and more resilient materials, it would be very possible to generate large constant-force loads for applications on a very large scale. This work provides a fundamental basis for the dynamic analysis of such mechanisms while benefiting from the true spirit of the PRBM, i.e., in its ease of implementation of the modeling presented.

APPENDIX A

ENGINEERING DRAWINGS

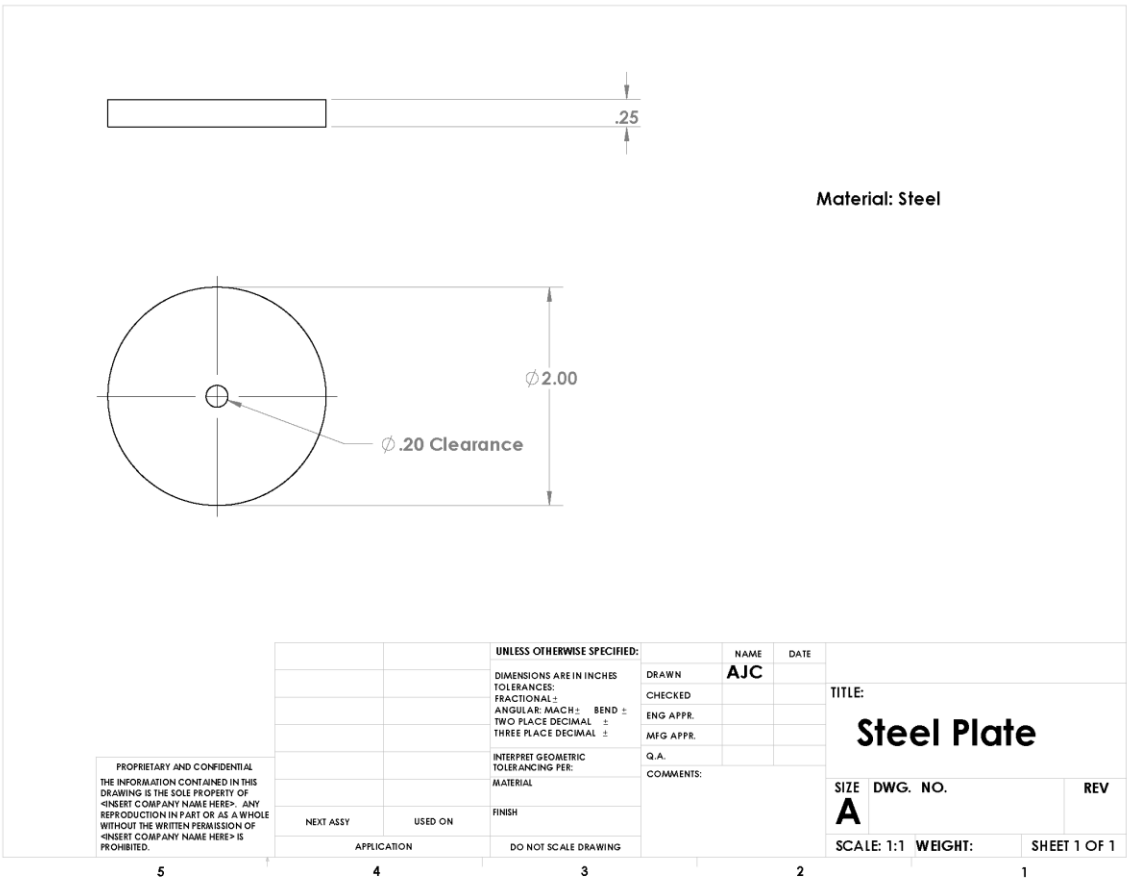

Figure A.1. Steel Plate

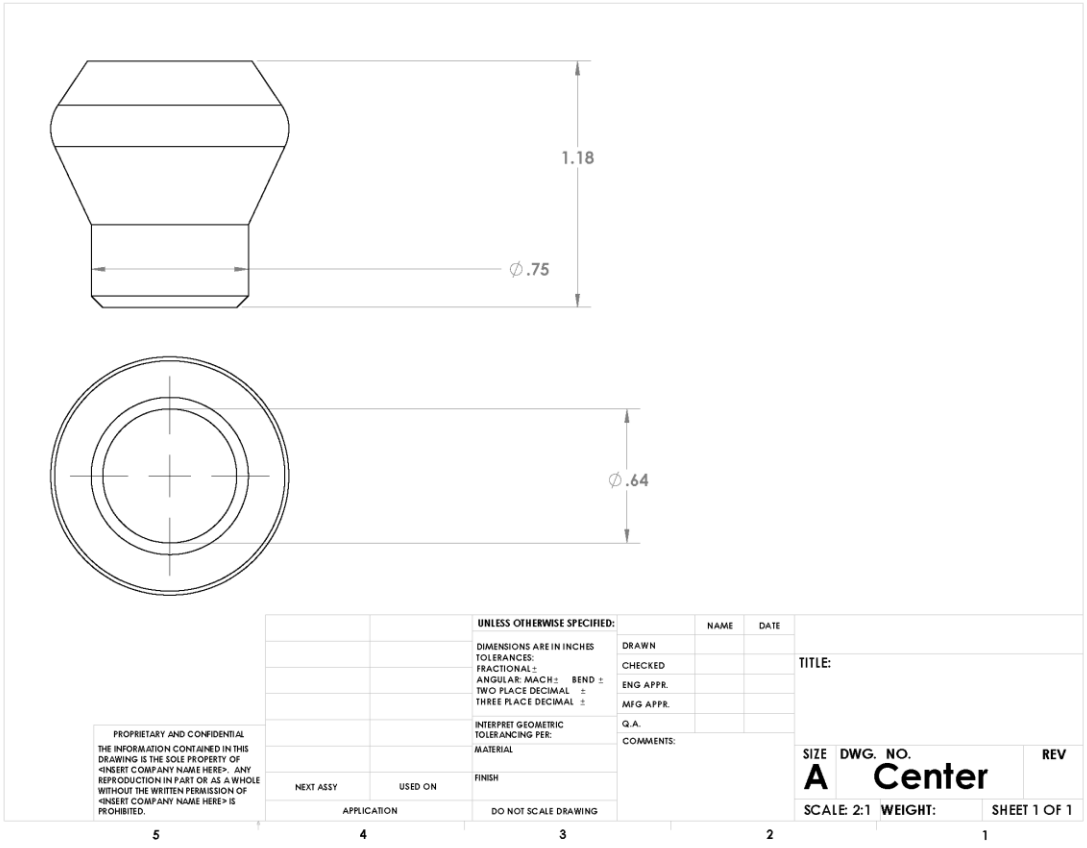

Figure A.2. Deflector

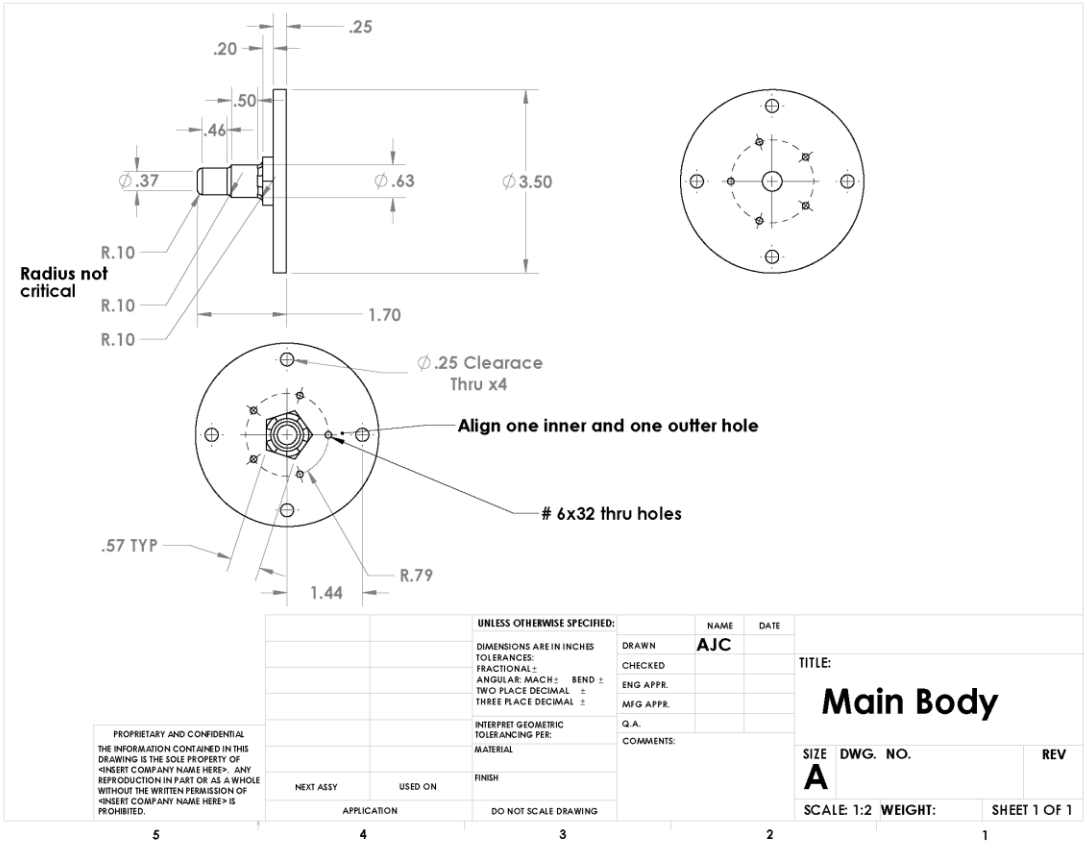

Figure A.3. Base of Modular Device

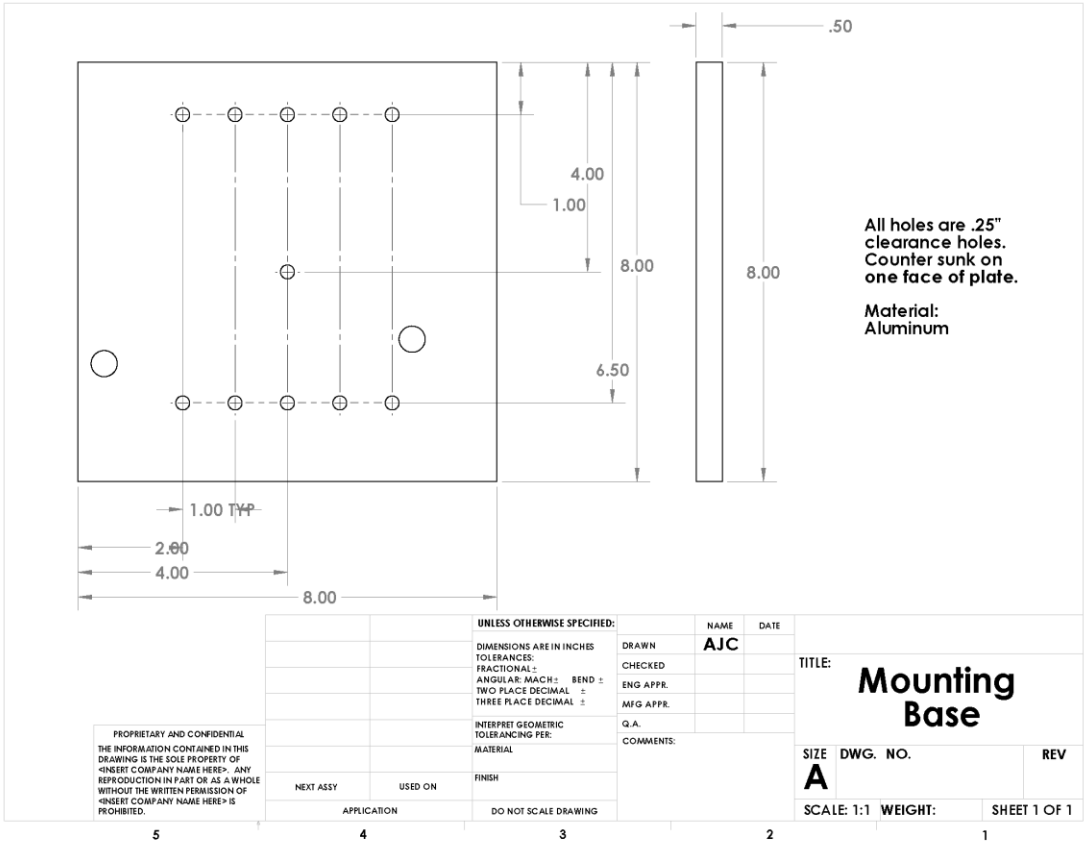

Figure A.4. Mounting Base

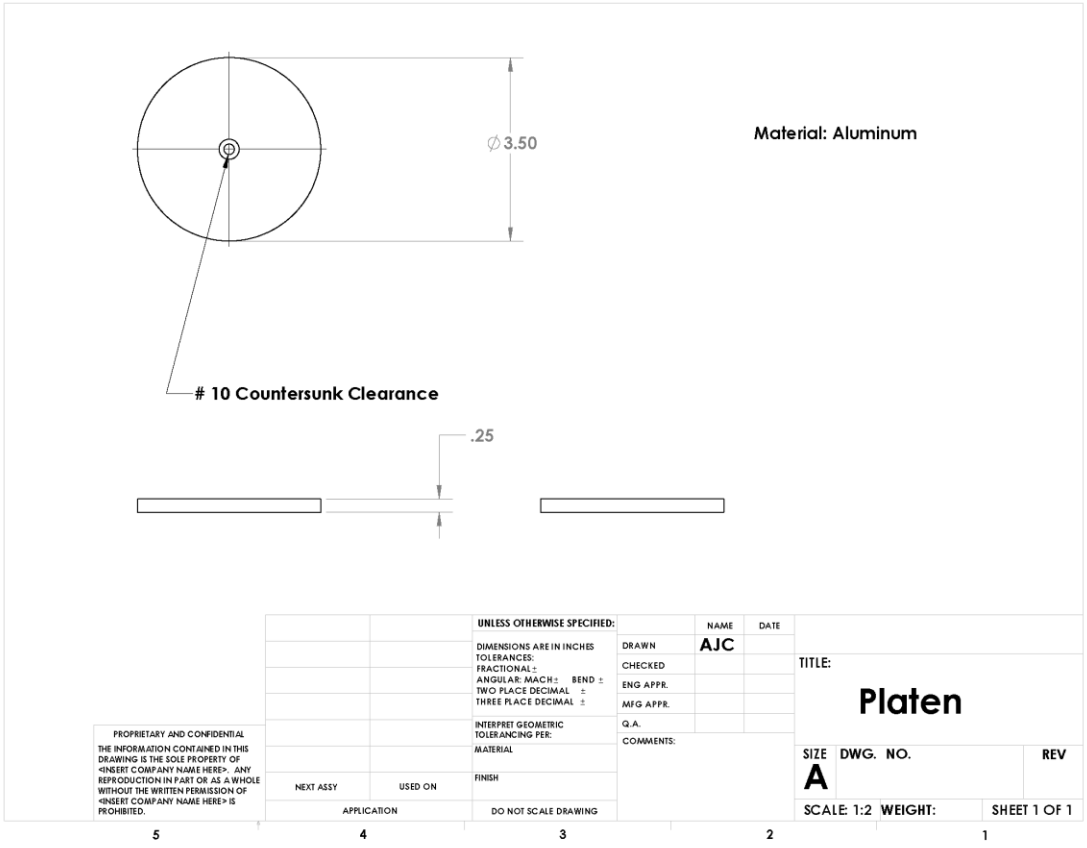

Figure A.5. Platen

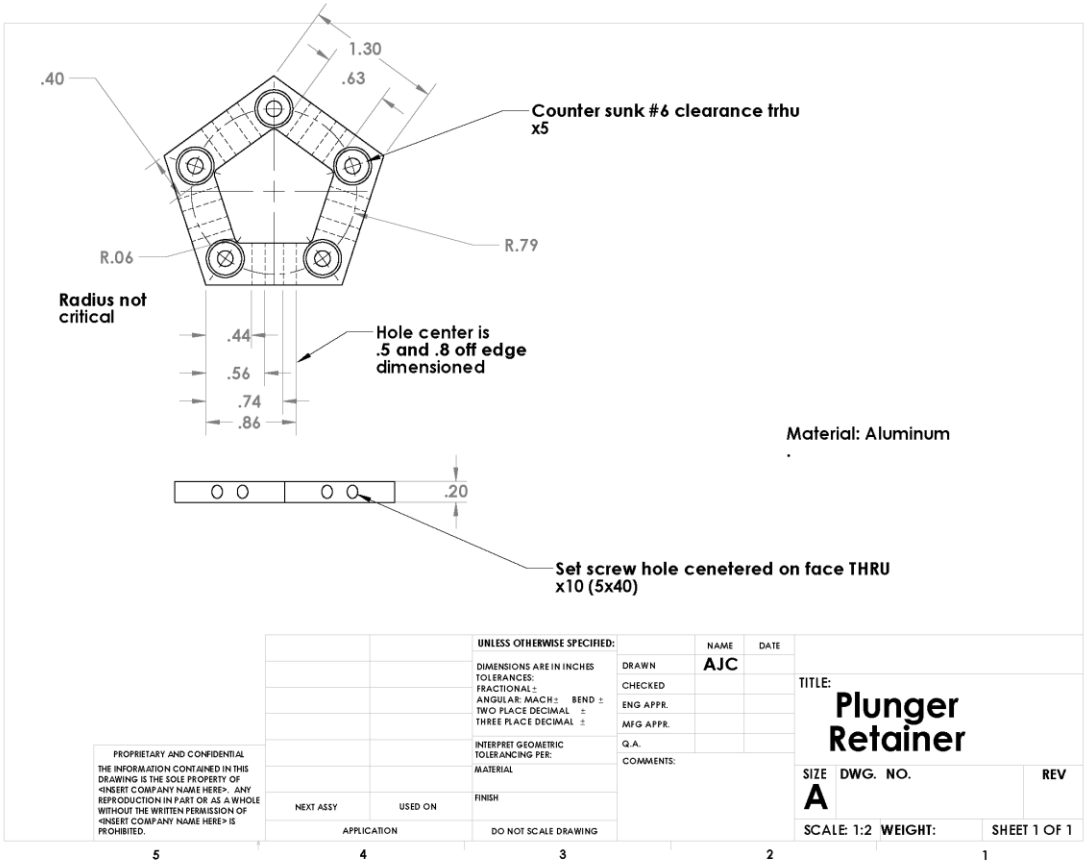

Figure A.6. Retainer

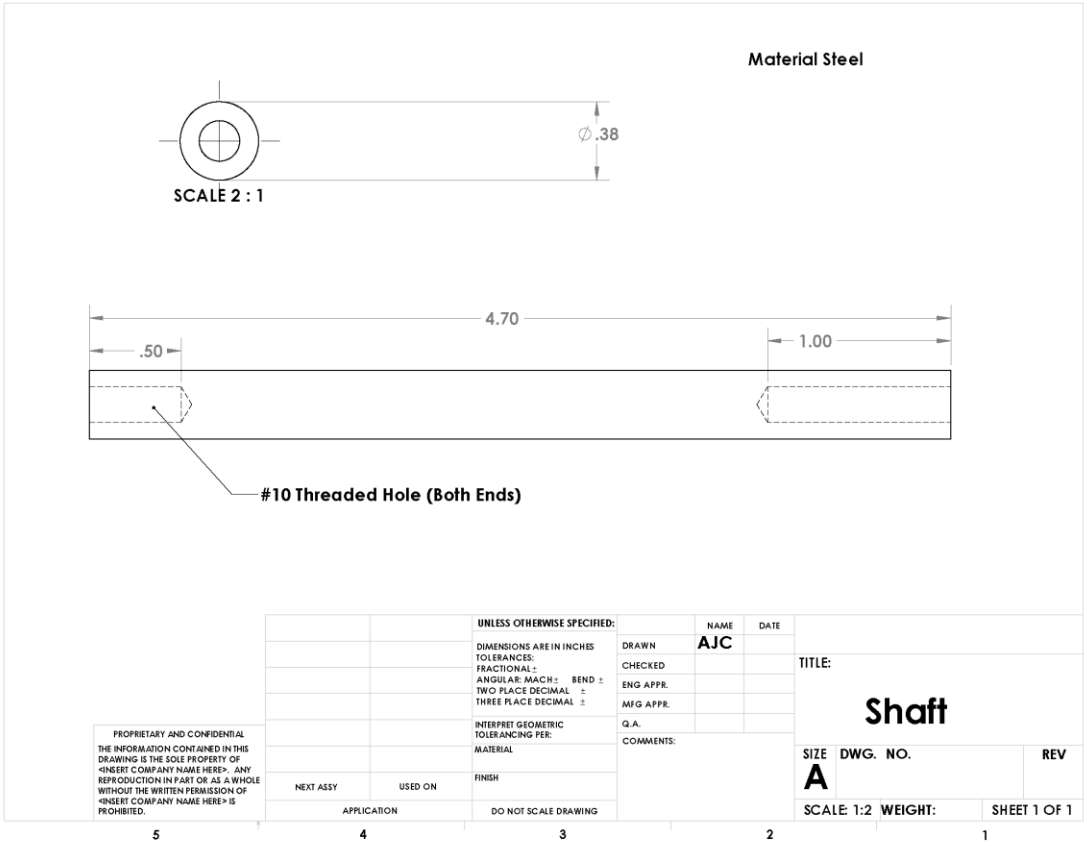

Figure A.7. Main Bearing Shaft

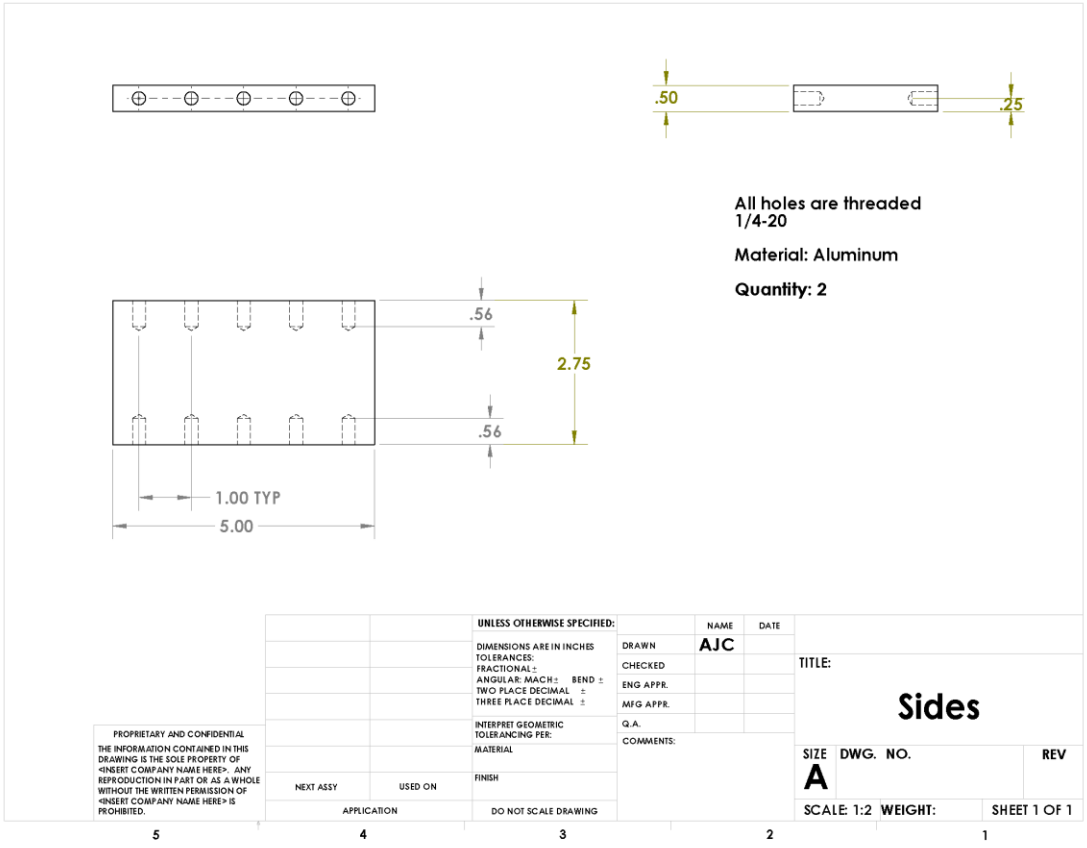

Figure A.8. Mounting Sides

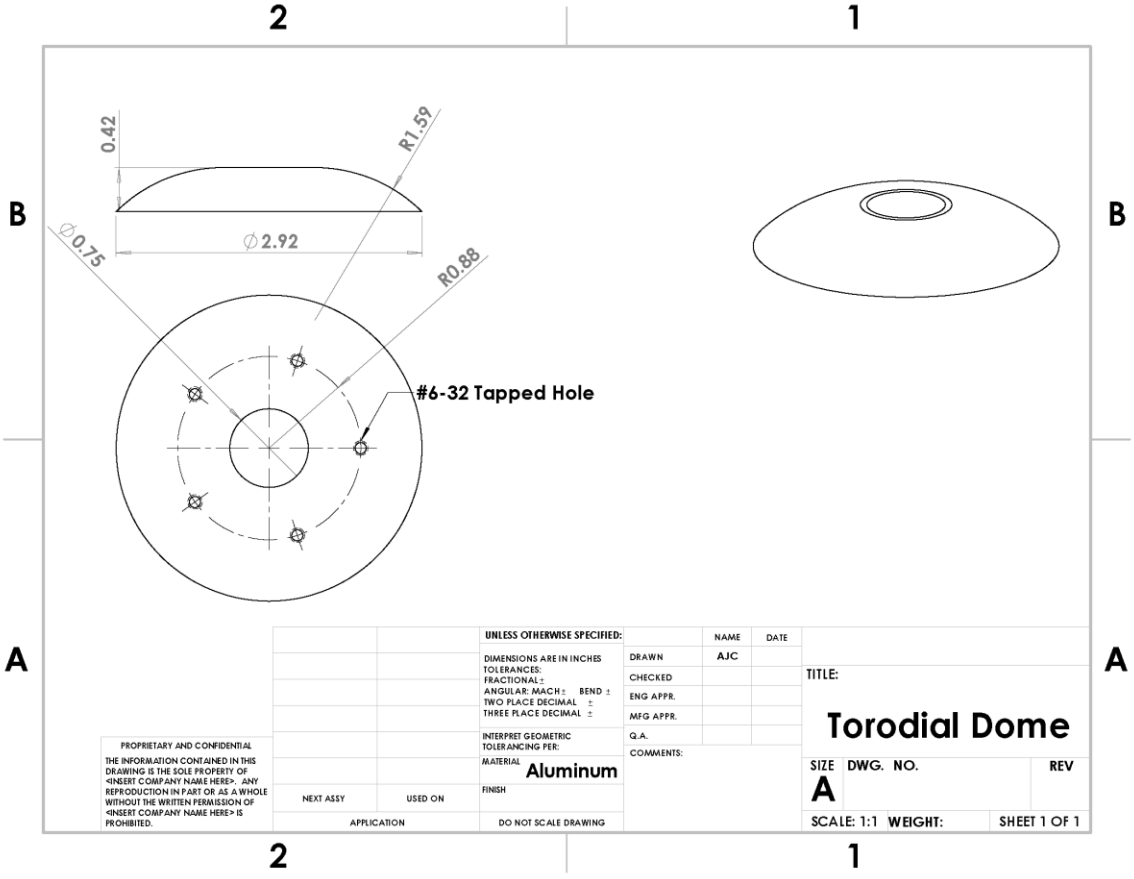

Figure A.9. Toroidal Dome

APPENDIX B

STATIC CFM MATLAB® CODE

```
%Class 1a

clc;
clear all;
format longe;
phi = 0.4773;
R = 0.8853;
gama=0.89; %Gamma
Kt=2.65; %K theta
L=2.2*.0254; %Length of beam
r3=gama*L;
r2=1.59*.0254; %R2
k2=0;  %Spring 2
k1=0;  %Spring 1
E=210e9; % Young's Modulus
h11 = 0.01526*.0254; %Thickness of compliant beam
w=0.5*.0254; %Width of compliant beam
I=w*h11^3/12;  %moment of interia
g=0;
h = 2*pi;
k3=gama*Kt*E*I/L;  %spring 3
u=.025  %coefficient of friciton in compression
n=1;
max1=18/1000 %max displacement
theta2=linspace(10*pi/180 ,pi/4.6, 75) %theta 2 values
r4=.04*.0254 %offset
for n=1:numel(theta2)
    %calulate kinematic values
    theta3(n) = asin((-r2*sin(theta2(n))-r4)/(r3));
    theta311(n) = (asin(r2*sin(theta2(n))-r4)/r3);
    theta311c(n)=theta311(n);
    theta31(n)=(2*pi+theta3(n));
    r1(n)=r2*cos(theta2(n))+r3*cos(theta3(n));
    %end kinematics
    %start forces
    Ff(n)=5*k3*theta311(n)/((((cos(theta2(n))-u*sin(theta2(n)))...
        *gama*L*sin(theta311(n))))+(sin(theta2(n))...
    +u*cos(theta2(n)))*gama*L*cos(theta311(n))); %reaction force
    Ffy(n)=Ff(n)*u*sin(theta2(n)); %friction force y
    Ffx(n)=Ff(n)*u*sin(theta2(n)); %friction force x
    Fx(n)=Ff(n)*sin(theta2(n)); %reaction force x
    Fy(n)=Ff(n)*cos(theta2(n)); %reaction force y
    F1(n) = (r3*cos(theta31(n))*(k1*(theta2(n)-g)...
        + k2*(theta2(n)-theta31(n)-g+h)))...
        /(r2*r3*sin(theta2(n)-theta31(n))); %virtual work force 1
    F2(n) = (r2*cos(theta2(n))*(k3*(h-theta31(n))))...
        /(r2*r3*sin(theta2(n)-theta31(n))); %virtual work force 2
    F(n)=F1(n)+F2(n); %total virtual work for 1 segment
    Fd(n)=F(n)*5; %module virutal work force
    Ft1(n)=Fd(n);
    Ftest1(n)=Fd(n)-Ffy(n)+.2*9.81; %output force w losses
E1(n)=.5*k3*5*(theta311(n))^2-Ff(n)*u*r2*theta2(n)...
    +.255*9.81*(r1(n)); %energy w loses
    d11(n) = r1(1)-r1(n); %displacement

    n=n+1;
end
```

```
for n=1:numel(theta2)-1
    Fc(n)=-(E1(n+1)-E1(n))/(r1(n+1)-r1(n)); %force from energy
    rc(n)=r1(1)-r1(n);
    theta21(n)=theta2(n);
end
plot((d11),Ftest1,'blue+',(d11),Fd,'green*','linewidth',2)
axis([min(rc) max1 0 50])
theta2e=(theta2)
u=.225 % coefficient of friction for extension
theta311=0
%%repeat loop as above
for n=1:numel(theta2e)
  theta3(n) = asin((-r2*sin(theta2(n))-r4)/(r3));
    theta311e(n) = (asin(r2*sin(theta2(n))-r4)/r3);
    theta31(n)=(2*pi+theta3(n));
    r2e(n)=r2*cos(theta2e(n))+r3*cos(theta3(n));
     Ffe(n)=5*k3*theta311e(n)/((((cos(theta2(n))+...
         u*sin(theta2(n)))*gama*L*sin(theta311e(n)))...
         +(sin(theta2(n))-u*cos(theta2(n)))*gama*L*cos(theta311e(n)));
    Ffy(n)=Ffe(n)*u*cos(theta2e(n));
    Ffx(n)=Ffe(n)*u*sin(theta2e(n));
    Fx(n)=Ffe(n)*sin(theta2e(n));
    Fy(n)=Ffe(n)*cos(theta2e(n));
    Rye(n)=Ffe(n)*cos(theta2e(n))+u*Ffe(n)*sin(theta2(n));
   Fmease(n)=Ry(n)-.155*9.81;
   F1(n) = (r3*cos(theta31(n))*(k1*(theta2e(n)-g) + k2*(theta2e(n)-...
       theta31(n)-g+h)))/(r2*r3*sin(theta2e(n)-theta31(n)));
    F2(n) = (r2*cos(theta2e(n))*(k3*(h-theta31(n))))...
        /(r2*r3*sin(theta2e(n)...-theta31(n)));
    F(n)=F1(n)+F2(n);
    Fd(n)=F(n)*5;
    Ft2(n)=Fd(n);
end
Fd=fliplr(Ft2)
for n=1:numel(theta2e)
   Ftest2(n)=Fd(n)-Ffy(n)-.2*9.81;
E2(n)=.5*k3*5*(theta311e(n))^2-
Ffe(n)*u*r2*theta2e(n)+.255*9.81*(r2e(n));
    d2(n) = r2e(n)-r2e(1);
    n=n+1;
end
for n=1:numel(theta2e)-1
   E22(n)=.5*k3*5*(theta311(n+1)-theta311(n))^2-Ffe(n)*u*r2*...
       (-theta2e(n+1)+theta2e(n))+.255*9.81*(-r2e(n+1)+r2e(n));
    Fe(n)=(E2(n)-E2(n+1))/(r2e(n+1)-r2e(n));
    re(n)=d2(n);
    theta2e1(n)=theta2e(n);
end
hold on
plot((abs(d2)),(Ftest2),'redo','linewidth',2)
 %,abs(fliplr(re)),Fe,'green')
%plot((abs(re)),(Fe),'red')

%%input data vector from test data removed for thesis
  %theta2(n) = (acos((r1^2+r2^2-r3^2)/(2*r1*r2)));
  %%for data manipulation this loop finds r1 based on test data and
theta2
```

```
  for kk=1:numel(data(:,1))
      r1test(kk)=r2+r3-data(kk,1)/1000-data(1,1)/1000;
      theta2test(kk)=real(acos((r1test(kk)^2+r2^2-r3^2)...
          /(2*r1test(kk)*r2)));
  test(kk,1)=theta2test(kk);
  end
plot(data(:,1)/1000,data(:,2),'black','Linewidth',2)
xlabel({'';'Distance, m'},'FontSize',15)
ylabel({'Force, N';''},'FontSize',15)
title({'Force vs. Deflection';''},'FontSize',20)
legend('Compression ','Virtual Work', 'Extension ','Test Data')
legend('boxoff')
```

APPENDIX C

MAPLE® EQUATION OF MOTION DERIVATION CODE

```
> restart;
> ##BEGIN KINEMATICS
> eq1:=r2*cos(theta(t))+r3*cos(theta3(t))=r1;
> eq2:=r2*sin(theta(t))+r3*sin(theta3(t))=0;
> theta3(t):=solve(eq2,theta3(t));
> theta23(t):=Pi+theta3(t)-theta(t)-2*Pi;
> theta31(t):=arcsin(r2/r3*theta(t));
> r1:=solve(eq1,r1);
> r1dot:=diff(r1,t);
> r1dotdot:=diff(r1dot,t);
> ##END KINEMTAICS
> #PE:=.5*K*theta31(t)^2-ms*g*r1-
mprbm*g*(r2*cos(theta(t))+r3/2*cos(theta3(t))):
##IDEAL PE WITHOUT LOSSES
> F:=int(-20.826*theta^2+29.739*theta+7.9425,theta):
##FORCE DEFLECTION CURVE
> PE:=-
.0188/3*theta(t)^3+8.6991/2*theta(t)^2+20.266*theta(t):
##PE FROM FORCE CURVE
>
v3sq:=expand(diff((r2*cos(theta(t))+r3*cos(theta3(t))),t)^2
):
##VELOCITY OF LINK 3 SQUARED:
> KE1:=(.5*ms*r1dot^2): ##KE PLATEN
> KE2:=.5*mprbm*(-r2*sin(theta(t))*(diff(theta(t), t))
-r2^2*sin(theta(t))*cos(theta(t))*(diff(theta(t),
 t))*.5/(r3*sqrt(1-r2^2*sin(theta(t))^2/r3^2)))^2:
##PLANAR KE OF LINK 3;
> KE3:=.5*J3*diff(theta31(t),t)^2:
##ROTATIONAL KE OF LINK 3:
> Lagrangian:=KE1+KE2+KE3-PE:
> with(VariationalCalculus);
> test:=EulerLagrange(Lagrangian,t,theta(t)):
##TEST IS EOM
> subs(theta(t)=disp,subs(diff(theta(t),t)=vel,
subs(arcsin=asin,subs(arccos=acos,subs(diff(theta(t),
t$2)=accel,(test[1])))))):
##COPY PASTE INTO MATLAB AND SOLVE FOR ACCEL
>
```

APPENDIX D

MAPLE® NORMALIZED ENERGY CODE

```
restart;
with(plots);
AA:=linalg[matrix](4,4,[1,0,1,1,0,1,1,-1,
-cos(alpha),-sin(alpha),exp(alpha),exp(-alpha),sin(alpha)
,-cos(alpha),exp(alpha),-exp(-alpha)]);
##matrix for canitlever beam
eigvals:=[1.8751040687119611664,4.6940911329741745764,7.8547574382376125649
,10.995540734875466991,14.137168391046470581]:
##eigenvalues for cantilever beam
Lb:=11.5*.0254;#length
b:=.5*.0254;#width
 h:=.015*.0254;#thickness
rhobar:=7700;#density
Ab := b*h;
rho:=rhobar*Ab;
Yb:=207000e6;#modulus
Ib:=b*h^3/12;
uL:=2*.0254:#initial deflection
##Vibrations math below this line
omegas := [seq(sqrt(Yb*Ib/(rhobar*Ab*Lb^4))*eigvals[i]^2, i = 1 .. nops(eigvals))];
fns:= [seq(evalf((sqrt(Yb*Ib/(rhobar*Ab*Lb^4))*eigvals[i]^2)/2/Pi), i = 1 .. nops(eigvals))]:
AAinv:= linalg[inverse]( linalg[delrows]( linalg[delcols]( AA, 4..4 ), 4..4 ) ):
col4:= matrix(3, 1, [
  [-linalg[col]( AA, 4) [1] ],
  [-linalg[col](AA, 4) [2] ],
  [-linalg[col]( AA, 4) [3] ]
                    ]):
solnVec:= linalg[multiply](AAinv, col4):

B1:= linalg[col]( solnVec, 1 )[1]:
                          B2:= linalg[col]( solnVec, 1 )[2]:
                          B3:= linalg[col]( solnVec, 1 )[3]:
```

```
B4:= 1:

U:=unapply(B1*cos(alpha*x/Lb)+B2*sin(alpha*x/Lb)+B3*exp(alpha*x/Lb)+B4*exp(-alpha*x/Lb),x,alpha):

plot(diff(U(x,eigvals[3]),x$2),x=0..Lb);

Nn:=[seq(int(U(x, eigvals[i])*(U(x, eigvals[i])),x=0..Lb),i=1..nops(eigvals))]:

eta0 := unapply(uL*(int((3*x^2-x^3/Lb)*U(x, alpha), x = 0 .. Lb))/(2*Lb^2*N_), alpha, N_); eta :=
unapply(eta0(alpha, N_)*cos(omega*t), t, omega, alpha, N_);

phi := Sum(U(Lb, eigvals[i])*eta(t, omegas[i], eigvals[i], Nn[i]), i = 1 .. n);

Phi := unapply(phi, t, n);

phi1 := Sum(U(Lb, eigvals[i])*diff(eta(t, omegas[i], eigvals[i], Nn[i]),t), i = 1 .. n):

Phi1 := unapply(phi1, t, n):

##End lots of math

P3 := plot(Phi(t, 3), t = 0 .. 20, color = "Green", numpoints = 1000, legend = "3");

P4 := plot(Phi(t, 4), t = 0 .. 20, color = "SteelBlue", numpoints = 1000, legend = "3");

P5 := plot(Phi(t, 5), t = 0 .. 20, color = "SteelBlue", numpoints = 1000, legend = "4");

ph1 := Sum(U(x, eigvals[i])*eta(t, omegas[i], eigvals[i], Nn[i]), i = 1 .. 1);

ph2 := Sum(U(x, eigvals[i])*eta(t, omegas[i], eigvals[i], Nn[i]), i = 2 .. 2);

ph3 := Sum(U(x, eigvals[i])*eta(t, omegas[i], eigvals[i], Nn[i]), i = 3 .. 3);

ph4 := Sum(U(x, eigvals[i])*eta(t, omegas[i], eigvals[i], Nn[i]), i = 4 .. 4);

ph5 := Sum(U(x, eigvals[i])*eta(t, omegas[i], eigvals[i], Nn[i]), i = 5 .. 5);

PE1:=(evalf(.5*int((diff(ph1,x$2))^2,x=0..Lb))):

PE2 := evalf(.5*(int((diff(ph2, `$`(x, 2)))^2, x = 0 .. Lb)));

PE3 := evalf(.5*(int((diff(ph3, `$`(x, 2)))^2, x = 0 .. Lb)));

PE4 := evalf(.5*(int((diff(ph4, `$`(x, 2)))^2, x = 0 .. Lb)));

PE5 := evalf(.5*(int((diff(ph5, `$`(x, 2)))^2, x = 0 .. Lb)));


PP1 := plot(PE1, t = 0 .. 4*(1/10), color = "SteelBlue", legend = "Mode 1");

PP2 := plot(PE2, t = 0 .. 4*(1/10), color = "Black", legend = "Mode 2");

PP3 := plot(PE3, t = 0 .. 4*(1/10), color = "Red", legend = "Mode 3");

PP4 := plot(PE4, t = 0 .. 4*(1/10), color = "Green", legend = "Mode 4");

PP5:=plot(PE5,t=0..4/10,color="Purple",legend="Mode 5"):

 display([PP1,PP2,PP3,PP4,PP5],labels=([typeset("\n Time"),typeset(" Potential
Energy\n")]),labeldirections=[horizontal,vertical],title=typeset("Stiffness Normalized Potential Energy vs
Time\n "),titlefont = ["ROMAN", 22, "bold"], labelfont = ["ROMAN", 18, "bold"], legendstyle = [font =
```

```
["ROMAN", 18], location = right], axes = boxed, size = [1000, 500], axesfont = ["ROMAN", 18], numpoints =
10000 ):

PP1 := plot(PE1, t = 0 .. 1/10, y = 0 .. 5*(1/1000), color = "SteelBlue", legend = "Mode 1");

PP2 := plot(PE2, t = 0 .. 1/10, y = 0 .. 5*(1/1000), color = "Black", legend = "Mode 2");

PP3 := plot(PE3, t = 0 .. 1/10, y = 0 .. 5*(1/1000), color = "Red", legend = "Mode 3");

PP4 := plot(PE4, t = 0 .. 1/10, y = 0 .. 5*(1/1000), color = "Green", legend = "Mode 4");

PP5:=plot(PE5,t=0..1/10,y=0..5/(1000),color="Purple",legend="Mode 5"):

display([PP1, PP2, PP3, PP4, PP5], labels = [typeset("\n Time"), typeset(" Potential Energy\n")],
labeldirections = [horizontal, vertical], title = typeset("Stiffness Normalized Potential Energy vs Time\n "),
titlefont = ["ROMAN", 22, "bold"], labelfont = ["ROMAN", 18, "bold"], legendstyle = [font = ["ROMAN",
18], location = right], axes = boxed, size = [1000, 500], axesfont = ["ROMAN", 18], numpoints = 10000);

kE1:=(evalf(.5*int((diff(ph1,t))^2,x=0..Lb))):

kE2 := evalf(.5*(int((diff(ph2, t))^2, x = 0 .. Lb)));

kE3 := evalf(.5*(int((diff(ph3, t))^2, x = 0 .. Lb)));

kE4 := evalf(.5*(int((diff(ph4, t))^2, x = 0 .. Lb)));

kE5 := evalf(.5*(int((diff(ph5, t))^2, x = 0 .. Lb)));

KP1 := plot(kE1, t = 0 .. 4*(1/10), color = "SteelBlue", legend = "Mode 1");

kP2 := plot(kE2, t = 0 .. 4*(1/10), color = "Black", legend = "Mode 2");

kP3 := plot(kE3, t = 0 .. 4*(1/10), color = "Red", legend = "Mode 3");

kP4 := plot(kE4, t = 0 .. 4*(1/10), color = "Green", legend = "Mode 4");

kP5:=plot(Pk5,t=0..4/10,color="Purple",legend="Mode 5"):

display([KP1, kP2, kP3, kP4, kP4], labels = [typeset("\n Time"), typeset(" Kinetic Energy\n")],
labeldirections = [horizontal, vertical], title = typeset("Mass Normalized Kinetic Energy vs Time\n "),
titlefont = ["ROMAN", 22, "bold"], labelfont = ["ROMAN", 18, "bold"], legendstyle = [font = ["ROMAN",
18], location = right], axes = boxed, size = [1000, 500], axesfont = ["ROMAN", 18], numpoints = 10000);

KP1 := plot(kE1, t = 0 .. 1/10, y = 0 .. 5*(1/1000), color = "SteelBlue", legend = "Mode 1");

kP2 := plot(kE2, t = 0 .. 1/10, y = 0 .. 5*(1/1000), color = "Black", legend = "Mode 2");

kP3 := plot(kE3, t = 0 .. 1/10, y = 0 .. 5*(1/1000), color = "Red", legend = "Mode 3");

kP4 := plot(kE4, t = 0 .. 1/10, y = 0 .. 5*(1/1000), color = "Green", legend = "Mode 4");

kP5:=plot(Pk5,t=0..4/10,y=0..5/(1000),color="Purple",legend="Mode 5"):

display([KP1, kP2, kP3, kP4, kP4], labels = [typeset("\n Time"), typeset(" Kinetic Energy\n")],
labeldirections = [horizontal, vertical], title = typeset("Mass Normalized Kinetic Energy vs Time\n "),
titlefont = ["ROMAN", 22, "bold"], labelfont = ["ROMAN", 18, "bold"], legendstyle = [font = ["ROMAN",
18], location = right], axes = boxed, size = [1000, 500], axesfont = ["ROMAN", 18], numpoints = 1000
```

APPENDIX E

MATLAB® SINGLE SEGMENT DYNAMICS CODE

Main Program

```
clear all
close all
clc
%%declare globals
global b
global w
global gamma
global L
global Ktheta
global Area
global rhobar
global beta
global E
global I
global x0
global v0
global tstep
global tfinal
global rho
global theta0
global thetadot0
global K
global Mass
global x01
global x02
global theta01
global theta02
global v01
global v02
global thetadot01
global thetadot02
global zeta2
global zeta1
global tinitial01
global tinitial
global g

load test0017.csv
a=test0017;
raw_data1=a(:,2)*1000*9.80665;
offset=sum(raw_data1)/numel(raw_data1);
raw_data=raw_data1/offset;
t=a(:,1);
rawpeaks=findpeaks(raw_data);
rawpkmax=find(rawpeaks==max(rawpeaks));
plotrawpks=rawpeaks(rawpkmax:numel(rawpeaks));
%load data and find peaks of data
tinitial=t(1);
g=-9.81

n11=1;
n12=10;
n1=n12-n11;
x11=plotrawpks(n11);
x1n=plotrawpks(n12);
```

```
delta1=1/n1*log(x11/x1n);
zeta1=1/(sqrt(1+(2*pi/delta1)^2));
%%determine damping 1
recl=(t(numel(t))-t(1));
fs= 1/(t(2)-t(1));
taus=1/fs;
nsamples=numel(t);

deltaf=1/recl;
fscale=deltaf;
xp=fft(raw_data,nsamples);
xp=abs(xp)/nsamples;
f=fscale*(0:(nsamples/2)-1);

plot(f,xp(1:nsamples/2));
axis([0 500 0 2e-4])
xlabel('frequency   hertz')
ylabel('spectral amplitude')
title('FFT of Machinery Noise Time Signal')
%%FFT algorithim above




b=2.15*.0254; %%width in meters
w=.125*.0254; %%thickness in meters
gamma=.8517; %gamma
L=11*.0254; %length in meters
Ktheta=2.65;
Area=b*w;
rhobar=2000 ;%density in kg/m^3
rho=rhobar*Area;
beta=1.8751040687119611664;
E=     1.5e9; %Young's modulus in Pa
I=1/12*b*w^3;
x01=-6.1*.0254; %initial x deflection in meters
theta01=asin(x01/(gamma*L)); %theta0
theta02=asin(x02/(gamma*L)); %theta0
v01=0; %initial velocity
thetadot01=v01/cos(theta01);
thetadot02=v02/cos(theta02);%initial thetadot
tfinal=t(numel(t));% final time in sec
tstep=  t(2)-t(1); %time step
K=gamma*Ktheta*E*I/L; %%Spring value for beam
Mass=rho*gamma*L %%Mass value for beam
global J
J=1/12*Mass*(gamma*L)^2;


%%%%

%%pass to ODE 45 and solve
[time1,disp11]=second_oder_ode2();  %damping ratio 1
disp1=disp11(:,1); %displacement 1 from damping ratio 1
peaks1=findpeaks(real(disp1(:,1))); %local maxima from damping ratio 1
```

```
pp=0;
  for i=1:numel(peaks1)-2; %if ratio 1 gives, go to this loop
if real(peaks1(i))>asin(.15/gamma); % condition for small deflection
            y1(i)=peaks1(i); %data tracking of peaks bigger than
condition
            z1=y1(i); %data tracking
           q1(i)=peaks1(i+1);
           v1=q1(i);
           zzz=find(real(disp1)==v1);
           xx=find(real(disp1)==z1); %find output of ODE45 that meets
the condtion

           pp=pp+1;

           for jj=1:(zzz-xx)
               zeros1(jj)=min((disp1(jj+xx)));

           end
           minzero=(min(real(abs(real(zeros1)))));
           zeroindex=find(abs(real(zeros1))==minzero);
         zerocross23=find(disp1==zeros1(zeroindex));
           for p=1:zerocross23;
               xfinal(p)=disp1(p); %store output from ODE 45
               timefinal(p)=time1(p);
           end

else

end

  end
  %%damping 2
  n21=pp;
n22=pp+5;
n2=n22-n21;
x21=rawpeaks(n21);
x2n=rawpeaks(n22);
 delta2=1/n2*log(x21/x2n);
  zeta2=1/(sqrt(1+(2*pi/delta2)^2));

thetadot02=disp11(zerocross23,2);
theta02=disp11(zerocross23,1);
tinitial01=timefinal(zerocross23);

[time2,disp22]=second_oder_ode();  %damping ratio 2

disp2=disp22(:,1); %displacement 2 from damping ratio 2

peaks2=findpeaks(real((disp2(:,1)))); %local maxima from damping ratio
2
y1=zeros(numel(peaks2),1);
xfinal=zeros(numel(time2),1);
timefinal=zeros(numel(time2),1);
y2=zeros(numel(peaks2),1);
 timenew=tinitial:tstep:tfinal;
```

```
 %%merge two solutions of ODE
for jj=1:zerocross23;
    xnew(jj)=disp1(jj);
    vnew(jj)=disp11(jj,2);
end
for kk=zerocross23+1:numel(time1);
    xnew(kk)=disp2(kk-zerocross23);
    vnew(kk)=disp22(kk-zerocross23,2);
end



%%find disp, vel and accel of beam end
   thetadotdot=diff(vnew)/tstep;
time4=[tinitial:tstep:tfinal-tstep];
for kk=1:numel(thetadotdot);

    tk(kk)=timenew(kk);
disptip(kk)=gamma*L*sin(xnew(kk));
vel(kk)=gamma*L*(cos(-1*xnew(kk)))*-1*vnew(kk);
accel(kk)=-gamma*L*(sin(-1*xnew(kk)))*(1*vnew(kk))^2...
+gamma*L*cos(xnew(kk))*thetadotdot(kk);

end

reclt=(timenew(numel(timenew))-timenew(1));
fst= 1/(timenew(2)-timenew(1));
taust=1/fst;
nsamplest=numel(timenew);

deltaft=1/reclt;
fscalet=deltaft;
xpt=fft(accel,nsamplest);
xpt=abs(xpt)/nsamplest;
ft=fscalet*(0:(nsamplest/2)-1);
%%FFT for model above
figure(3)
plot(ft,xpt(1:nsamplest/2),f,xp(1:nsamples/2));
xlabel('Frequency,Hz')
ylabel('Spectral Amplitude')
title('FFT of Raw and Predicted Signals')
axis([0 75 0 30])
legend('Experimental','Predicted','Location','SouthEast')

peaksnew=findpeaks(accel);
rawpkmax=find(rawpeaks==max(rawpeaks));
plotrawpks=rawpeaks(rawpkmax:numel(rawpeaks));

%figure(1)
%plot(t,raw_data,tk,accel,tk,disptip*1000,time2,disp2*1000)

figure(2)
plot(t,raw_data,tk,accel)
xlabel('Time,sec')
ylabel('Acceleration,m/s^2')
```

```
title('Raw and Predicted Acceleration')
%axis([0 75 0 30])
legend('Experimental','Predicted','Location','SouthEast')

figure(4)
plot(plotrawpks)
hold on
plot(findpeaks(accel,'MinPeakDistance',600),'green')
hold off
xlabel('Sample Number')
ylabel('Amplitude m/s^2')
title('Peaks of Raw and Predicted Signals')
%axis([0 75 0 30])
legend('Experimental','Predicted','Location','NorthEast')
```

ODE 45 Solver

```
function [t,x]=second_oder_ode() % add output argument

% SOLVE  d2x/dt2+5 dx/dt - 4 x = sin(10 t)
% initial conditions: x(0) = 0, x'(0)=0
%%copy these variables to second_oder_ode
global b
global w
global gamma
global L
global Ktheta
global Area
global rhobar
global beta
global E
global I
global x0
global v0
global tstep
global tfinal
global rho
global theta0
global thetadot0
global K
global Mass
global x02
global theta02
global v02
global thetadot02
global zeta2
global tinitial01
global g
global J
%%%%

t= tinitial01:tstep:tfinal;   % time scale

initial_x    = theta02;
initial_dxdt = thetadot02;
```

```
[t,x]=ode45( @rhs, t, [initial_x initial_dxdt] );

plot(t,x(:,1),'green');
xlabel('t'); ylabel('x');

    function dxdt=rhs(t,x);

        dxdt_1 = x(2);
        K_t=(.004233+2.567095*x(1)-.037173*x(1)^2+.17997*x(1)^3)/x(1);

       % dxdt_2=(-
L^2*cos(x(1))^2*Mass*x(2)^2+4*3.001399338*zeta2*x(2)+4*K*x(1))/(L*L*cos
(x(1))*sin(x(1))*Mass);
      % dxdt_2=-2*zeta2*sqrt(K/Mass)*x(2)-K/Mass*x(1);
    %  dxdt_2=-
2*(Mass*g*sin(x(1))*gamma*L+2*K*x(1)+4*sqrt(K/Mass)*zeta2*x(2))/(Mass*g
amma^2*L^2)  ;
      dxdt_2=-K*x(1)/J-2*sqrt(K/J)*zeta2*x(2)-gamma*L/2*Mass*sin(x(1));

    dxdt=[dxdt_1; dxdt_2];

    end

end
```

APPENDIX F

MATLAB® DYNAMIC CFM CODE

```
clear all

clc
hold on
global b
global h
global gama
global L
global Kt
global Area
global rhobar
global beta
global E
global I
global x0
global v0
global tstep
global tfinal
global rho
global theta0
global thetadot0
global K
global mprbm
global zeta1
global tinitial
global r3
global r2
global Ib
global ms
global g
global m2
global J3
m2=0;

b=.5*.0254; %%width in meters
h=.015*.0254; %%thickness in meters
gama=.8276; %gamma
L=2.25*.0254; %length in meters
Kt=2.59707;
Area=b*h;
rhobar=7700;%density in kg/m^3
rho=rhobar*Area;
beta=1.875;
E=210e9; %Young's modulus in Pa
Ib=1/12*b*h^3;
tfinal=.5;% final time in sec
g=-9.81
tinitial=0
tfinal=.1;% final time in sec
tstep=  .0001; %time step
K=gama*Kt*E*5*Ib/L; %%Spring value for beam
ms=.255
r2=1.59*.0254;
r3=gama*L;
theta0=35*pi/180;
v0=0; %initial velocity
mprbm=gama*L*rho
```

```
thetadot0=0;
J3=1/12*mprbm*r3^2;
global C
global tum
global u1
global u2
global zeta2
global Pi
Pi=pi
u1=0
u2=0
tum=0
global offset
global Er
global r4
offset=0
%%%%
r4=0;
Er=r4/r2
R=.8853
k1=0
k2=0
k3=K
[time1,disp11]=second_oder_ode_cfm();  %damping ratio 1
disp1=disp11(:,1); %displacement 1 from damping ratio 1
r=r2*cos(disp11(1))+r3*cos(asin(-r2*sin(disp1(1))/r3))+(1-gama)*L;
 for kk=1:numel(time1)-1
    theta2(kk)=disp1(kk);
    x(1)=disp1(kk);
    x(2)=disp11(kk,2);
    theta3(kk)=-asin((r2*sin(x(1)))/r3);
    theta31(kk)=2*Pi+asin((r2*sin(x(1)))/r3);
    r1(kk)=r2*cos(x(1))+r3*sqrt(1-(r2*sin(x(1)))^2/r3^2);
    tum=0;
    %tum=(-r2*sin(x(1))-r2^2*sin(x(1))*cos(x(1))/(r3^2-
r2^2*sin(x(1))^2))*u2;
    %tum=u1*K*x(1)*L*theta3(kk)+offset+u2*(-r2*sin(x(1))*x(2)-
r2^2*sin(x(1))*cos(x(1))*x(2)/(r3*sqrt(1-r2^2*sin(x(1))^2/r3^2)));
   tum1(kk)=tum;
    r1dot(kk)=-r2*sin(x(1))*x(2)-(r2*sin(x(1))-
r4)*r2*cos(x(1))*x(2)/(r3*sqrt(1-(r2*sin(x(1))-r4)^2/r3^2));
thetadotdot(kk)=(.50*(2.00*K*asin(r2*x(1.00)/r3)*r3^8.00+2.00*x(2.00)^2
.00*sqrt(-(1.00*(r2^2.00*x(1.00)^2.00-
1.00*r3^2.00))/r3^2.00)*sin(x(1.00))*cos(x(1.00))^3.00*ms*r2^3.00*r3^7.
00-2.00*x(2.00)^2.00*sqrt(-(1.00*(r2^2.00*x(1.00)^2.00-
1.00*r3^2.00))/r3^2.00)*sin(x(1.00))^3.00*(-
(1.00*(r2^2.00*sin(x(1.00))^2.00-
1.00*r3^2.00))/r3^2.00)^(3.00/(2.00))*ms*r2^2.00*r3^8.00+2.00*J3*x(1.00
)*x(2.00)^2.00*sqrt(-(1.00*(r2^2.00*x(1.00)^2.00-
1.00*r3^2.00))/r3^2.00)*sin(x(1.00))^4.00*r2^7.00*r3-
4.00*J3*x(1.00)*x(2.00)^2.00*sqrt(-(1.00*(r2^2.00*x(1.00)^2.00-
1.00*r3^2.00))/r3^2.00)*sin(x(1.00))^2.00*r2^5.00*r3^3.00+2.00*x(1.00)^
4.00*sqrt(-(1.00*(r2^2.00*x(1.00)^2.00-
1.00*r3^2.00))/r3^2.00)*sin(x(1.00))^5.00*g*ms*r2^8.00*r3-
4.00*x(1.00)^4.00*sqrt(-(1.00*(r2^2.00*x(1.00)^2.00-
1.00*r3^2.00))/r3^2.00)*sin(x(1.00))^3.00*g*ms*r2^6.00*r3^3.00+2.00*x(1
.00)^4.00*sqrt(-(1.00*(r2^2.00*x(1.00)^2.00-
```

```
1.00*r3^2.00))/r3^2.00)*sin(x(1.00))*g*ms*r2^4.00*r3^5.00-
4.00*x(1.00)^2.00*sqrt(-(1.00*(r2^2.00*x(1.00)^2.00-
1.00*r3^2.00))/r3^2.00)*sin(x(1.00))^5.00*g*ms*r2^6.00*r3^3.00+8.00*x(1
.00)^2.00*sqrt(-(1.00*(r2^2.00*x(1.00)^2.00-
1.00*r3^2.00))/r3^2.00)*sin(x(1.00))^3.00*g*ms*r2^4.00*r3^5.00-
4.00*x(1.00)^2.00*sqrt(-(1.00*(r2^2.00*x(1.00)^2.00-
1.00*r3^2.00))/r3^2.00)*sin(x(1.00))*g*ms*r2^2.00*r3^7.00+2.00*x(1.00)^
4.00*sqrt(-(1.00*(r2^2.00*x(1.00)^2.00-
1.00*r3^2.00))/r3^2.00)*sin(x(1.00))^5.00*g*mprbm*r2^8.00*r3-
4.00*x(1.00)^4.00*sqrt(-(1.00*(r2^2.00*x(1.00)^2.00-
1.00*r3^2.00))/r3^2.00)*sin(x(1.00))^3.00*g*mprbm*r2^6.00*r3^3.00+2.00*
x(1.00)^4.00*sqrt(-(1.00*(r2^2.00*x(1.00)^2.00-
1.00*r3^2.00))/r3^2.00)*sin(x(1.00))*g*mprbm*r2^4.00*r3^5.00-
4.00*x(1.00)^2.00*sqrt(-(1.00*(r2^2.00*x(1.00)^2.00-
1.00*r3^2.00))/r3^2.00)*sin(x(1.00))^5.00*g*mprbm*r2^6.00*r3^3.00+8.00*
x(1.00)^2.00*sqrt(-(1.00*(r2^2.00*x(1.00)^2.00-
1.00*r3^2.00))/r3^2.00)*sin(x(1.00))^3.00*g*mprbm*r2^4.00*r3^5.00-
4.00*K*x(1.00)^4.00*asin(r2*x(1.00)/r3)*sin(x(1.00))^2.00*r2^6.00*r3^2.
00-
4.00*K*x(1.00)^2.00*asin(r2*x(1.00)/r3)*sin(x(1.00))^4.00*r2^6.00*r3^2.
00+2.00*sqrt(-(1.00*(r2^2.00*x(1.00)^2.00-
1.00*r3^2.00))/r3^2.00)*sin(x(1.00))^5.00*g*mprbm*r2^4.00*r3^5.00-
4.00*sqrt(-(1.00*(r2^2.00*x(1.00)^2.00-
1.00*r3^2.00))/r3^2.00)*sin(x(1.00))^3.00*g*mprbm*r2^2.00*r3^7.00+2.00*
sqrt(-(1.00*(r2^2.00*x(1.00)^2.00-
1.00*r3^2.00))/r3^2.00)*sin(x(1.00))^5.00*g*ms*r2^4.00*r3^5.00-
4.00*sqrt(-(1.00*(r2^2.00*x(1.00)^2.00-
1.00*r3^2.00))/r3^2.00)*sin(x(1.00))^3.00*g*ms*r2^2.00*r3^7.00-
4.00*x(1.00)^2.00*sqrt(-(1.00*(r2^2.00*x(1.00)^2.00-
1.00*r3^2.00))/r3^2.00)*sin(x(1.00))*g*mprbm*r2^2.00*r3^7.00+4.00*x(2.0
0)^2.00*sqrt(-(1.00*(r2^2.00*x(1.00)^2.00-
1.00*r3^2.00))/r3^2.00)*sin(x(1.00))^5.00*cos(x(1.00))*ms*r2^5.00*r3^5.
00-6.00*x(2.00)^2.00*sqrt(-(1.00*(r2^2.00*x(1.00)^2.00-
1.00*r3^2.00))/r3^2.00)*sin(x(1.00))^3.00*cos(x(1.00))*ms*r2^3.00*r3^7.
00+2.00*x(2.00)^2.00*sqrt(-(1.00*(r2^2.00*x(1.00)^2.00-
1.00*r3^2.00))/r3^2.00)*sin(x(1.00))*cos(x(1.00))*ms*r2*r3^9.00+2.00*sq
rt(-(1.00*(r2^2.00*x(1.00)^2.00-1.00*r3^2.00))/r3^2.00)*sin(x(1.00))*(-
(1.00*(r2^2.00*sin(x(1.00))^2.00-
1.00*r3^2.00))/r3^2.00)^(3.00/(2.00))*cos(x(1.00))*g*ms*r2*r3^8.00-
4.00*x(1.00)^2.00*x(2.00)^2.00*sqrt(-(1.00*(r2^2.00*x(1.00)^2.00-
1.00*r3^2.00))/r3^2.00)*sin(x(1.00))*cos(x(1.00))*ms*r2^3.00*r3^7.00+2.
00*x(1.00)^4.00*x(2.00)^2.00*sqrt(-(1.00*(r2^2.00*x(1.00)^2.00-
1.00*r3^2.00))/r3^2.00)*sin(x(1.00))*cos(x(1.00))^3.00*ms*r2^7.00*r3^3.
00-4.00*x(1.00)^2.00*sqrt(-(1.00*(r2^2.00*x(1.00)^2.00-
1.00*r3^2.00))/r3^2.00)*sin(x(1.00))*(-
(1.00*(r2^2.00*sin(x(1.00))^2.00-
1.00*r3^2.00))/r3^2.00)^(3.00/(2.00))*cos(x(1.00))*g*ms*r2^3.00*r3^6.00
+2.00*x(1.00)^4.00*sqrt(-(1.00*(r2^2.00*x(1.00)^2.00-
1.00*r3^2.00))/r3^2.00)*sin(x(1.00))*(-
(1.00*(r2^2.00*sin(x(1.00))^2.00-
1.00*r3^2.00))/r3^2.00)^(3.00/(2.00))*cos(x(1.00))*g*ms*r2^5.00*r3^4.00
-2.00*x(1.00)^2.00*sqrt(-(1.00*(r2^2.00*x(1.00)^2.00-
1.00*r3^2.00))/r3^2.00)*sin(x(1.00))*(-
(1.00*(r2^2.00*sin(x(1.00))^2.00-
1.00*r3^2.00))/r3^2.00)^(3.00/(2.00))*cos(x(1.00))*g*mprbm*r2^3.00*r3^6
.00-6.00*x(1.00)^4.00*x(2.00)^2.00*sqrt(-(1.00*(r2^2.00*x(1.00)^2.00-
1.00*r3^2.00))/r3^2.00)*sin(x(1.00))^3.00*cos(x(1.00))*ms*r2^7.00*r3^3.
```

```
00+4.00*x(1.00)^4.00*x(2.00)^2.00*sqrt(-(1.00*(r2^2.00*x(1.00)^2.00-
1.00*r3^2.00))/r3^2.00)*sin(x(1.00))^5.00*cos(x(1.00))*ms*r2^9.00*r3-
4.00*x(1.00)^2.00*x(2.00)^2.00*sqrt(-(1.00*(r2^2.00*x(1.00)^2.00-
1.00*r3^2.00))/r3^2.00)*sin(x(1.00))*cos(x(1.00))^3.00*ms*r2^5.00*r3^5.
00+12.00*x(1.00)^2.00*x(2.00)^2.00*sqrt(-(1.00*(r2^2.00*x(1.00)^2.00-
1.00*r3^2.00))/r3^2.00)*sin(x(1.00))^3.00*cos(x(1.00))*ms*r2^5.00*r3^5.
00-8.00*x(1.00)^2.00*x(2.00)^2.00*sqrt(-(1.00*(r2^2.00*x(1.00)^2.00-
1.00*r3^2.00))/r3^2.00)*sin(x(1.00))^5.00*cos(x(1.00))*ms*r2^7.00*r3^3.
00+2.00*x(2.00)^2.00*sqrt(-(1.00*(r2^2.00*x(1.00)^2.00-
1.00*r3^2.00))/r3^2.00)*sin(x(1.00))^3.00*sqrt(-
(1.00*(r2^2.00*sin(x(1.00))^2.00-
1.00*r3^2.00))/r3^2.00)*cos(x(1.00))^2.00*ms*r2^4.00*r3^6.00+4.00*x(1.0
0)^2.00*x(2.00)^2.00*sqrt(-(1.00*(r2^2.00*x(1.00)^2.00-
1.00*r3^2.00))/r3^2.00)*sin(x(1.00))^3.00*(-
(1.00*(r2^2.00*sin(x(1.00))^2.00-
1.00*r3^2.00))/r3^2.00)^(3.00/(2.00))*ms*r2^4.00*r3^6.00-
2.00*x(1.00)^4.00*x(2.00)^2.00*sqrt(-(1.00*(r2^2.00*x(1.00)^2.00-
1.00*r3^2.00))/r3^2.00)*sin(x(1.00))^3.00*(-
(1.00*(r2^2.00*sin(x(1.00))^2.00-
1.00*r3^2.00))/r3^2.00)^(3.00/(2.00))*ms*r2^6.00*r3^4.00+4.00*x(2.00)^2
.00*sqrt(-(1.00*(r2^2.00*x(1.00)^2.00-
1.00*r3^2.00))/r3^2.00)*sin(x(1.00))*(-
(1.00*(r2^2.00*sin(x(1.00))^2.00-
1.00*r3^2.00))/r3^2.00)^(3.00/(2.00))*cos(x(1.00))^2.00*ms*r2^2.00*r3^8
.00+2.00*x(1.00)^4.00*x(2.00)^2.00*sqrt(-(1.00*(r2^2.00*x(1.00)^2.00-
1.00*r3^2.00))/r3^2.00)*sin(x(1.00))*cos(x(1.00))*ms*r2^5.00*r3^5.00+sq
rt(-(1.00*(r2^2.00*x(1.00)^2.00-1.00*r3^2.00))/r3^2.00)*sin(x(1.00))*(-
(1.00*(r2^2.00*sin(x(1.00))^2.00-
1.00*r3^2.00))/r3^2.00)^(3.00/(2.00))*cos(x(1.00))*g*mprbm*r2*r3^8.00-
4.00*x(1.00)^2.00*x(2.00)^2.00*sqrt(-(1.00*(r2^2.00*x(1.00)^2.00-
1.00*r3^2.00))/r3^2.00)*sin(x(1.00))^3.00*sqrt(-
(1.00*(r2^2.00*sin(x(1.00))^2.00-
1.00*r3^2.00))/r3^2.00)*cos(x(1.00))^2.00*ms*r2^6.00*r3^4.00+4.00*x(1.0
0)^4.00*x(2.00)^2.00*sqrt(-(1.00*(r2^2.00*x(1.00)^2.00-
1.00*r3^2.00))/r3^2.00)*sin(x(1.00))*(-
(1.00*(r2^2.00*sin(x(1.00))^2.00-
1.00*r3^2.00))/r3^2.00)^(3.00/(2.00))*cos(x(1.00))^2.00*ms*r2^6.00*r3^4
.00+2.00*x(1.00)^4.00*x(2.00)^2.00*sqrt(-(1.00*(r2^2.00*x(1.00)^2.00-
1.00*r3^2.00))/r3^2.00)*sin(x(1.00))^3.00*sqrt(-
(1.00*(r2^2.00*sin(x(1.00))^2.00-
1.00*r3^2.00))/r3^2.00)*cos(x(1.00))^2.00*ms*r2^8.00*r3^2.00-
8.00*x(1.00)^2.00*x(2.00)^2.00*sqrt(-(1.00*(r2^2.00*x(1.00)^2.00-
1.00*r3^2.00))/r3^2.00)*sin(x(1.00))*(-
(1.00*(r2^2.00*sin(x(1.00))^2.00-
1.00*r3^2.00))/r3^2.00)^(3.00/(2.00))*cos(x(1.00))^2.00*ms*r2^4.00*r3^6
.00+x(1.00)^4.00*sqrt(-(1.00*(r2^2.00*x(1.00)^2.00-
1.00*r3^2.00))/r3^2.00)*sin(x(1.00))*(-
(1.00*(r2^2.00*sin(x(1.00))^2.00-
1.00*r3^2.00))/r3^2.00)^(3.00/(2.00))*cos(x(1.00))*g*mprbm*r2^5.00*r3^4
.00+2.00*K*asin(r2*x(1.00)/r3)*sin(x(1.00))^4.00*r2^4.00*r3^4.00-
4.00*K*asin(r2*x(1.00)/r3)*sin(x(1.00))^2.00*r2^2.00*r3^6.00+2.00*K*x(1
.00)^4.00*asin(r2*x(1.00)/r3)*sin(x(1.00))^4.00*r2^8.00+2.00*K*x(1.00)^
4.00*asin(r2*x(1.00)/r3)*r2^4.00*r3^4.00-
4.00*K*x(1.00)^2.00*asin(r2*x(1.00)/r3)*r2^2.00*r3^6.00+2.00*sqrt(-
(1.00*(r2^2.00*x(1.00)^2.00-
1.00*r3^2.00))/r3^2.00)*sin(x(1.00))*g*ms*r3^9.00+2.00*sqrt(-
(1.00*(r2^2.00*x(1.00)^2.00-
```

```
1.00*r3^2.00))/r3^2.00)*sin(x(1.00))*g*mprbm*r3^9.00+8.00*K*x(1.00)^2.0
0*asin(r2*x(1.00)/r3)*sin(x(1.00))^2.00*r2^4.00*r3^4.00+2.00*J3*x(1.00)
*x(2.00)^2.00*sqrt(-(1.00*(r2^2.00*x(1.00)^2.00-
1.00*r3^2.00))/r3^2.00)*r2^3.00*r3^5.00))/(sqrt(-
(1.00*(r2^2.00*x(1.00)^2.00-1.00*r3^2.00))/r3^2.00)*r2*r3*(-
2.00*x(1.00)^4.00*(-(1.00*(r2^2.00*sin(x(1.00))^2.00-
1.00*r3^2.00))/r3^2.00)^(3.00/(2.00))*sin(x(1.00))^2.00*cos(x(1.00))*ms
*r2^5.00*r3^3.00-
1.00*x(1.00)^4.00*sin(x(1.00))^6.00*ms*r2^8.00+x(1.00)^4.00*sin(x(1.00)
)^4.00*cos(x(1.00))^2.00*ms*r2^8.00+2.00*x(1.00)^4.00*sin(x(1.00))^4.00
*ms*r2^6.00*r3^2.00-
1.00*x(1.00)^4.00*sin(x(1.00))^2.00*cos(x(1.00))^2.00*ms*r2^6.00*r3^2.0
0+4.00*x(1.00)^2.00*(-(1.00*(r2^2.00*sin(x(1.00))^2.00-
1.00*r3^2.00))/r3^2.00)^(3.00/(2.00))*sin(x(1.00))^2.00*cos(x(1.00))*ms
*r2^3.00*r3^5.00+2.00*x(1.00)^2.00*sin(x(1.00))^6.00*ms*r2^6.00*r3^2.00
-
2.00*x(1.00)^2.00*sin(x(1.00))^4.00*cos(x(1.00))^2.00*ms*r2^6.00*r3^2.0
0-1.00*x(1.00)^4.00*sin(x(1.00))^2.00*ms*r2^4.00*r3^4.00-
4.00*x(1.00)^2.00*sin(x(1.00))^4.00*ms*r2^4.00*r3^4.00+2.00*x(1.00)^2.0
0*sin(x(1.00))^2.00*cos(x(1.00))^2.00*ms*r2^4.00*r3^4.00-2.00*(-
(1.00*(r2^2.00*sin(x(1.00))^2.00-
1.00*r3^2.00))/r3^2.00)^(3.00/(2.00))*sin(x(1.00))^2.00*cos(x(1.00))*ms
*r2*r3^7.00-
1.00*sin(x(1.00))^6.00*ms*r2^4.00*r3^4.00+sin(x(1.00))^4.00*cos(x(1.00)
)^2.00*ms*r2^4.00*r3^4.00+J3*x(1.00)^2.00*sin(x(1.00))^4.00*r2^6.00+2.0
0*x(1.00)^2.00*sin(x(1.00))^2.00*ms*r2^2.00*r3^6.00+2.00*sin(x(1.00))^4
.00*ms*r2^2.00*r3^6.00-
1.00*sin(x(1.00))^2.00*cos(x(1.00))^2.00*ms*r2^2.00*r3^6.00-
2.00*J3*x(1.00)^2.00*sin(x(1.00))^2.00*r2^4.00*r3^2.00-
1.00*J3*sin(x(1.00))^4.00*r2^4.00*r3^2.00-
1.00*sin(x(1.00))^2.00*ms*r3^8.00+J3*x(1.00)^2.00*r2^2.00*r3^4.00+2.00*
J3*sin(x(1.00))^2.00*r2^2.00*r3^4.00-1.00*J3*r3^6.00));
       %tum=offset+u2*(r2*sin(x(1))*x(2)-
r2^2*sin(x(1))*cos(x(1))*x(2)/(r3*sqrt(1-r2^2*sin(x(1))^2/r3^2)));
       r1dotdot(kk)=-r2*cos(x(1))*x(2)^2-r2*sin(x(1))*thetadotdot(kk)-
(r2*sin(x(1))-r4)^2*r2^2*cos(x(1))^2*x(2)^2/(r3^3*(1-(r2*sin(x(1))-
r4)^2/r3^2)^(3/2))-r2^2*cos(x(1))^2*x(2)^2/(r3*sqrt(1-(r2*sin(x(1))-
r4)^2/r3^2))+(r2*sin(x(1))-r4)*r2*sin(x(1))*x(2)^2/(r3*sqrt(1-
(r2*sin(x(1))-r4)^2/r3^2))-(r2*sin(x(1))-
r4)*r2*cos(x(1))*thetadotdot(kk)/(r3*sqrt(1-(r2*sin(x(1))-r4)^2/r3^2));
    tk(kk)=time1(kk);
    tum1(kk)=tum;
    dr1(kk)=r2+r3+r1(kk);
    KEslider(kk)=.5*(ms)*r1dot(kk)^2;

KEplunger(kk)=.5*mprbm*(r2^2*x(2)^2+.25*r2*r2*cos(x(1))^2*x(2)^2/(1-
r2^2*sin(x(1))^2/r3^2)-
r2*r2*cos(x(1)+asin(r2*sin(x(1))/r3))*x(2)^2*cos(x(1))/sqrt(1-
r2^2*sin(x(1))^2/r3^2));
    PEplunger(kk)=.5*K*theta31(kk)^2;
    PEgravity(kk)=-ms*g*(r1(kk))-mprbm*g*r2*cos(x(1))+(1/2)*r3*sqrt(1-
r2^2*sin(x(1))^2/r3^2);
    KErot(kk)=.5*J3*r2^2*cos(x(1))^2*x(2)^2/(r3^2*(1-
r2^2*sin(x(1))^2/r3^2));
    PEtot(kk)=PEplunger(kk)+PEgravity(kk);
    KEtot(kk)=.5*ms*(-r2*sin(x(1))*x(2)-
r2^2*sin(x(1))*cos(x(1))*x(2)/(r3*sqrt(1-
```

```
r2^2*sin(x(1))^2/r3^2)))^2+.5*mprbm*(r2^2*x(2)^2+.25*r2^2*cos(x(1))^2*x
(2)^2/(1-r2^2*sin(x(1))^2/r3^2)-
r2^2*cos(x(1)+sin(r2*sin(x(1))/r3))*x(2)^2*cos(x(1))/sqrt(1-
r2^2*sin(x(1))^2/r3^2))+.5*J3*r2^2*cos(x(1))^2*x(2)^2/(r3^2*(1-
r2^2*sin(x(1))^2/r3^2));
    end

% lpFilt = designfilt('bandpassfir','FilterOrder',500, ...
%          'CutoffFrequency1',2,'CutoffFrequency2',100, ...
%          'SampleRate',1/(t(2)-t(1)));
% fvtool(lpFilt)
% dataIn = raw_data;
% dataOut = filter(lpFilt,dataIn);
figure(5)
plot((tk),(r1dotdot),'Linewidth' ,2);
axis([0 16e-3 -10 200])
% plot(t,dataOut)
title('Acceleration vs. time','Fontsize',20)
ylabel({'Amplitude, m/s^2',''},'Fontsize',15)
xlabel({'','Time, sec'},'Fontsize',15)
legend('Model','Experimental','Location', 'NorthEast')
legend('boxoff')
```

ODE 45 Solver

```
function [t,x]=second_oder_ode_cfm() % add output argument


% SOLVE  d2x/dt2+5 dx/dt - 4 x = sin(10 t)
% initial conditions: x(0) = 0, x'(0)=0
%%copy these variables to second_oder_ode

global b
global h
global gama
global L
global Kt
global Area
global rhobar
global beta
global E
global I
global x0
global v0
global tstep
global tfinal
global rho
global theta0
global thetadot0
global K
global mprbm
global zeta1
global tinitial
global r3
global r2
global Ib
```

```
global ms
global g
global m2
global rho
global J3
global C
global tum
global u1
global u2
global zeta2
global Pi
global offset
global Er
global r4
%%%%

t= tinitial:tstep:tfinal;   % time scale

initial_x    = theta0;
initial_dxdt = thetadot0;

[t,x]=ode23tb( @rhs, t, [initial_x initial_dxdt], 'NonNegative' );

    function dxdt=rhs(t,x);

        dxdt_1 = x(2);

dxdt_2=(.50*(2.00*K*asin(r2*x(1.00)/r3)*r3^8.00+2.00*x(2.00)^2.00*sqrt(
-(1.00*(r2^2.00*x(1.00)^2.00-
1.00*r3^2.00))/r3^2.00)*sin(x(1.00))*cos(x(1.00))^3.00*ms*r2^3.00*r3^7.
00-2.00*x(2.00)^2.00*sqrt(-(1.00*(r2^2.00*x(1.00)^2.00-
1.00*r3^2.00))/r3^2.00)*sin(x(1.00))^3.00*(-
(1.00*(r2^2.00*sin(x(1.00))^2.00-
1.00*r3^2.00))/r3^2.00)^(3.00/(2.00))*ms*r2^2.00*r3^8.00+2.00*J3*x(1.00
)*x(2.00)^2.00*sqrt(-(1.00*(r2^2.00*x(1.00)^2.00-
1.00*r3^2.00))/r3^2.00)*sin(x(1.00))^4.00*r2^7.00*r3-
4.00*J3*x(1.00)*x(2.00)^2.00*sqrt(-(1.00*(r2^2.00*x(1.00)^2.00-
1.00*r3^2.00))/r3^2.00)*sin(x(1.00))^2.00*r2^5.00*r3^3.00+2.00*x(1.00)^
4.00*sqrt(-(1.00*(r2^2.00*x(1.00)^2.00-
1.00*r3^2.00))/r3^2.00)*sin(x(1.00))^5.00*g*ms*r2^8.00*r3-
4.00*x(1.00)^4.00*sqrt(-(1.00*(r2^2.00*x(1.00)^2.00-
1.00*r3^2.00))/r3^2.00)*sin(x(1.00))^3.00*g*ms*r2^6.00*r3^3.00+2.00*x(1
.00)^4.00*sqrt(-(1.00*(r2^2.00*x(1.00)^2.00-
1.00*r3^2.00))/r3^2.00)*sin(x(1.00))*g*ms*r2^4.00*r3^5.00-
4.00*x(1.00)^2.00*sqrt(-(1.00*(r2^2.00*x(1.00)^2.00-
1.00*r3^2.00))/r3^2.00)*sin(x(1.00))^5.00*g*ms*r2^6.00*r3^3.00+8.00*x(1
.00)^2.00*sqrt(-(1.00*(r2^2.00*x(1.00)^2.00-
1.00*r3^2.00))/r3^2.00)*sin(x(1.00))^3.00*g*ms*r2^4.00*r3^5.00-
4.00*x(1.00)^2.00*sqrt(-(1.00*(r2^2.00*x(1.00)^2.00-
1.00*r3^2.00))/r3^2.00)*sin(x(1.00))*g*ms*r2^2.00*r3^7.00+2.00*x(1.00)^
4.00*sqrt(-(1.00*(r2^2.00*x(1.00)^2.00-
1.00*r3^2.00))/r3^2.00)*sin(x(1.00))^5.00*g*mprbm*r2^8.00*r3-
4.00*x(1.00)^4.00*sqrt(-(1.00*(r2^2.00*x(1.00)^2.00-
1.00*r3^2.00))/r3^2.00)*sin(x(1.00))^3.00*g*mprbm*r2^6.00*r3^3.00+2.00*
x(1.00)^4.00*sqrt(-(1.00*(r2^2.00*x(1.00)^2.00-
1.00*r3^2.00))/r3^2.00)*sin(x(1.00))*g*mprbm*r2^4.00*r3^5.00-
```

```
4.00*x(1.00)^2.00*sqrt(-(1.00*(r2^2.00*x(1.00)^2.00-
1.00*r3^2.00))/r3^2.00)*sin(x(1.00))^5.00*g*mprbm*r2^6.00*r3^3.00+8.00*
x(1.00)^2.00*sqrt(-(1.00*(r2^2.00*x(1.00)^2.00-
1.00*r3^2.00))/r3^2.00)*sin(x(1.00))^3.00*g*mprbm*r2^4.00*r3^5.00-
4.00*K*x(1.00)^4.00*asin(r2*x(1.00)/r3)*sin(x(1.00))^2.00*r2^6.00*r3^2.
00-
4.00*K*x(1.00)^2.00*asin(r2*x(1.00)/r3)*sin(x(1.00))^4.00*r2^6.00*r3^2.
00+2.00*sqrt(-(1.00*(r2^2.00*x(1.00)^2.00-
1.00*r3^2.00))/r3^2.00)*sin(x(1.00))^5.00*g*mprbm*r2^4.00*r3^5.00-
4.00*sqrt(-(1.00*(r2^2.00*x(1.00)^2.00-
1.00*r3^2.00))/r3^2.00)*sin(x(1.00))^3.00*g*mprbm*r2^2.00*r3^7.00+2.00*
sqrt(-(1.00*(r2^2.00*x(1.00)^2.00-
1.00*r3^2.00))/r3^2.00)*sin(x(1.00))^5.00*g*ms*r2^4.00*r3^5.00-
4.00*sqrt(-(1.00*(r2^2.00*x(1.00)^2.00-
1.00*r3^2.00))/r3^2.00)*sin(x(1.00))^3.00*g*ms*r2^2.00*r3^7.00-
4.00*x(1.00)^2.00*sqrt(-(1.00*(r2^2.00*x(1.00)^2.00-
1.00*r3^2.00))/r3^2.00)*sin(x(1.00))*g*mprbm*r2^2.00*r3^7.00+4.00*x(2.0
0)^2.00*sqrt(-(1.00*(r2^2.00*x(1.00)^2.00-
1.00*r3^2.00))/r3^2.00)*sin(x(1.00))^5.00*cos(x(1.00))*ms*r2^5.00*r3^5.
00-6.00*x(2.00)^2.00*sqrt(-(1.00*(r2^2.00*x(1.00)^2.00-
1.00*r3^2.00))/r3^2.00)*sin(x(1.00))^3.00*cos(x(1.00))*ms*r2^3.00*r3^7.
00+2.00*x(2.00)^2.00*sqrt(-(1.00*(r2^2.00*x(1.00)^2.00-
1.00*r3^2.00))/r3^2.00)*sin(x(1.00))*cos(x(1.00))*ms*r2*r3^9.00+2.00*sq
rt(-(1.00*(r2^2.00*x(1.00)^2.00-1.00*r3^2.00))/r3^2.00)*sin(x(1.00))*(-
(1.00*(r2^2.00*sin(x(1.00))^2.00-
1.00*r3^2.00))/r3^2.00)^(3.00/(2.00))*cos(x(1.00))*g*ms*r2*r3^8.00-
4.00*x(1.00)^2.00*x(2.00)^2.00*sqrt(-(1.00*(r2^2.00*x(1.00)^2.00-
1.00*r3^2.00))/r3^2.00)*sin(x(1.00))*cos(x(1.00))*ms*r2^3.00*r3^7.00+2.
00*x(1.00)^4.00*x(2.00)^2.00*sqrt(-(1.00*(r2^2.00*x(1.00)^2.00-
1.00*r3^2.00))/r3^2.00)*sin(x(1.00))*cos(x(1.00))^3.00*ms*r2^7.00*r3^3.
00-4.00*x(1.00)^2.00*sqrt(-(1.00*(r2^2.00*x(1.00)^2.00-
1.00*r3^2.00))/r3^2.00)*sin(x(1.00))*(-
(1.00*(r2^2.00*sin(x(1.00))^2.00-
1.00*r3^2.00))/r3^2.00)^(3.00/(2.00))*cos(x(1.00))*g*ms*r2^3.00*r3^6.00
+2.00*x(1.00)^4.00*sqrt(-(1.00*(r2^2.00*x(1.00)^2.00-
1.00*r3^2.00))/r3^2.00)*sin(x(1.00))*(-
(1.00*(r2^2.00*sin(x(1.00))^2.00-
1.00*r3^2.00))/r3^2.00)^(3.00/(2.00))*cos(x(1.00))*g*ms*r2^5.00*r3^4.00
-2.00*x(1.00)^2.00*sqrt(-(1.00*(r2^2.00*x(1.00)^2.00-
1.00*r3^2.00))/r3^2.00)*sin(x(1.00))*(-
(1.00*(r2^2.00*sin(x(1.00))^2.00-
1.00*r3^2.00))/r3^2.00)^(3.00/(2.00))*cos(x(1.00))*g*mprbm*r2^3.00*r3^6
.00-6.00*x(1.00)^4.00*x(2.00)^2.00*sqrt(-(1.00*(r2^2.00*x(1.00)^2.00-
1.00*r3^2.00))/r3^2.00)*sin(x(1.00))^3.00*cos(x(1.00))*ms*r2^7.00*r3^3.
00+4.00*x(1.00)^4.00*x(2.00)^2.00*sqrt(-(1.00*(r2^2.00*x(1.00)^2.00-
1.00*r3^2.00))/r3^2.00)*sin(x(1.00))^5.00*cos(x(1.00))*ms*r2^9.00*r3-
4.00*x(1.00)^2.00*x(2.00)^2.00*sqrt(-(1.00*(r2^2.00*x(1.00)^2.00-
1.00*r3^2.00))/r3^2.00)*sin(x(1.00))*cos(x(1.00))^3.00*ms*r2^5.00*r3^5.
00+12.00*x(1.00)^2.00*x(2.00)^2.00*sqrt(-(1.00*(r2^2.00*x(1.00)^2.00-
1.00*r3^2.00))/r3^2.00)*sin(x(1.00))^3.00*cos(x(1.00))*ms*r2^5.00*r3^5.
00-8.00*x(1.00)^2.00*x(2.00)^2.00*sqrt(-(1.00*(r2^2.00*x(1.00)^2.00-
1.00*r3^2.00))/r3^2.00)*sin(x(1.00))^5.00*cos(x(1.00))*ms*r2^7.00*r3^3.
00+2.00*x(2.00)^2.00*sqrt(-(1.00*(r2^2.00*x(1.00)^2.00-
1.00*r3^2.00))/r3^2.00)*sin(x(1.00))^3.00*sqrt(-
(1.00*(r2^2.00*sin(x(1.00))^2.00-
1.00*r3^2.00))/r3^2.00)*cos(x(1.00))^2.00*ms*r2^4.00*r3^6.00+4.00*x(1.0
0)^2.00*x(2.00)^2.00*sqrt(-(1.00*(r2^2.00*x(1.00)^2.00-
```

```
1.00*r3^2.00))/r3^2.00)*sin(x(1.00))^3.00*(-
(1.00*(r2^2.00*sin(x(1.00))^2.00-
1.00*r3^2.00))/r3^2.00)^(3.00/(2.00))*ms*r2^4.00*r3^6.00-
2.00*x(1.00)^4.00*x(2.00)^2.00*sqrt(-(1.00*(r2^2.00*x(1.00)^2.00-
1.00*r3^2.00))/r3^2.00)*sin(x(1.00))^3.00*(-
(1.00*(r2^2.00*sin(x(1.00))^2.00-
1.00*r3^2.00))/r3^2.00)^(3.00/(2.00))*ms*r2^6.00*r3^4.00+4.00*x(2.00)^2
.00*sqrt(-(1.00*(r2^2.00*x(1.00)^2.00-
1.00*r3^2.00))/r3^2.00)*sin(x(1.00))*(-
(1.00*(r2^2.00*sin(x(1.00))^2.00-
1.00*r3^2.00))/r3^2.00)^(3.00/(2.00))*cos(x(1.00))^2.00*ms*r2^2.00*r3^8
.00+2.00*x(1.00)^4.00*x(2.00)^2.00*sqrt(-(1.00*(r2^2.00*x(1.00)^2.00-
1.00*r3^2.00))/r3^2.00)*sin(x(1.00))*cos(x(1.00))*ms*r2^5.00*r3^5.00+sq
rt(-(1.00*(r2^2.00*x(1.00)^2.00-1.00*r3^2.00))/r3^2.00)*sin(x(1.00))*(-
(1.00*(r2^2.00*sin(x(1.00))^2.00-
1.00*r3^2.00))/r3^2.00)^(3.00/(2.00))*cos(x(1.00))*g*mprbm*r2*r3^8.00-
4.00*x(1.00)^2.00*x(2.00)^2.00*sqrt(-(1.00*(r2^2.00*x(1.00)^2.00-
1.00*r3^2.00))/r3^2.00)*sin(x(1.00))^3.00*sqrt(-
(1.00*(r2^2.00*sin(x(1.00))^2.00-
1.00*r3^2.00))/r3^2.00)*cos(x(1.00))^2.00*ms*r2^6.00*r3^4.00+4.00*x(1.0
0)^4.00*x(2.00)^2.00*sqrt(-(1.00*(r2^2.00*x(1.00)^2.00-
1.00*r3^2.00))/r3^2.00)*sin(x(1.00))*(-
(1.00*(r2^2.00*sin(x(1.00))^2.00-
1.00*r3^2.00))/r3^2.00)^(3.00/(2.00))*cos(x(1.00))^2.00*ms*r2^6.00*r3^4
.00+2.00*x(1.00)^4.00*x(2.00)^2.00*sqrt(-(1.00*(r2^2.00*x(1.00)^2.00-
1.00*r3^2.00))/r3^2.00)*sin(x(1.00))^3.00*sqrt(-
(1.00*(r2^2.00*sin(x(1.00))^2.00-
1.00*r3^2.00))/r3^2.00)*cos(x(1.00))^2.00*ms*r2^8.00*r3^2.00-
8.00*x(1.00)^2.00*x(2.00)^2.00*sqrt(-(1.00*(r2^2.00*x(1.00)^2.00-
1.00*r3^2.00))/r3^2.00)*sin(x(1.00))*(-
(1.00*(r2^2.00*sin(x(1.00))^2.00-
1.00*r3^2.00))/r3^2.00)^(3.00/(2.00))*cos(x(1.00))^2.00*ms*r2^4.00*r3^6
.00+x(1.00)^4.00*sqrt(-(1.00*(r2^2.00*x(1.00)^2.00-
1.00*r3^2.00))/r3^2.00)*sin(x(1.00))*(-
(1.00*(r2^2.00*sin(x(1.00))^2.00-
1.00*r3^2.00))/r3^2.00)^(3.00/(2.00))*cos(x(1.00))*g*mprbm*r2^5.00*r3^4
.00+2.00*K*asin(r2*x(1.00)/r3)*sin(x(1.00))^4.00*r2^4.00*r3^4.00-
4.00*K*asin(r2*x(1.00)/r3)*sin(x(1.00))^2.00*r2^2.00*r3^6.00+2.00*K*x(1
.00)^4.00*asin(r2*x(1.00)/r3)*sin(x(1.00))^4.00*r2^8.00+2.00*K*x(1.00)^
4.00*asin(r2*x(1.00)/r3)*r2^4.00*r3^4.00-
4.00*K*x(1.00)^2.00*asin(r2*x(1.00)/r3)*r2^2.00*r3^6.00+2.00*sqrt(-
(1.00*(r2^2.00*x(1.00)^2.00-
1.00*r3^2.00))/r3^2.00)*sin(x(1.00))*g*ms*r3^9.00+2.00*sqrt(-
(1.00*(r2^2.00*x(1.00)^2.00-
1.00*r3^2.00))/r3^2.00)*sin(x(1.00))*g*mprbm*r3^9.00+8.00*K*x(1.00)^2.0
0*asin(r2*x(1.00)/r3)*sin(x(1.00))^2.00*r2^4.00*r3^4.00+2.00*J3*x(1.00)
*x(2.00)^2.00*sqrt(-(1.00*(r2^2.00*x(1.00)^2.00-
1.00*r3^2.00))/r3^2.00)*r2^3.00*r3^5.00))/(sqrt(-
(1.00*(r2^2.00*x(1.00)^2.00-1.00*r3^2.00))/r3^2.00)*r2*r3*(-
2.00*x(1.00)^4.00*(-(1.00*(r2^2.00*sin(x(1.00))^2.00-
1.00*r3^2.00))/r3^2.00)^(3.00/(2.00))*sin(x(1.00))^2.00*cos(x(1.00))*ms
*r2^5.00*r3^3.00-
1.00*x(1.00)^4.00*sin(x(1.00))^6.00*ms*r2^8.00+x(1.00)^4.00*sin(x(1.00)
)^4.00*cos(x(1.00))^2.00*ms*r2^8.00+2.00*x(1.00)^4.00*sin(x(1.00))^4.00
*ms*r2^6.00*r3^2.00-
1.00*x(1.00)^4.00*sin(x(1.00))^2.00*cos(x(1.00))^2.00*ms*r2^6.00*r3^2.0
0+4.00*x(1.00)^2.00*(-(1.00*(r2^2.00*sin(x(1.00))^2.00-
```

```
1.00*r3^2.00))/r3^2.00)^(3.00/(2.00))*sin(x(1.00))^2.00*cos(x(1.00))*ms
*r2^3.00*r3^5.00+2.00*x(1.00)^2.00*sin(x(1.00))^6.00*ms*r2^6.00*r3^2.00
-
2.00*x(1.00)^2.00*sin(x(1.00))^4.00*cos(x(1.00))^2.00*ms*r2^6.00*r3^2.0
0-1.00*x(1.00)^4.00*sin(x(1.00))^2.00*ms*r2^4.00*r3^4.00-
4.00*x(1.00)^2.00*sin(x(1.00))^4.00*ms*r2^4.00*r3^4.00+2.00*x(1.00)^2.0
0*sin(x(1.00))^2.00*cos(x(1.00))^2.00*ms*r2^4.00*r3^4.00-2.00*(-
(1.00*(r2^2.00*sin(x(1.00))^2.00-
1.00*r3^2.00))/r3^2.00)^(3.00/(2.00))*sin(x(1.00))^2.00*cos(x(1.00))*ms
*r2*r3^7.00-
1.00*sin(x(1.00))^6.00*ms*r2^4.00*r3^4.00+sin(x(1.00))^4.00*cos(x(1.00)
)^2.00*ms*r2^4.00*r3^4.00+J3*x(1.00)^2.00*sin(x(1.00))^4.00*r2^6.00+2.0
0*x(1.00)^2.00*sin(x(1.00))^2.00*ms*r2^2.00*r3^6.00+2.00*sin(x(1.00))^4
.00*ms*r2^2.00*r3^6.00-
1.00*sin(x(1.00))^2.00*cos(x(1.00))^2.00*ms*r2^2.00*r3^6.00-
2.00*J3*x(1.00)^2.00*sin(x(1.00))^2.00*r2^4.00*r3^2.00-
1.00*J3*sin(x(1.00))^4.00*r2^4.00*r3^2.00-
1.00*sin(x(1.00))^2.00*ms*r3^8.00+J3*x(1.00)^2.00*r2^2.00*r3^4.00+2.00*
J3*sin(x(1.00))^2.00*r2^2.00*r3^4.00-1.00*J3*r3^6.00));
        %tum=offset+u2*(r2*sin(x(1))*x(2)-
r2^2*sin(x(1))*cos(x(1))*x(2)/(r3*sqrt(1-r2^2*sin(x(1))^2/r3^2)));
      dxdt=[dxdt_1;dxdt_2];
    end
end
```

APPENDIX G

ANSYS® INPUT CODE

```
finish
/clear

/TITLE, Dynamic Analysis
/FILNAME,Dynamic,0 ! This sets the jobname to 'Dynamic'
/PREP7 ! Enter preprocessor
K,1,0,0 ! Keypoints
K,2,20,0
finish !These two commands clear current data
/clear
/title, Nonlinear Analysis
/prep7 ! Enter the preprocessor
et,1,BEAM3 ! Define element as Beam3
mp,ex,1,112364.35 ! Young's modulus (in MPa)
mp,prxy,1,0.33 ! Poisson's ratio
r,1,0.6874,0.004331,0.137482 ! area, I, height
k,1,0,0,0 ! Fixed-end
k,2,10,0,0 ! Guided-end
l,1,2 ! Line 1 k1-k2
esize,0.5 ! Sets element size to 0.5 in.
REAL,1
lmesh,1 ! Mesh line
finish
/solu
antype,static ! Static analysis (not buckling)
!!Comment above line and uncomment below for modal analysis!!!
!ANTYPE,2 ! Modal analysis
!MODOPT,SUBSP,5 ! Subspace, 5 modes
!EQSLV,FRONT ! Frontal solver
!MXPAND,5
!!!!!
nlgeom,on ! Nonlinear geometry solution supported
outres,all,all ! Stores bunches of output
nsubst,5 ! Load broken into 5 load steps
neqit,20 ! Use 20 load steps to find solution
autots,on ! Auto time stepping
lnsrch,on
/eshape,0 ! Plot the beam as a volume rather than line
dk,1,all,0 ! Constrain bottom
dk,2,uy,0.127082 !Deflect End
finish
/post1
/eshape,1
PLNS,u,sum $ /REPLOT
```

BIBLIOGRAPHY

[1] Norton, T. W., "On the Nomenclature, Classification, and Mobility of Compliant Mechanisms," MS Thesis, Purdue University, 1991.

[2] Midha, A., Her, I., and Salamon, B. A., "A Methodology for Compliant Mechanism Design: Part I – Introduction and Large-Deflection Analysis," *Advances in Design Automation*, 18th ASME Design Automation Conference, DE-Vol. 44, No. 2, 1992, pp. 29-38.

[3] Midha, A., and Visser, S. C., "Compliant Pliers," US Patent No. 5,522,290, issued June 4, 1996.

[4] N. A., "How to Make an Atlatl," Utah State History, Archaeology (Antiquities Section). N.d.

[5] Guttman, J., "English Longbow," *Military History*, Vol. 28, 2011, pp. 23.

[6] Michelin Tweel Technologies, Michelin, http://www.michelintweel.com/, 27 September 2015.

[7] Stratton, E., "Design and Analysis of a Compliant Mechanism Spinal Implant," MS Thesis, Brigham Young University, 2010.

[8] Leonhard Euler. Methodus inveniendi lineas curvas maximi minimive proprietate gaudentes, sive solutio problematis isoperimetrici lattissimo sensu accepti, chapter Additamentum 1. eulerarchive.org E065, 1744.

[9] Burns, R. H., and Crossley, F. R. E., "Kinetostatic Synthesis of Flexible Link Mechanisms," ASME Paper 68-Mech-36, 1968.

[10] Bisshopp, K. E., and Drucker, D. C., "Large-defection of Cantilever Beams," *Quarterly of Applied Mathematics*, Vol. 3, No. 3, 1945, pp. 272-275.

[11] Her, I., Midha, A., and Salamon, B. A., "A Methodology for Compliant Mechanisms Design: Part II – Shooting Method and Application," *Advances in Design Automation*, 18th ASME Design Automation Conference, DE-Vol. 44, No. 2, 1992, pp. 39-45.

[12] Salamon, B. A., "Mechanical Advantage Aspects in Compliant Mechanisms Design," MS Thesis, Purdue University, 1989.

[13] Salamon, B. A., and A. Midha, "An Introduction to Mechanical Advantage in Compliant Mechanisms," *Journal of Mechanical Design*, Trans. ASME, Vol. 120, No. 2, June 1998, pp. 311-315.

[14] Midha, A., Bapat, S., Midha, P., " Mechanical Advantage of a Compliant Mechanism and Significant Factors Affecting it, Using the Pseudo-Rigid-Body Model Approach," *Proceedings of the ASME 2015 International Design Engineering Technical Conferences & Computers and Information in Engineering Conference,* Boston, MA, August 2015, pp. DETC47930-1-3.

[15] Bapat, S. G., "On the Design and Analysis of Compliant Mechanisms Using the Pseudo-Rigid-Body Model Concept," PhD Dissertation, Missouri University of Science and Technology, 2015.

[16] Byers, F. K., and Midha, A., "Design of a Compliant Gripper Mechanism," *Proceedings of the 2nd National Applied Mechanisms and Robotics Conference*, Cincinnati, OH, 1991, pp. XC-1-1 – XC-1-12.

[17] Nahvi, H., "Static and Dynamic Analysis of Compliant Mechanisms Containing Highly Flexible Members," PhD Dissertation, Purdue University, 1991.

[18] Murphy, M., "A generalized Theory for the Type Synthesis and Design of Compliant Mechanisms," PhD Dissertation, Purdue University, December 1993.

[19] Howell, L. L., "A Generalized Loop-Closure Theory for the Analysis and Synthesis of Compliant Mechanisms," PhD Dissertation, Purdue University, December 1993.

[20] Howell, L. L., and Midha, A., "Parametric Deflection Approximations for End-Loaded, Large-Deflection Beams in Compliant Mechanisms," *Journal of Mechanical Design*, Trans. ASME, Vol. 117, No. 1, March 1995, pp. 156-165.

[21] Howell, L. L., and Midha, A., " A Method for the Design of Compliant Mechanisms with Small-Length Flexural Pivots," *Journal of Mechanical Design*, Trans. ASME, Vol. 116, No. 1, March 1994, pp. 280-290.

[22] Howell, L. L., "The Design and Analysis of Large-Deflection Members in Compliant Mechanisms," MS Thesis, Purdue University, 1991.

[23] Howell, L. L., and Midha, A., "Parametric Deflection Approximations for End-Loaded, Large-Deflection Beams in Compliant Mechanisms," *Journal of Mechanical Design*, Trans. ASME, Vol. 117, No. 1, March 1995, pp. 156-165.

[24] Midha, A., et al, "Analysis of a Fixed-Guided Compliant Beam With an Inflection Point Using the Pseudo-Rigid-Body Model Concept," Journal of Mechanisms and Robotics, Trans. ASME, Vol. 7, No.3, August 2015.

[25] Mettlach, G. A., and Midha. A., "Characteristic Deflection Domain Concept in Compliant Mechanism Design and Analysis," *Proceedings of the 6th National*

Applied Mechanisms and Robotics Conference, Cincinnati, Ohio, December, 1999, pp. 27-01 – 27-06.

[26] Midha, A., Bapat, S. G., "Characterisitic Deflection Domain for Various Compliant Segment Types, and its Importance in Compliant Mechanism Syntehsis and Analysis," *Proceedings of the ASME 2014 International Mechanical Engineering Congress and Exposition*, Montreal, Quebect, Canada, November 14-20, pp. IMECE2014-338795.

[27] Pauly, J., "Analysis of Compliant Mechanisms with Complex Shaped Segments," MS Thesis, University of Missouri-Rolla, 2002.

[28] Kuber, R., "Development of a Methodology For Pseudo-Rigid-Body Models of Compliant Segments with Inserts, and Experimental Validation," MS Thesis, Missouri University of Science & Technology, 2013.

[29] Wahl, A., *Mechanical Springs*, 2nd Ed., McGraw-Hill, New York, 1965.

[30] Oakes, M. E., Racely, K. L., "Constant Force Mechanism," US Patent: 2906524A, September 1959.

[31] Dykema, O. W. "Constant Spring Force Mechanism," US Patent: 4673170A, June 1987.

[32] Baker, A. L. "Drafting Machine," US Patent: 2996805A, August 1961.

[33] Harmening, N., "Static Mass Balancing with a Torsion Spring and Four Bar Linkage," *ASME Design Engineering Technical Conference*, paper 74-DET-29, New York, NY, USA, 1974.

[34] Carson, W., and Stephens, J., "Feasible Parameter design spaces for force and root-mean square moment balancing on in-line 4R 4bar linkage synthesized for kinematic criteria," *Journal of Mechanisms and Machines Theory*, 1978, pp. 649-658.

[35] Jenuwine, J. G., and Midha, A., "Synthesis of Single-Input and Multiple-Output Port Mechanisms with Springs for Specified Energy Absorption," *Journal of Mechanical Design*, Trans. ASME, Vol. 116, September 1994, pp. 937-943.

[36] Howell, L. L., Midha, A., and Murphy, M. D., "Dimensional Synthesis of Compliant Constant-force Slider Mechanisms," *Machine Elements and Machine Dynamics*, Trans. ASME, DE-Vol. 71, 1994, pp. 509-515.

[37] Midha, A., Murphy, M., and Howell, L. L., "Compliant Constant-Force Mechanism and Devices Formed Therewith," US Patent: 5649454, Jul, 22, 1997.

[38] Miller, A. J., Howell, L. L., and Leonard, J. N., "Design and Evaluation of Compliant Constant-force Mechanisms," *The 1996 ASME Design Engineering Technical Conferences and Computers in Engineering Conference*, August 18-22, 1996, DETC/MECH-1209.

[39] Parkinson, M. B., Howell, L. L, and Cox, J. J., "A Parametric Approach to the Optimization-based design of compliant mechanisms," *Proceedings of the ASME Design Engineering Technical Conferences*, DETC-1997-DAC-3763.

[40] Evans, M.S. and Howell, L.L., 1999, "Constant-Force End-Effector Mechanism," *Proceedings of the IASTED International Conference, Robotics and Applications*, Oct. 28-30, Santa Barbara, CA, USA, pp. 250-256.

[41] Weight, B. L., "Development and Design of Constant-Force Mechanisms," MS Thesis, BYU, 2001.

[42] Nahar, D. R., Sagar, T., "Compliant Constant-Force Mechanism with a Variable Output for Micro/Macro Application," *IEEE 2003 International Conference on Robotics and Automation,* September 14-19, 2003.

[43] Howell, L. L and Magleby. S. P., "Substantially Constant-force Exercise Machine," US Patent: 0198571 A1, 2004.

[44] Meaders, J. C., and Mattson, C. A., "Optimization of near-constant-force springs subject to mating uncertainty," *Research Paper*, DOI 10.1007/s00158-009-0410-4.

[45] Hajhashemi, M. S., Barazandeh, F., Nejad.S. N., and Nadafi. R., "Design and microfabrication of a constant-force microgripper," *Proceedings of the Institution of Mechanical Engineers*, Vol. 0, Part C, July 25, 2011, pp. 1177-1 - 1177-10.

[46] Lan, C. C., Wang, J. H., and Chen, Y. H., "A Compliant Constant-Force Mechanism for Adaptive Robot End-Effector Operations," *IEEE International Conference on Robotics and Automation,* May 2010, pp. 2131-2136.

[47] Ugwuoke, I.C., "Development and Design of Constant-Force Compression Spring Electrical Contacts," *Regular Paper*, AU J.T. 14(4), April 2011, pp. 243-252.

[48] Boyle, C., "A Closed-Form Dynamic Model of the Compliant Constant-Force Mechanism Using the Pseudo-Rigid-Body Model," MS Thesis, Brigham Young University, 2003.

[49] Lyons, S. M., "The Pseudo-Rigid-Body Model for Dynamic Predictions of Macro and Micro Compliant Mechanisms," PhD Dissertation, Brigham Young University, 2003.

[50] Yu, Y., Howell, L. L., and Lusk, C., "Dynamic Modeling of Compliant Mechanisms Based on the Pseudo-Rigid-Body Model," *Journal of Mechanical Design*, Trans. ASME, Vol. 127, 2005, pp. 760-765.

[51] Wang, W., and Yu, Y., "New Approach to the Dynamic Modeling of Compliant Mechanisms," *Journal of Mechanisms and Robotics*, Trans. ASME, Vol. 2, 2010, pp. 021003-1-8.

[52] Hongzhe, Z., Shusheng, B., and Bo, P., "Dynamic analysis and experiment of a novel ultra-precision compliant linear-motion mechanism," *Journal of Precision Engineering*, Vol 42, 2015, pp. 352-359.

[53] Benamar, R., Bennouna, M. M., White, R. G., "The Effects of large Vibration Amplitudes on the Mode Shapes and Natural Frequencies of Thin Elastic Structures Part I: Simply Supported and Clamped-Clamped Beams," *Journal of Sound and Vibration*, 1991, Vol. 142(2), pp.179-195.

[54] Gorski, W., "A Review on Literature and a Bibliography on Finite Elastic Deflection of Bars," *Transaction of the Institution of Engineers, Australia, Civil Engineering*, Vol. 18, No. 2, 1976, pp. 74-85.

[55] Midha, A., Kuber, R., Chinta, V., Bapat, G., "A Method for a More Accurate Calculation of the Stiffness Coefficient in a Pseudo-Rigid-Body Model (PRBM) of a Fixed-Free Beam Subjected to End Forces," *Proceedings of the ASME 2014 International Design Engineering Technical Conferences & Computers and Information in Engineering Conference*, Buffalo, NY, August, 2014, pp. DETC35366-1-10.

[56] Karthik, K. "On the Design of A Nearly Constant-Force Modular Device Based on A Compliant Slider Mechanism," MS Thesis, Missouri University of Science and Technology, 2015.

[57] Midha, A., Ed. Chapter 9, "Elastic Mechanisms," *Modern Kinematics: Developments in the Last Forty Years*, (Ed.: A G. Erdman), John Wiley & Sons, Inc., New York, New York, 1993, pp. 369-449.

[58] Midha, A., Prasanna, B. P., "Mode shapes in Compliant Mechanisms and A procedure To Identify Appropriate Pseudo-Rigid-Body Model Type," *Proceedings of the ASME 2015 International Design Engineering Technical Conferences & Computers and Information in Engineering Conference*, Boston, MA, August 2015, pp. DETC47694-1-9.

[59] Zadoks, R. I., “Parametric Stability Analysis of A Two Degree-of-Freedom Machine System,” PhD Dissertation, Purdue University, 1985.

[60] Rao, S. S., *Vibrations of Continuous Systems,* John Wiley & Sons, Inc. New York, New York, 2007.

[61] Azrar, L., Benamar, R., White, R. G., “A Semi-Analytical Approach to the Non-Linear Dynamic Response Problem of Beams At Large Vibration Amplitudes, Part II: Multimode Approach to the Steady State Forced Periodic Response,” *Journal of Sound and Vibration,* Vol. 255(1), 2002, pp. 1-41.

[62] Abed, E. H., Hassouneh, M. A., Hashlamoun, W. A., “Modal Participation Factors Revisited: One Definition Replaced by Two,” *American Control Conference,* St. Louis, MO, June 2009, pp. 978-1-4244-4525-1140-1145.

[63] Graesser, E. J., Wong C. R., “Analysis of Strain Dependent Damping in Materials via Modeling of Material Point Hysteresis,” Ship Materials Engineering Department Research and Development Report, David Taylor Research Center, Bethesda, MD, July 1991.

[64] Albers, J. M., A. Midha, J. M. Starkey and T. D. White, “Design of an Accelerated Pavement Testing Machine Based on a Constant-Force Mechanism,” Proceedings of the 6th National Applied Mechanisms & Robotics Conference, Cincinnati, Ohio, December 1999, pp. 49-01 – 49-13.

[65] Friction and Coefficients of Friction, Engineering ToolBox, http://www.engineeringtoolbox.com/friction-coefficients-d_778.html, 27 September 2015.

[66] Midha, A., Miyamoto, A., Williams, D., “Equipment to Measure Shock Loads,” ME 261: Senior Design Missouri S&T, University of Missouri University of Science and Technology, Rolla, MO, November 2010.

[67] NI 9234, National Instruments Incorporated, http://sine.ni.com/nips/cds/view/p/lang/en/nid/208802, 27 September 2015.

VITA

Andrew Christian was born in August 1990, in Maryville, Missouri. He received his Bachelor's degree in Mechanical Engineering from Missouri University of Science and Technology in December 2013. During his undergraduate career he interned at Caterpillar Inc. as a structures and dynamics intern. He also interned at ABB Inc., and Murray Energy Corp., as a corporate intern. In January of 2014 he was accepted into the MS program in Mechanical Engineering at the Missouri University of Science and Technology in Rolla, Missouri. In December 2015 he received his MS in Mechanical Engineering.